LEVEL

② ①²

⑥

TARGET IDENTIFICATION USING RADAR IMAGERY AND MOMENT METHODS.

⑩ GEORGE A. IOANNIDIS

ADVANCED PROGRAMS DIVISION
RADAR SYSTEMS GROUP

HUGHES AIRCRAFT COMPANY

EL SEGUNDO, CALIFORNIA 90245

⑪ JUNE 1980

⑫ 157

⑨ Final Report for Contract N00014-79-C-0643

Sep 79 - Jun 80,

⑭ HAC-FR80-23-919R,

HAC-REF-E5599

Submitted to
OFFICE OF NAVAL RESEARCH
Arlington, Virginia

RADAR SYSTEMS GROUP

HUGHES

HUGHES AIRCRAFT COMPANY
EL SEGUNDO, CALIFORNIA

375 119

80 8 25 145

SECURITY CLASSIFICATION OF THIS PAGE *(When Data Entered)*

REPORT DOCUMENTATION PAGE		READ INSTRUCTIONS BEFORE COMPLETING FORM
1. REPORT NUMBER	2. GOVT ACCESSION NO. AD-A088 514	3. RECIPIENT'S CATALOG NUMBER
4. TITLE *(and Subtitle)* Target Identification Using Radar Imagery and Moment Methods		5. TYPE OF REPORT & PERIOD COVERED Final Report Sept. 1979 - June 1980
		6. PERFORMING ORG. REPORT NUMBER FR80-23-919R
7. AUTHOR(s) George A. Ioannidis		8. CONTRACT OR GRANT NUMBER(s) N00014-79-C-0643
9. PERFORMING ORGANIZATION NAME AND ADDRESS Hughes Aircraft Company Advanced Programs Division, Radar Systems Group 2000 East Imperial Hwy., El Segundo, CA 90245		10. PROGRAM ELEMENT, PROJECT, TASK AREA & WORK UNIT NUMBERS
11. CONTROLLING OFFICE NAME AND ADDRESS Office of Naval Research Department of the Navy 800 N. Quincy Street Arlington, VA 22217		12. REPORT DATE June 1980
		13. NUMBER OF PAGES 156
14. MONITORING AGENCY NAME & ADDRESS*(if different from Controlling Office)* Office of Naval Research Arlington, VA		15. SECURITY CLASS. *(of this report)* Unclassified
		15a. DECLASSIFICATION/DOWNGRADING SCHEDULE

16. DISTRIBUTION STATEMENT *(of this Report)*

Approved for public release: distribution UNLIMITED

17. DISTRIBUTION STATEMENT *(of the abstract entered in Block 20, if different from Report)*

Unlimited

18. SUPPLEMENTARY NOTES

19. KEY WORDS *(Continue on reverse side if necessary and identify by block number)*

ISAR, NCTR, Target Classification, Radar Image Recognition

20. ABSTRACT *(Continue on reverse side if necessary and identify by block number)*

In this investigation the Hughes Aircraft Company studied the application of the geometric moments of an image and rotationally invariant functions of these moments to the automatic recognition of radar images of aircraft targets generated using the ISAR technique.

DD FORM 1 JAN 73 3 EDITION OF 1 NOV 65 IS OBSOLETE

FINAL REPORT FOR TARGET IDENTIFICATION
USING RADAR IMAGERY AND MOMENT METHODS

Meets Data Requirement A002 of
Contract N00014-79-C-0643

By George A. Ioannidis

June 1980

FOREWORD

This report describes an investigation conducted by the Hughes Aircraft Company, Radar Systems Group, El Segundo, California, to test the use of the geometric moments of an image and of the rotationally invariant functions of these moments for the automatic recognition of aircraft targets from radar images. The effort consisted of radar image generation from real data and analysis and computer studies of statistical pattern recognition techniques for the automatic recognition of targets using the geometric moments of radar images.

The investigation was performed by the Signal Exploitation Programs Office of Hughes' Radar Systems Group, for the Office of Naval Research, Arlington, Virginia, under Contract N00014-79-C-0643.

Dr. George A. Ioannidis served as the Hughes program manager. Commander Stacy Holmes followed by Commander Roger Nichols were the program managers for the Office of Naval Research, Arlington, Virginia.

The analytical tasks for this study were carried out by the program manager with help from Jon P. Belleville, who also contributed to the development of the software and wrote Appendix A.

The major contributor to the development of the software for this study was Charles P. Dolan who also wrote Appendix B.

This final report is submitted in accordance with the data requirements of Exhibit A, dated 20 August 1979, Sequence A002 of the contract Data Requirements List 1423.

The author acknowledges the support and contributions of Messrs. James Crosby, Manager, and Calvin Boerman, Assistant Manager of Signal Exploitation Programs at Hughes. The author also thanks Dr. Chung-Ching Chen who provided the images of the F-111.

1

CONTENTS

CONTENTS (Continued)

LIST OF ILLUSTRATIONS

LIST OF ILLUSTRATIONS (Continued)

LIST OF TABLES

LIST OF TABLES (Concluded)

SECTION I
INTRODUCTION AND SUMMARY

In the past, most radar target recognition techniques have concentrated on the use of one-dimensional target signatures. However, the development of the Synthetic Aperture Radar (SAR) and the recent development of the Inverse Synthetic Aperture (ISAR) technologies have made it possible to obtain radar images of targets and thus allow the use of two-dimensional pattern classification schemes for automatic radar target recognition. One such two-dimensional shape recognition scheme is a technique known as the method of moments, which has been successfully applied to the recognition of objects imaged in the visible and infrared spectrum. Recently under an Office of Naval Research (ONR) sponsored investigation Gonzalez and Moret [8] applied the method of moments to the classification of simulated radar images. Their results showed that very good classification performance could be obtained using this technique.

In this investigation sponsored by ONR the Hughes Aircraft Company studied the application of the geometric moments of an image and rotationally invariant functions of these moments to the automatic recognition of aircraft targets from their radar images. The images used in this investigation were generated by the application of the ISAR technique to turntable radar data and also data obtained from flying aircraft targets. The turntable data had been obtained at the RATSCAT facility under the AFAL E-3A Non-Cooperative Data Collection program and consist of X-band measurements against 1/3 scale models of an F-102, an F-5E, an A-10, an F-15 and a YF-16. The data were collected using the stepped frequency technique using a total of 256 3.4 MHz frequency steps to synthesize an 870.4 MHz bandwidth. For the full scale targets these measurements correspond to S-band data at 290 MHz bandwidth. The targets were placed on a rotary platform which rotated at 0.2 degree increments between adjacent bursts of the 256 frequency steps. In addition to the RATSCAT data, measurements for a maneuvering F-111 aircraft and a DC-10 during take off were also used. The data on the F-111 were obtained using the ALCOR radar which uses a linear F-M pulse with 500 MHz bandwidth. The data on the DC-10 were obtained by an S-band

1

radar operated by the Naval Ocean Systems Center (NOSC) in San Diego. By
stepping the transmitter frequency pulse to pulse at 1.08 MHz increments over
a total of 256 pulses this radar has an effective bandwidth of 276 MHz. The
images of the F-111 were available from the work of Chen and Andrews [14].
Images for all these aircraft targets were generated using the techniques
described in Section 2.

Using the above data a set of 540 images was formed from the
RATSCAT data base (108 images per target for an F-102, an F-15, an
YF-16, an F-5E, and an A-10). The first 72 images for each target were
obtained using the lower 128 frequencies covering a bandwidth of 128 MHz
out of a total of 256 MHz measurement bandwidth. The last 36 images out
of the total of 108 images per target were obtained using the upper 128 fre-
quencies. The resulting range resolution was 1.17 meters. The images
were formed for a 3-degree rotation of the target which results in a cross
range resolution of 0.95 meters. The images were formed over the following
set of aspect angles 0-3 degrees, 5-8 degrees, . . . , 175-178 degrees and
2-5 degrees, 7-10 degrees, 12-15 degrees, . . . , 177-180 degrees for the
first set of 128 frequencies and for aspects 0-3 degrees, 5-8 degrees, . . . ,
175-178 degrees for the second set of 128 frequencies.

The images of the F-111 obtained using the ALCOR radar ranged
over the following aspect angles: 0-3 degrees, 5-8 degrees, . . . ,
85-87 degrees and 2-5 degrees, 7-10 degrees, . . . , 87-90 degrees. All of
the above images corresponded to top views of the targets, i.e., projections
on the horizontal plane. From the NOSC data set a small number of images,
10 top views, and 10 side views were obtained for a DC-10. However,
because the target in this case was moving it was necessary to use the full
256 MHz measurement bandwidth to properly focus and align the range signa-
tures used in forming the image. For classification tests only the ten side
views obtained on this target were used. These images were combined with
a set of ten side view images obtained using RATSCAT measurements for the
F-5E and A-10. In addition to the above classification tests the classifiers
were also presented with top view images of the RATSCAT targets obtained
using the full 256 MHz bandwidth and a 6.2 degree rotation of the target.
For these tests 24 images per target for the five RATSCAT targets were

formed over the following set of aspects: 0.8-7 degrees, 3.8-10 degrees, 6.8-13 degrees, ..., 33.8-40 degrees and 140.8-147 degrees, 143.8-150 degrees, ..., 173.8-180 degrees. The images used in this study are given in Table 1.

In addition to the generation of the above images, software was developed for image processing such as background noise computation, adaptive threshold adjustment, edge enhancement and edge detection. Software was also developed for the computation of all central moments of orders two to seven and of all orthogonal moment invariant functions using moments of orders two to seven. As described in Section III, the total number of required moments is 33 and is also equal to the total number of invariants. Also three general algebraic invariants were computed as described in Section III.

TABLE 1. RADAR IMAGES OF AIRCRAFT TARGETS
GENERATED FOR THIS STUDY

Data	View	Aspects	Frequency Steps
RATSCAT	Plan	$0-3^o$, $5-8^o$, ..., $175-178^o$	0 to 128
RATSCAT	Plan	$2-5^o$, $7-10^o$, ..., $177-180^o$	0 to 128
RATSCAT	Plan	$0-3^o$, $5-8^o$, ..., $175-178^o$	128 to 256
RATSCAT	Plan	$0.8-7^o$, $3.8-10^o$, $6.8-13^o$, ..., $33.8-40^o$	0 to 256
RATSCAT	Plan	$140.8-147^o$, $143.8-150^o$, ..., $173.8-180^o$	0 to 256
A-10, F-5E	Profiles	-18.2^o to 12°, -15.2^o to -9°, ..., 12° to 18.2^o	0 to 256
ALCOR (F-111)	Plan	$0-3^o$, $2-5^o$, $5-8^o$, ..., $87-90^o$	1.2 m resolution
NCSC (DC-10)	Profiles	10 nose aspects	0 to 256
NCSC (DC-10)	Plan	10 broadside aspects	0 to 256

(RATSCAT Targets: F-102, F-5E, F-15, YF-16, A-10.)

Moments and invariants were computed from both the image and the edge detected image (contour image) and classification tests were performed using feature vectors constructed from the moments and feature vectors constructed from the invariants. In addition to feature vectors computed from the geometric moments and invariants features obtained by collapsing the image intensities along two orthogonal axes (parallel and normal to the fuselage orientation) as described in Section IV were tested.

As seen in the results from the classification tests presented in Sections VI and VII the best performance (84 to 97 percent correct) was observed for feature vectors using the central moments of the image and also for combinations of moments from the image and the edge detected image. The results are encouraging and suggest that the geometric moments may prove to be important features for the application of statistical pattern recognition techniques to the identification of aircraft targets from radar images. However, because a limited set of imaging geometries (only plan views corresponding to projections on the horizontal plane for zero roll and profiles corresponding to projections on the vertical plane) was used in this study the performance of the techniques as a function of roll and pitch angles was not investigated. Further more it was assumed that the imaging plane was known. The determination of the target view presented by the image is an important problem that will be addressed in follow-on work in this area.

In addition to the above classification results obtained during this study a technique was also developed which uses invariant moment functions for the computation of the cross range scale in ISAR images of targets whose rotation rate is not known a priori.

Section II contains a discussion of the ISAR imaging and image processing algorithms used in this study. Section III is a discussion of the geometric moments and invariant functions of these moments and their use in the computation of the target aspect and the computation of the cross range scale factor of ISAR images. A recognition scheme based on image collapsing along two orthogonal axes is discussed in Section IV and Section V contains a description of the classifiers used in this investigation as well as two techniques used for reducing the dimensionality of the feature vectors. The classification results are contained in Section VI and the conclusions are given in Section VII. Details

4

on the computation of the invariant functions and a brief discussion of the software used in this study are found in Appendices A and B, respectively.

Section II
INVERSE SAR IMAGING BY FREQUENCY STEPPING

The most common radar imaging technique today is the SAR method
used primarily for ground mapping by airborne radars. The method
employs high range resolution waveforms and takes advantage of the linear
translational motion of the airborne antenna to generate a synthetic long
array with an effective azimuth beamwidth several times smaller than the
beamwidth of the radar antenna. Thus radar images of the ground and of
ground targets are generated.

When the radar target is moving (thus causing a change in target
aspect) a similar technique called ISAR can be used to image targets in
motion. The method takes advantage of the relative doppler shift of the sig-
nals returned from the various scatters on the target (as a result of the tar-
get's rotational motion) to obtain the scatterers cross range locations. Either
a single wideband pulse waveform or a burst of N narrow band pulses stepped
in frequency pulse to pulse over a large bandwidth can be used to obtain the
range profile of the target. For the stepped frequency waveform, a synthetic
high resolution range profile is obtained by Fourier transforming the target
echoes per frequency burst. The time history of the range profiles for a tar-
get with a changing aspect contains doppler frequencies that are directly
related to the target scatterers cross range locations. Thus the cross range
dimension at each range cell of a rotating target is obtained by Fourier trans-
forming the echo history of the range cell. In this way, range and cross
range data are mapped into a target image.

2.1 RANGE-DOPPLER IMAGING OF TARGETS ON A ROTARY PLATFORM

Radar imaging of targets on a rotary platform with a stepped
frequency radar system is briefly described here. The processing algo-
rithms for the formation of a radar image of the target are derived by repre-
senting the target by a collection of many point scatterers as described by

Chen and Andrews (1), Walker (2) and Wehner (3). Even though the analysis presented here follows this point scatterer model, the resulting imaging algorithms are also valid for targets that consist of one large continuous surface with dimensions much larger than the radar wavelength, as it follows from the work of R. M. Lewis (4) who by the use of physical optics formulas, found the same imaging algorithms as those obtained by the point scatterer model.

For the geometry of Figure 1, assume that the target consists of a large number of point scatterers. After coherent demodulation the received radar echo as a function of transmitter frequency f (wave number $k = 2\pi f/c$) and target aspect angle θ is given by

$$U(f,\theta) = \frac{E_o A_e}{2\sqrt{\pi} \lambda R_o^2} e^{j2\vec{k} \cdot \vec{R}_o} \int_{S_1} \rho(\vec{r};\theta) e^{j2\vec{k} \cdot \vec{r}} ds(\vec{r}) \tag{1}$$

where $\rho(\vec{r};\theta)$ is the complex target reflectivity at point $\vec{r}$ on the target surface when the aspect angle is θ, $\vec{k}$ is a vector pointing from the radar towards the center of the target and its magnitude is equal to the radar wave number given by

$$\|\vec{k}\| = \frac{2\pi}{\lambda} = \frac{2\pi f}{c} , \tag{2}$$

E_o is the amplitude of the transmitted pulse, A_e is the effective antenna aperture of the radar, R_o is the target range, and the surface integral is over the illuminated target surface S_1. Expressing the vectors $\vec{k}$ and $\vec{r}$ of Equation (1) in terms of the body coordinates X, Y (see Figure 1)

$$2\vec{k} \cdot \vec{r} = xp_x + yp_y \tag{3}$$

where:

$$p_x = (4\pi f/c) \cos\theta, \quad p_y = (4\pi f/c) \sin\theta$$

$$x = r\cos\alpha \text{ and } y = r\sin\alpha$$

Substituting from Equation (3) into (1),

$$U(p_x, p_y) = \left(\frac{E_o A_e}{2\sqrt{\pi}\,\lambda R_o^2}\right) e^{\,\overrightarrow{jp}\cdot\overrightarrow{R}_o} \int_{S_1}\int \rho(x,y;\theta)\, e^{\,j(xp_x + yp_y)} \, dxdy \tag{4}$$

which shows that the measured signal is a sample of the two dimensional Fourier transform of the target's reflectivity projected onto the horizontal plane and modulated by the linear phase term

$$e^{\,\overrightarrow{jp}\cdot\overrightarrow{R}_o}.$$

When in the measurement setup of Figure 1 pulse-to-pulse frequency stepping is used over a bandwidth $(f_{max} - f_{min})$, the resulting measurements correspond to samples of $U(p_x, p_y)$ over a region D in (p_x, p_y) space which is a section of a ring between two circles with radii p_1 and p_2 as shown in Figure 2. The corresponding measurement transfer function is

$$H(p_x, p_y) = 1 \ , \quad p_x = p\cos\theta \ , \quad p_y = p\sin\theta \tag{5a}$$

$$p_1 \le p \le p_2 \ , \quad -\frac{\Delta\theta}{2} \le \theta \le \frac{\Delta\theta}{2} \ , \quad H(p_x, p_y) = 0 \ , \quad \text{otherwise.} \tag{5b}$$

When $\Delta\theta$ is small and $(p_2 - p_1) \ll 1/2\,(p_2 - p_1)$, the Fourier transform of this measurement transfer function is given by

$$h(x, y) = \left(\frac{p_2^2 - p_1^2}{4\pi^2}\right) (\Delta\theta) \cdot \frac{\sin(\bar{p}y\,\Delta\theta/2)}{(\bar{p}y\,\Delta\theta/2)} \cdot \frac{\sin(x\Delta p/2)}{(x\Delta p/2)} \tag{6}$$
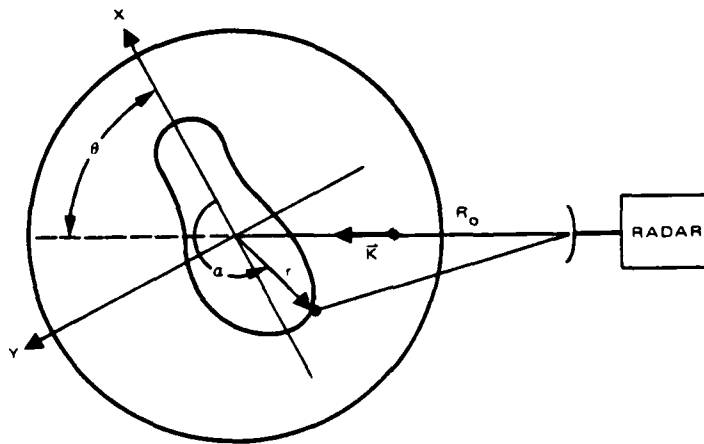
Figure 1. Imaging of target on a turntable.
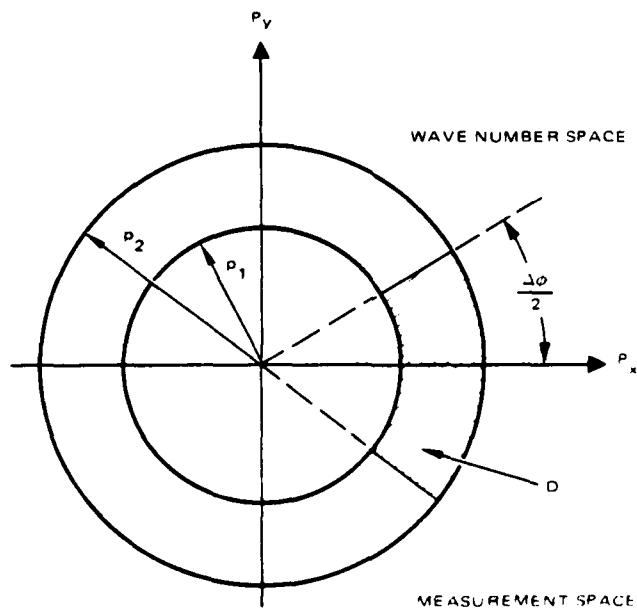
Figure 2. Mapping of measurement region in wave number space, for measurement set up of Figure 1

10

where X is the range axis and Y is the cross range axis, $\bar{p} = \dfrac{p_2 + p_1}{2}$ and $\Delta p = p_2 - p_1$. Therefore, the reconstructed reflectivity $\hat{\rho}(x, y)$ and the actual reflectivity profile $\rho(x, y)$ are related by the convolution integral

$$\hat{\rho}(x, y) = \iint dx' \, dy' \, h(x - x', y - y') \, \rho(x', y') \quad . \tag{7}$$

From Equations (6) and (7), the resulting range resolution is

$$\Delta x = \frac{2\pi}{\Delta p} = \frac{2\pi}{\dfrac{4\pi}{c}(f_{max} - f_{min})} = \frac{c}{2(f_{max} - f_{min})} \tag{8}$$

while the cross range resolution is given by

$$\Delta y = \frac{2\pi}{\bar{p}\Delta\theta} = \frac{\lambda}{2\Delta\theta} \tag{9}$$

where λ is the mean radar wavelength given by

$$\lambda = \frac{2c}{f_{max} + f_{min}}$$

From Equations (4) and (5a, b), the reconstructed reflectivity profile, which is the radar target image, is given by

$$\hat{\rho}(x, y) = K_o \int_{-\frac{\Delta\theta}{2}}^{\frac{\Delta\theta}{2}} d\theta \int_{p_1}^{p_2} p\,dp \; U(p, \theta) \, e^{jxp\cos\theta} \, e^{jyp\sin\theta} \quad , \tag{10}$$

where K_o is a constant that depends on range, effective antenna aperture, wavelength, and transmitter power. For small values of $\Delta\theta$, the above integral can be approximated by

$$\hat{\rho}(x, y) = K_o \int_{-\frac{\Delta\theta}{2}}^{\frac{\Delta\theta}{2}} d\theta \int_{p_1}^{p_2} p\,dp \; U(p, \theta) \, e^{jpx} \, e^{jp\theta y} \quad . \tag{11}$$

11

For numerical computations,

$$p = p_1 + k\Delta p \quad , \quad p_2 = p_1 + (N-1)\,\Delta p$$

$$\theta = i\delta\theta - \frac{\Delta\theta}{2} \quad , \quad \Delta\theta = (M-1)\delta\theta$$

$$x = n\Delta x \quad\quad , \quad\quad y = m\Delta y$$

and choose Δx, Δy so that

$$\Delta p\,\Delta x = \frac{2\pi}{N} \quad , \quad p_1\,\delta\theta\Delta y = \frac{2\pi}{M} \quad .$$

Using the above,

$$e^{jpx} = e^{jp_1 n\Delta x}\, e^{j(2\pi/N)kn}$$

$$e^{jp\theta y} = e^{j(2\pi/M)im}\, e^{j(2\pi/M)(\Delta p/p_1)imk}\, e^{-jp_1 y\Delta\theta/2}$$

$$= e^{j(2\pi/M)im}\left[1 + j\frac{2\pi}{M}\left(\frac{\Delta p}{p_1}\right)imk\right]e^{-jp_1 y\Delta\theta/2}$$

Substituting from above in Equation (11) and replacing the integrals by summations, the magnitude of $\hat{\rho}(x,\ y)$ is given by

$$\hat{\rho}(n\Delta x, m\Delta y) = K_o\frac{p_2^2 - p_1^2}{2}\left|\sum_{k=0}^{N-1}\sum_{i=0}^{M-1} U(k,i)\, e^{j(2\pi/N)kn}\, e^{j(2\pi/M)im}\right.$$

$$\left. - j\frac{2\pi}{M}\left(\frac{\Delta p}{p_1}\right)m \sum_{k=0}^{N-1}\sum_{i=0}^{M-1} k\cdot i\, U(k,i)\, e^{j(2\pi/N)kn}\, e^{j(2\pi/M)im}\right| \qquad (12)$$

In most radar image applications, only the first summation is used. The second summation which is multiplied by the very small factor

$$\frac{2\pi m}{M}\left(\frac{\Delta p}{p_1}\right)$$

where m is the cross range dimension index $(y = m\,\Delta y)$ is a small correction term that accounts for the error introduced by the approximations used in the polar to rectangular conversion and is usually neglected. The above polar-to-rectangular conversion also imposes a restriction on the maximum size of the angular sector $\Delta\theta$ in the measurement space that can be processed coherently to form a radar image. For large values of $\Delta\theta$, the polar-to-rectangular conversion introduces an error caused by scatterer motion through resolution cells. This problem imposes the following resolution limitations [5] when Equation (12) is used

$$\Delta CR > \left(\frac{\lambda L}{4}\right)^{1/2} \tag{13}$$

$$\Delta CR \cdot \Delta R > \left(\frac{\lambda D}{4}\right), \tag{14}$$

where:

ΔCR = cross range resolution

ΔR = range resolution

L = target length in range

D = target width in cross range, and

λ = radar wavelength.

This limitation can be avoided by polar format processing using Equation (10) at the expense of a computationally inefficient algorithm.

The stepped frequency technique was used to form images of five aircraft models. The data used for these images were collected at RATSCAT at X-band against 1 3 scale models of an F-102, an F-5E, a TF-1., an F-15 and an A-10. A total of 256 5.4 MHz frequency steps

13

were used. The targets were placed on a rotary platform that rotated at 0.2 degree increments. To avoid range aliasing the frequency step size must be less than (c/4L) where L is the target length. To avoid cross range aliasing the angular increment must be less than (λ/4D), where λ is the radar wavelength and D is the cross range target dimension. In the RAT-SCAT measurements the frequency step was adequate to avoid range aliasing, but the 0.2 degree angular increment was somewhat high for aspect angles near the broadside of the target. By introducing a human observer in many of the cases where cross range aliasing occurred for aspect angles other than head-on-broadside, the images were corrected when the aliased part could be resolved in the range dimension. The five scaled aircraft models were mounted both horizontally and vertically on the rotary platform so that both yaw and pitch angle rotation could be simulated. The measurements obtained when the targets were horizontally mounted on the platform gave plan (top) view images of the targets; examples are shown in Figures 3 through 8. The vertical mounting resulted in profile (side) view images as shown in Figures 9 and 10. For most of the classification tests described below, the top view images of the targets were used. One test, however, was performed with profiles of the F-5E, the A-10 and of a DC-10 during take off; stepped frequency measurements provided by the Naval Ocean Systems Center (NOSC) in San Diego were used. The technique used to image that target is described below.

2.2 RANGE-DOPPLER IMAGING OF MOVING TARGETS

When the target is moving, in addition to the change in target aspect, the range between the radar and the target is also changing. As a result of such range changes during formation of the radar image the images appear to be out of focus. The signal processing technique used to correct for this defocusing effect is known as autofocusing if it relies only on the received radar signal to accomplish this task. Although the autofocusing problem for the stepped frequency waveforms, in principle, is similar to the autofocusing problem for the single wideband pulse waveform, in the stepped frequency case a correction must also be introduced to account for phase errors

14
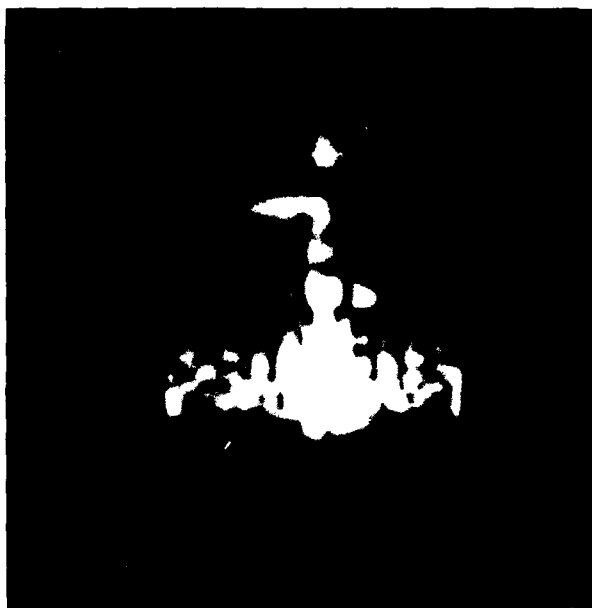
Figure 3. Top views of F-102 for tail aspect.
0.6m range resolution
0.45m cross range resolution

15
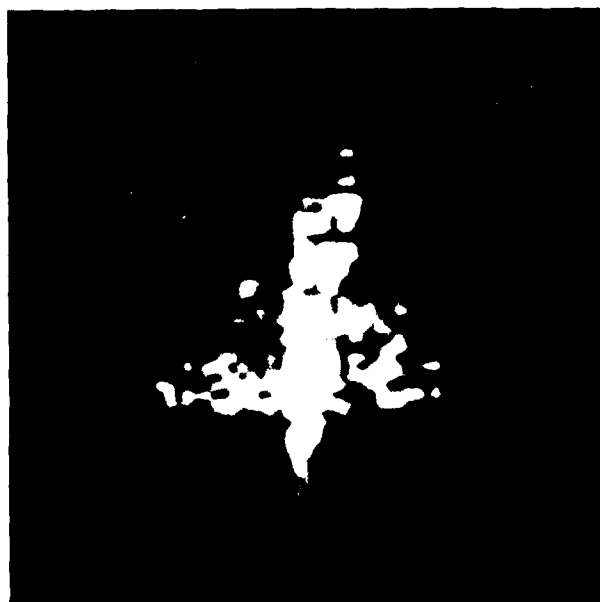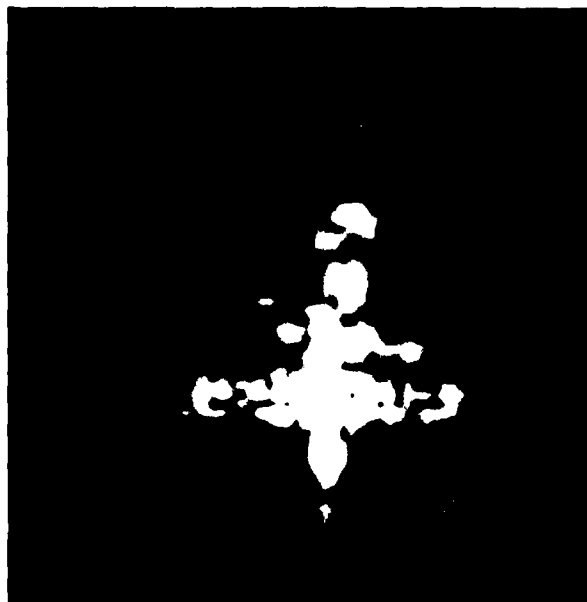
Figure 1. Plan views of F-5E for two aspects
(l) for range resolution
(r) for cross-range resolution

F-15
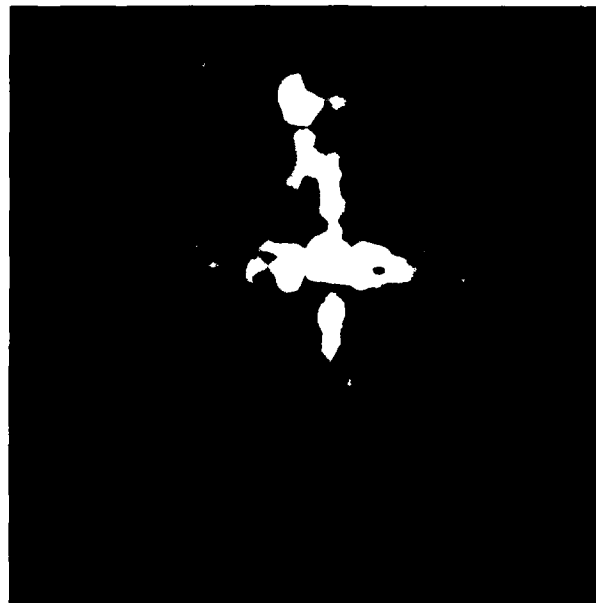
F-15
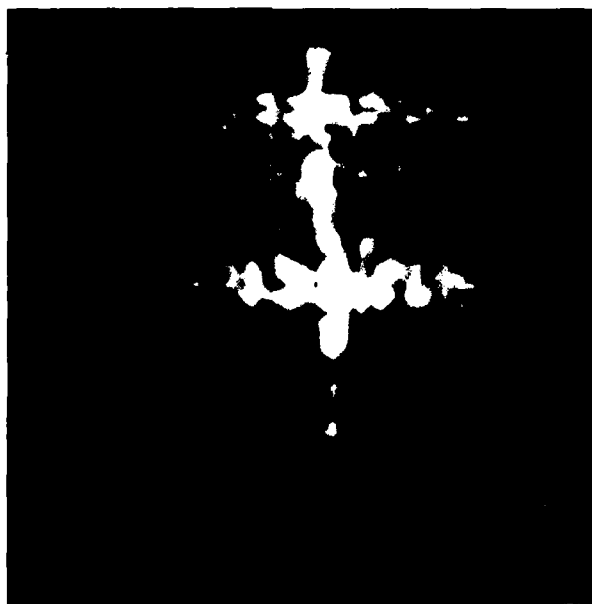
F-5E

Figure 5. Plan views of F-15 and F-5E nose aspects.
0.6M range resolution
0.45M cross range resolution
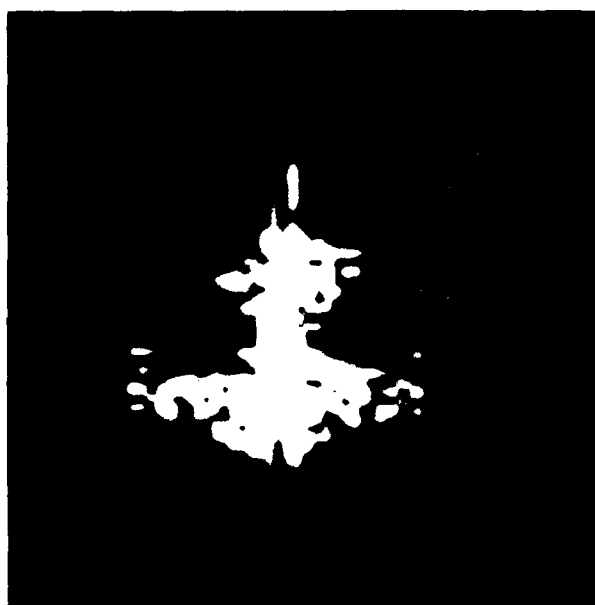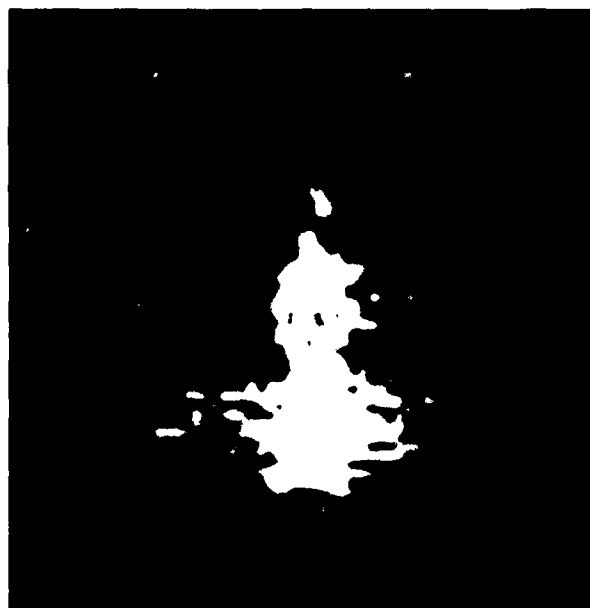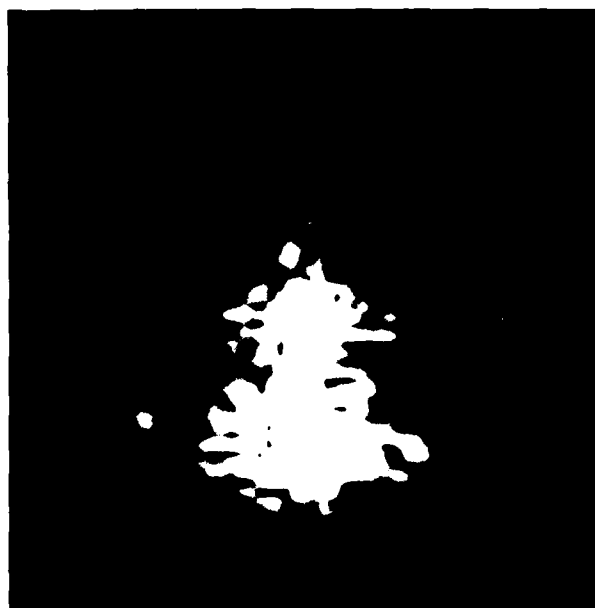
Figure 6. Plan views of F-16 for aspect
(1) 15° composite view
(2) 25° composite view
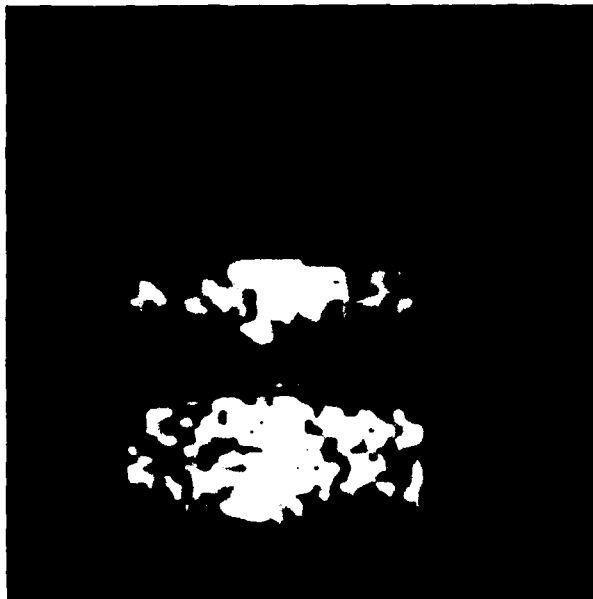
Figure 7. Plan views of YF-16 for three aspects.
0.6m range resolution.
0.45m cross range resolution.
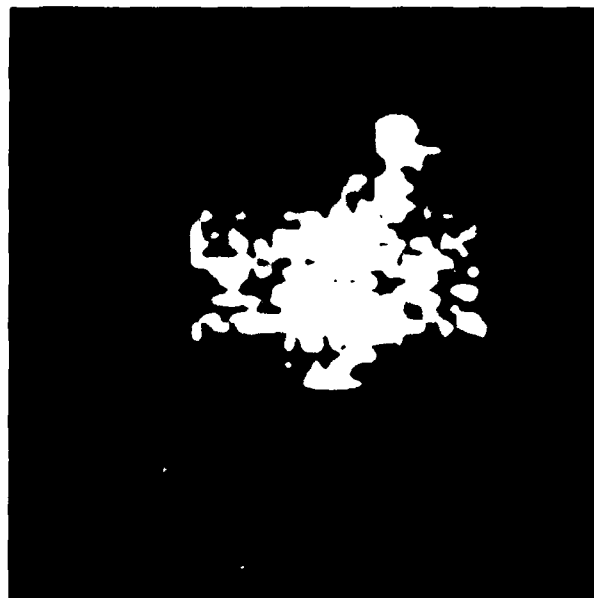
Figure 8 Plan views of A-10 nose aspects
0 6M range resolution
0 45M cross range resolution

Figure 9   Profiles of F-5E nose aspects
0.6M range resolution
0.45M cross range resolution

Figure 10. Profiles of A 10 for nose aspect with
0.6M range and 0.45 cross range resolution

caused by the changing target range during transmission of a single N frequency pulse burst.

As shown in Figure 11 when the imaging radar employs pulse-to-pulse frequency stepping to synthesize a high range resolution target profile, the received target echo at each frequency can be considered as a frequency sample of the Fourier transform $F(f_k, \theta_i)$ of the target's range response multiplied by quadratic and linear phase error terms introduced by the target range R_o and target radial velocity $\dot{R}$. As seen in Figure 11, the received signal as a function of frequency f_k and aspect angle θ_i is given by

$$U(f_k, \theta_i) = F(f_k, \theta_i) \exp\left[-j\frac{4\pi}{\lambda_o} R_o\right] \exp\left[-j\frac{4\pi}{\lambda_o}(T\dot{R})i\right]$$

$$\exp\left[-j\frac{4\pi}{\lambda_o}(R_o \frac{\Delta f}{f_o} + \dot{R}\Delta T)k\right] \exp\left[-j\frac{4\pi}{\lambda_o}\left(\frac{\Delta f}{f_o}\right)(\dot{R}T)ik\right]$$

$$\exp\left[-j\frac{4\pi}{\lambda_o}\left(\frac{\Delta f}{f_o}\right)(\dot{R}\Delta T)k^2\right]. \tag{15}$$

where R_o is the target range at aspect θ_o when frequency f_o is transmitted, λ_o, is the mean radar wavelength, Δf is the frequency step size, ΔT is the pulse repetition interval (PRI) between transmissions at adjacent frequencies, and $T = N \cdot \Delta T$ is the burst time. The effect of the linear phase errors introduced by the first three complex exponentials in Equation (15) is a translation of the resulting radar image in the image plane and does not affect the image quality. But the last two complex exponential terms in Equation (15) are quadratic functions of the indices i and k and have a defocusing and blurring effect on the resulting radar image. Autofocusing algorithms attempt to correct the effect of these two quadratic phase error terms. The autofocusing algorithms used in Figure 12 to correct for the quadratic phase error involving the product of $i \cdot k$ is known as range align-ment while the correction for the quadratic error involving k^2 in Equa-tion (15) is known as quadratic phase compensation and is needed before the returns of a single burst can be Fourier transformed to obtain the high
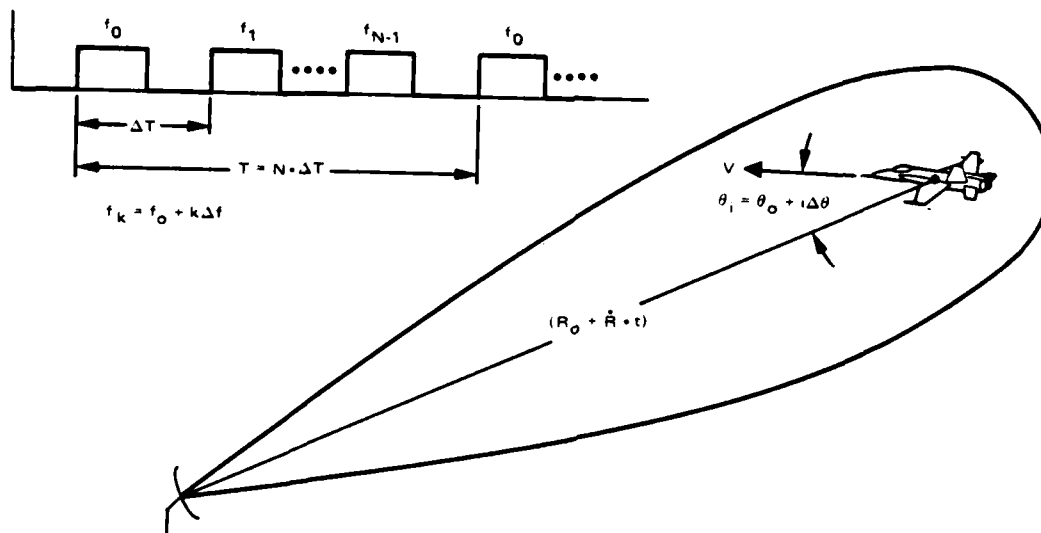
RECEIVED SIGNAL

$$U(f_k, \theta_i) = F(f_k, \theta_i) \cdot EXP\left[-j\frac{4\pi}{\lambda_0} R_0\right] \cdot EXP\left[-j\frac{4\pi}{\lambda_0} (T \cdot \dot{R}) i\right]$$

$$EXP\left[-j\frac{4\pi}{\lambda_0} (R_0 \frac{\Delta f}{f_0} + \dot{R}\Delta T) k\right] EXP\left[-j\frac{4\pi}{\lambda_0} \frac{\Delta f}{f_0} (T \cdot \dot{R}) ik\right]$$

$$EXP\left[-j\frac{4\pi}{\lambda_0} \cdot \frac{\Delta f}{f_0} (\Delta T \cdot \dot{R}) k^2\right]$$

Figure 11. ISAR imaging of target by radar using pulse to pulse frequency stepping.
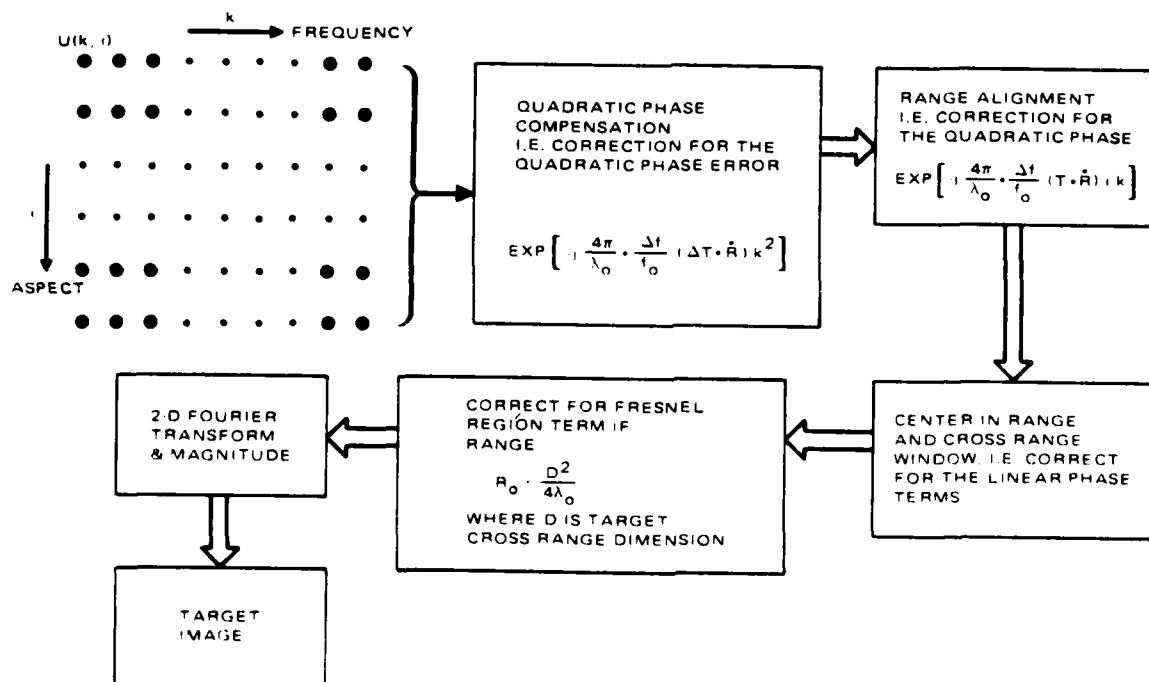
Figure 12. Signal processing functions needed in formation of ISAR images using stepped frequency technique.

range resolution profile. A signal processing block for correction of phase errors introduced by Fresnel region terms is also shown in Figure 12. This correction accounts for a quadratic phase error introduced by the assumption that the radar signals are plane waves rather than spherical waves and is only important at relatively short ranges.

When autofocusing is used for range alignment, it is usually assumed that the target's rotational motion is relatively slow in comparison to the N-pulse burst time, so that two adjacent range signatures are approximately equal. With this assumption, the problem of range alignment can be expressed as an optimization problem, where an unknown linear phase function of the form $\exp[-j(2\pi f_k d_i + \phi_i)]$ is sought so that the function

$$J = \sum_{k=0}^{N-1} \left| U(f_k, \theta_i) - U(f_k, \theta_{i-1})\, e^{-j(2\pi f_k d_i + \phi_i)} \right|^2 \tag{16}$$

is minimized.

Then the resulting value of d_i is an estimate of the (range displacement) time delay between the two range profiles at aspect angles θ_i and θ_{i+1}, and ϕ_i is a phase difference between the two profiles. In general depending on the spectral characteristics of the signal, filters $H_1(f)$ and $H_2(f)$ are introduced and the resulting criterion function becomes

$$J = \sum_{k=0}^{N-1} \left| H_1(f_k)\, U(f_k, \theta_i) - H_2(f_k)\, U(f_k, \theta_{i+1})\, \exp(-j2\pi f_k d_i - j\phi_i) \right|^2 . \tag{17}$$

Minimization of Equation (17) with respect to d_i and ϕ_i gives that the optimum value of the delay d_i is the value that maximizes

$$Q = \left| \sum_{k=0}^{N-1} W(f_k)\, U(f_k, \theta_i)\, U^*(f_k, \theta_{i-1})\, e^{j2\pi f_k d_i} \right|^2 , \tag{18}$$

where:

$$W(f_k) = H_1(f_k) H_2^*(f_k) , \tag{19}$$

is a frequency weighting that depends on the spectral characteristics of the signal and interference. For example when $W(f_k) = 1.0$ then using Parseval's theorem, it can be easily shown that the maximum value of Q is equal to the square of the maximum cross correlation peak between the two range profiles.

Once estimates for the delays d_i's and phase angles ϕ_i's are obtained, then assuming that the range rate $\dot{R}$ is approximately constant during a burst period a quadratic phase compensation can be introduced to account for range changes during one range signature time.

The above processing technique was used to generate inverse SAR images of a DC-10 during take off. The data were obtained by an S-band radar operated by NOSC in San Diego, CA. By stepping the transmitted frequency pulse to pulse at 1 MHz increments over a total bandwidth of 256 MHz, this radar obtains a synthetic high range resolution profile every 0.05 second. A total of 64 range profiles are used to form an image. Depending on the apparent target rotation (yaw or pitch) plan (top) or profile (side) view images of the target are obtained. Figure 13 is an example of the plan (top) and of the side view images for the above DC-10 generated using the processing described in Figure 12. Ten side view images of this target, 10 side view images of an F-5E and 10 images of an A-10, were used for classification tests using the method of moments. The results are presented in Section VI.

2.3 IMAGE PREPROCESSING FOR AUTOMATIC TARGET RECOGNITION

Before the radar images generated by the coherent processing of the radar returns as described in Figure 12 are presented to the classifier, an adaptive thresholding scheme is used to remove noise in the images. Furthermore, the edge detection scheme of Figure 14 is used to generate image boundaries. As seen in that figure the background noise level of the image is computed, and a threshold corresponding to 4.4 dB above the
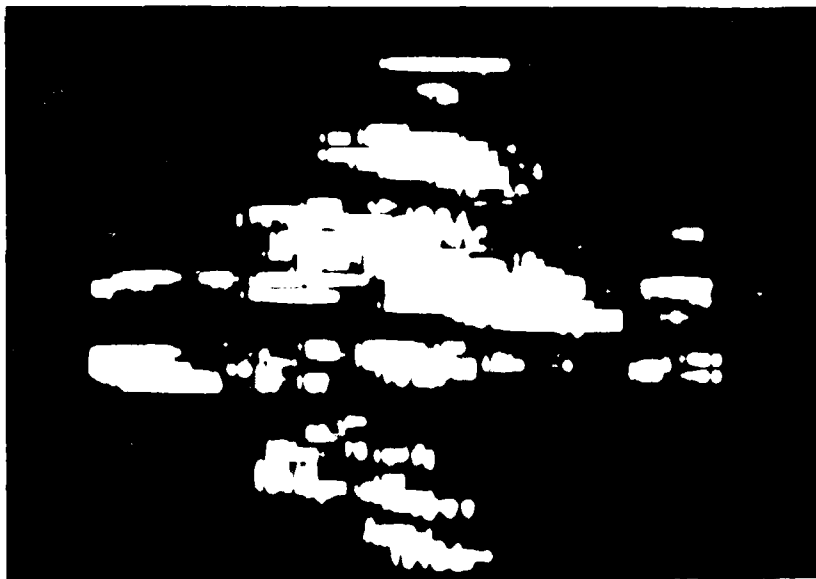
a. DC-10 TOP VIEW

Figure 1.5 AA DC-10 during takeoff
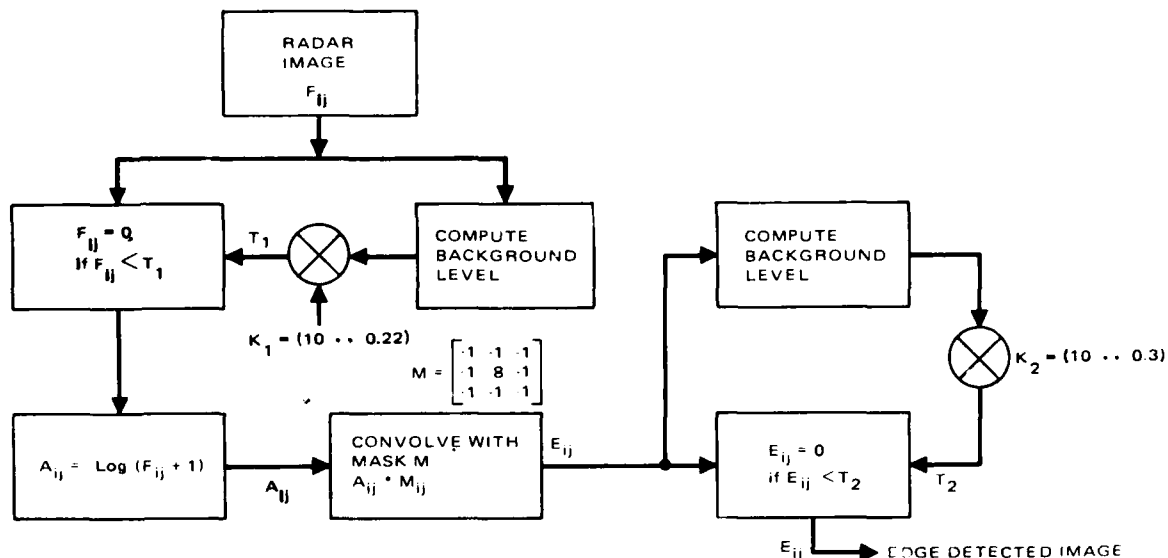
Figure 14. **Processing for edge detection.**

background noise level is used. Then the resulting image is used to obtain
the image edges as shown in Figure 14. As seen the dynamic range
the thresholded image intensity is reduced using the transformation
$A_{ij} = \log(F_{ij}+1)$ where F_{ij} is the original image intensity. The resulting
image intensity field A_{ij} is then convolved with an edge detection mask M
to generate the field $E_{ij} = M * A_{ij}$. The field E_{ij} is thresholded using an
adaptive threshold set at 6 dB above the estimated background noise level
in E_{ij}. The computation of the background noise levels used in computing
the adaptive thresholds is obtained by averaging all intensities in the
observed image fields that are less than one fifth the maximum observed
intensity. Examples of radar images before thresholding, after thresholding
and after edge detection are shown in Figures 15 through 18.

All the aircraft targets used in this study are shown in Figure 19.
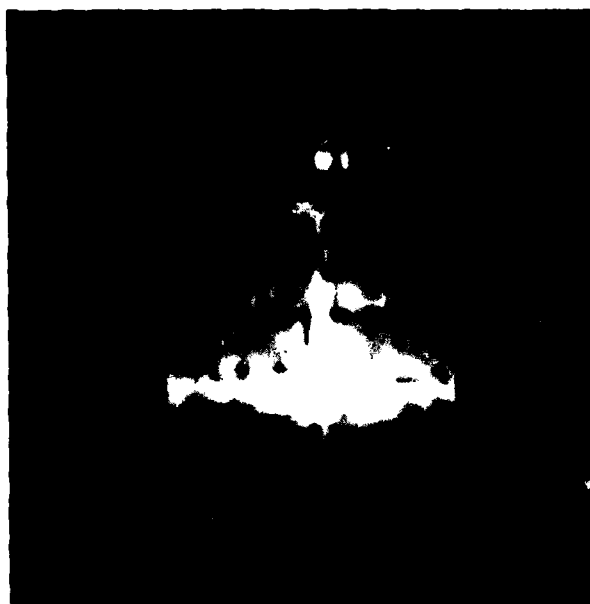
a. Original
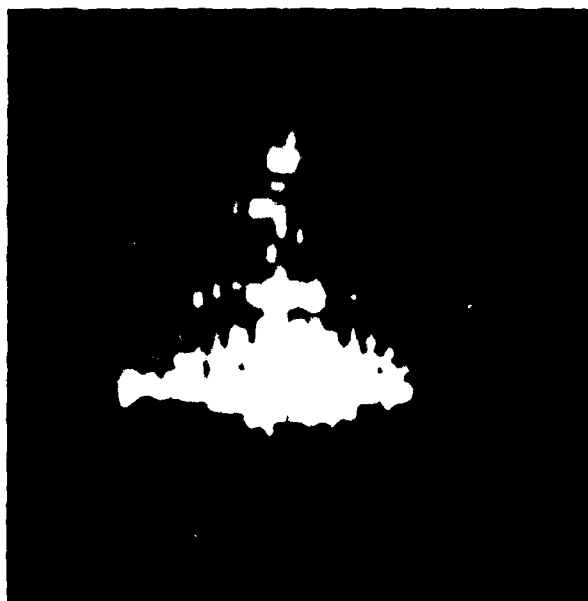
b. After thresholding
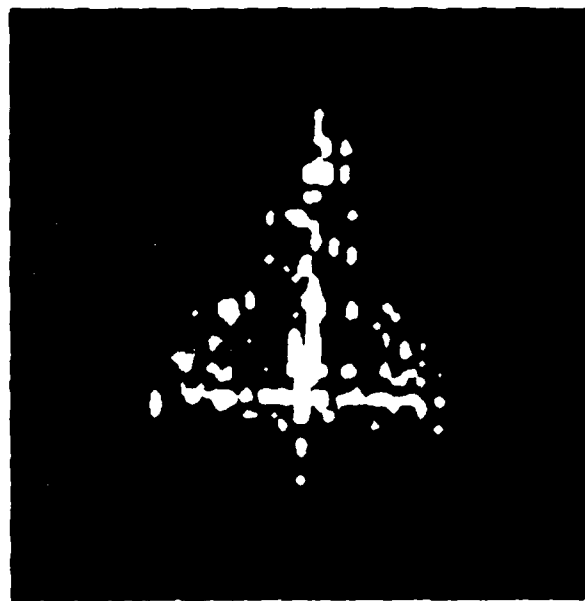
c. Edge detected

Figure 15. Plan view of F-102.
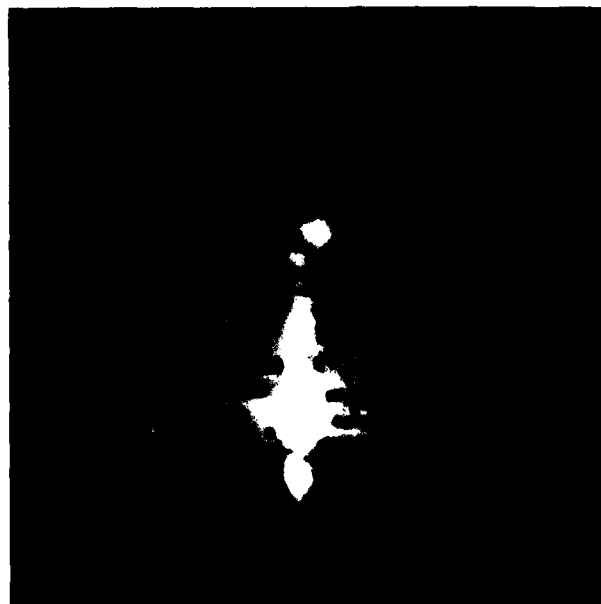
a. Original

b. After thresholding
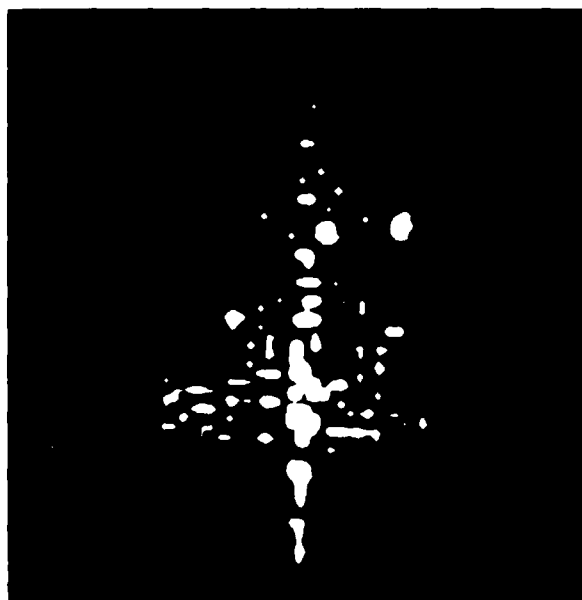
c. Edge detected

Figure 16 Plan view of F 5E.

a. Original

b After thresholding
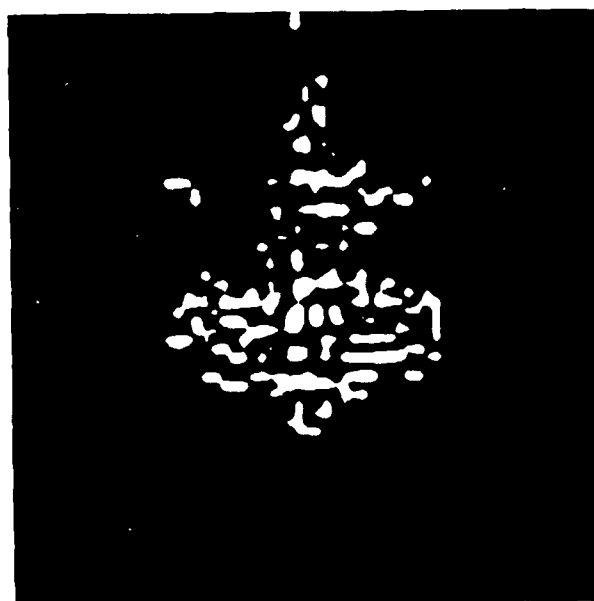
c. Edge detected

Figure 12. Plan views of F-15

44
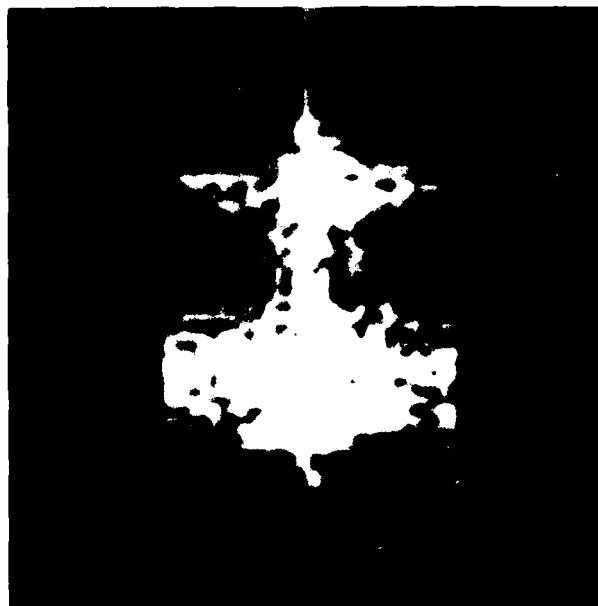
a. Original

b. After thresholding
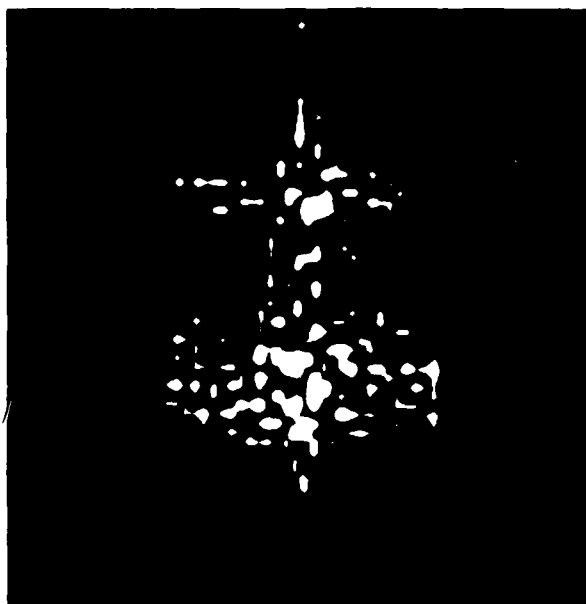
c. Edge detected

Figure 18. Plan view images of YF-16
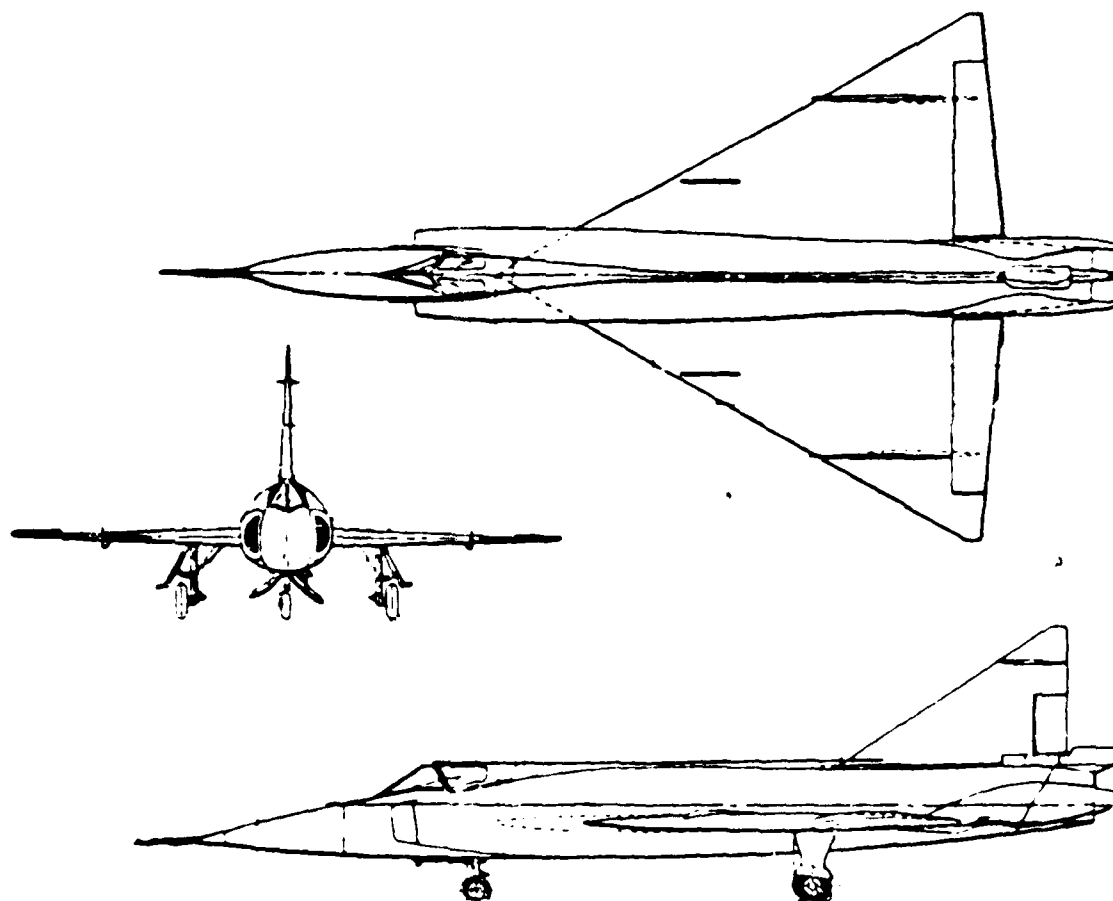
a. F-102 (LENGTH = 20.8M, WING SPAN = 11.6M)

Figure 19. Target aircraft (Sheet 1 of 4)
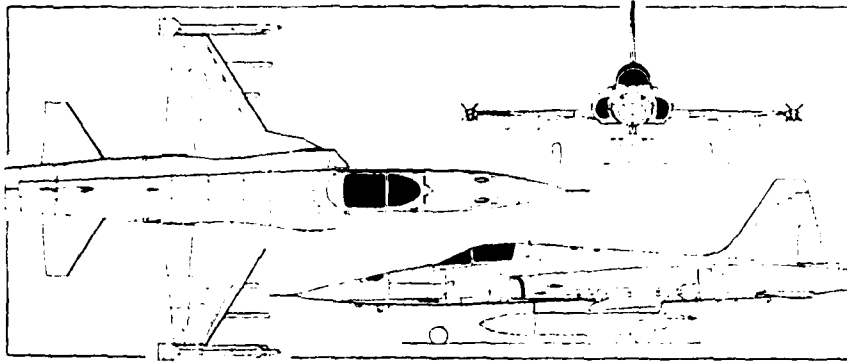
b. Northrop F-5E (length = 14.73 meters, wing span = 8.128 meters)
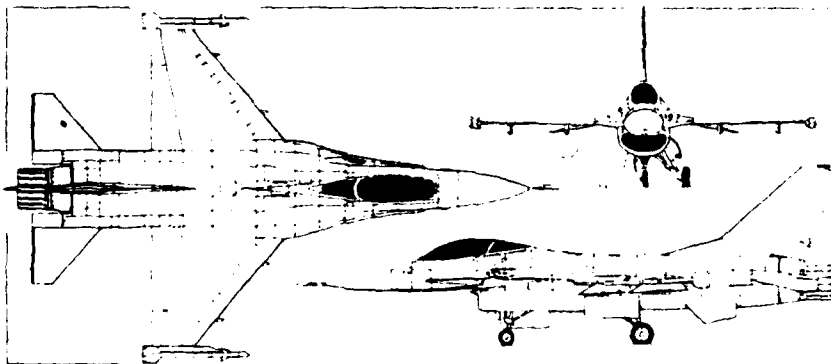
c. General dynamics F-16A (length = 14.17 meters, wing span = 10 meters)

Figure 19. Target aircraft (Sheet 2 of 4)
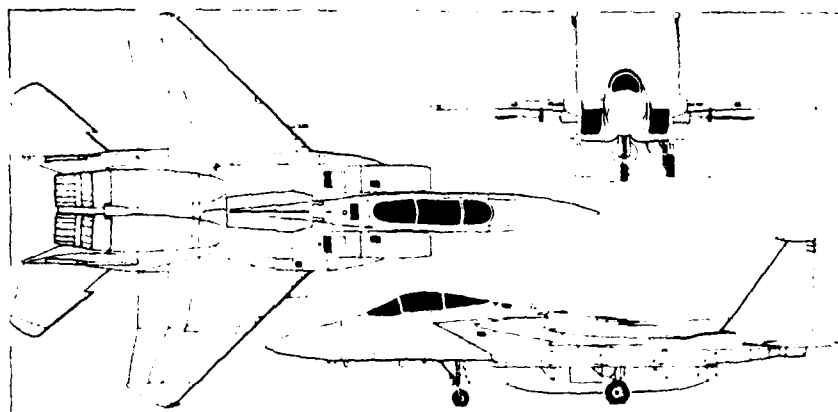
d. McDonnell Douglas F-15 (length = 19.4 meters, wing span = 13 meters)
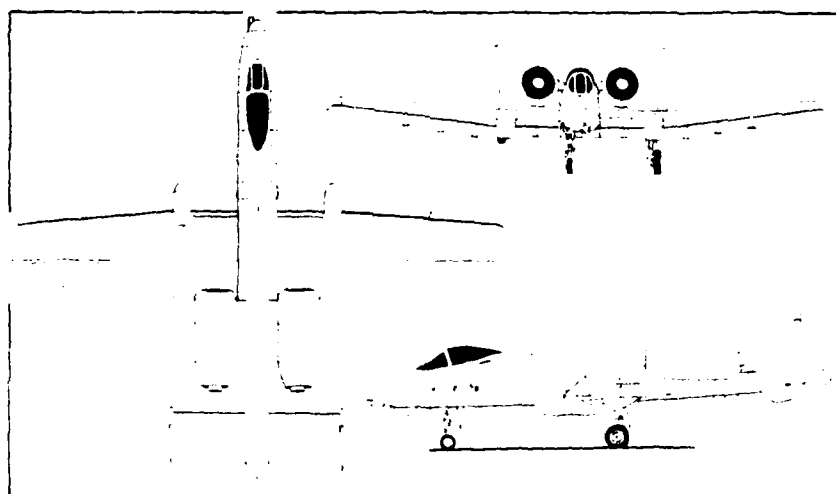
e. Fairchild Republic A-10A (length = 16.2M, wing span = 17.5M)

Figure 19. Target aircraft (Sheet 3 of 4)
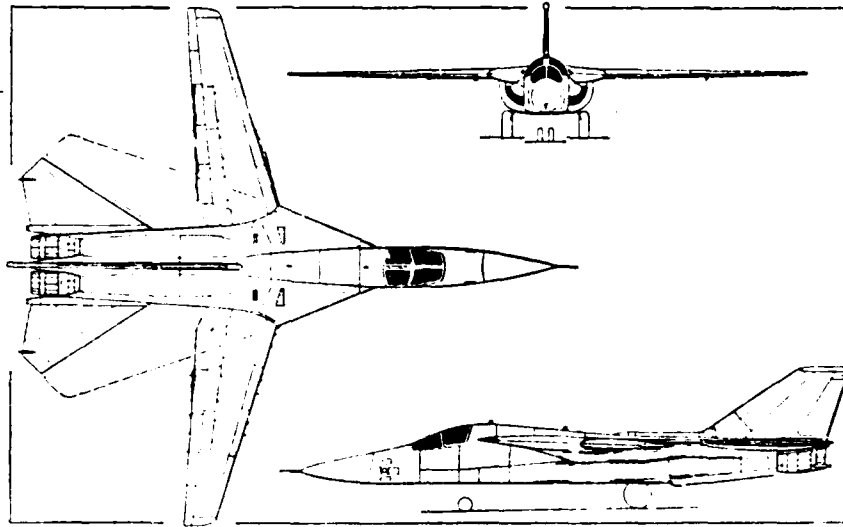
f. General Dynamics FB-111A
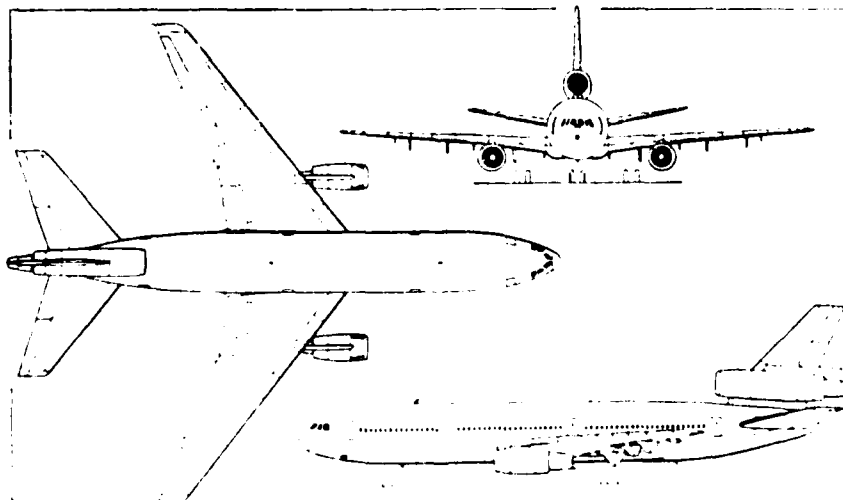
g. McDonnell Douglas DC-10

Figure 19. Target aircraft (Sheet 4 of 4)

Section III
RADAR IMAGE CLASSIFICATION USING
THE METHOD OF MOMENTS

One of the more difficult problems in the design of a recognition system for pictorial patterns is the selection of a set of appropriate numerical attributes or features to be extracted from the object of interest for classification. One set of features that has been applied successfully to the recognition of optical pictures is the set of geometric moments of the image and invariant functions of these moments [6], [7], [8], . The geometric moments and invariant moment functions and their use in classifying radar images of targets are detailed in this section.

3.1 GEOMETRIC MOMENTS AND INVARIANT MOMENT FUNCTIONS OF IMAGES

The non central $(p + q)$th order moments of an NxM rectangular image field $f(x_i, y_j)$ are defined by

$$n_{pq} = \frac{1}{N \cdot M} \sum_{i=1}^{N} \sum_{j=1}^{M} f(x_i, y_j) x_i^p y_j^q \tag{20}$$

where (x_i, y_j) are the coordinates of the (i, j) cell and $f(x_i, y_j)$ is the intensity function.

The central moments for the same rectangular image field are defined by

$$m_{pq} = \frac{1}{N \cdot M} \sum_{i=1}^{N} \sum_{j=1}^{M} f(x_i, y_j)(x_i - \bar{x})^p (y_j - \bar{y})^q \tag{21}$$

where·

$$\overline{x} = \frac{n_{10}}{n_{00}} \tag{22}$$

and

$$\overline{y} = \frac{n_{01}}{n_{00}} \ . \tag{23}$$

The normalized central moments are defined by

$$\mu_{pq} = \frac{m_{pq}}{m_{00}} \ ,$$

and are invariant with respect to changes in the image intensity. Central moments as used in this discussion are the normalized central moments defined above.

From Equation (21), the central moments are seen to be invariant under translation but vary under rotations of the image. Using the theory of algebraic invariants Hu[7] has shown that algebraic relations exist among the central moments of an image that are invariant under translation and rotation (see also Appendix A).

These invariant moment functions are of the form

$$\rho \ (m_{p_1 q_1}, \ m_{p_2 q_2}, \ \ldots \ m_{p_n q_n})$$

and are invariant under co-ordinate transformations. In particular a set of invariants known as orthogonal invariants are functions whose value does

not change under a rotation of co-ordinates, i.e., they are invariant with respect to the orthogonal transformation

$$
\begin{pmatrix} x' \\ y' \end{pmatrix} = \begin{pmatrix} \cos\theta & \sin\theta \\ -\sin\theta & \cos\theta \end{pmatrix} \begin{pmatrix} x \\ y \end{pmatrix}
\tag{24}
$$

for any angle θ, i.e.,

$$
\rho(m'_{p_1 q_1}, m'_{p_2 q_2}, \dots m'_{p_n q_n}) = \rho(m_{p_1 q_1}, \dots m_{p_n q_n})
$$

where the $m_{p_i q_i}$ are computed using the image intensity field $f(x, y)$ and the $m'_{p_i q_i}$ are computed from $f(x', y')$. When these functions are invariant under rotations and/or reflections about one of the coordinate axes they are called absolute orthogonal invariants. In what follows, by 'invariants' we refer to these absolute orthogonal invariants.

Using the theory of algebraic invariants, Hu [7] has shown that the number of invariants involving moments from second to nth order $(n = p + q)$ are the same as the number of moments with orders 2 to n which is

$$
N = \frac{(n + 4)(n - 1)}{2} \quad .
$$

In optical and infrared image recognition systems only invariant functions obtained from the second and third order moments are usually used. For these moments, there are six absolute orthogonal invariants given by

$$
\rho_0 = (\mu_{20} + \mu_{02})^{1/2} = r
\tag{25}
$$

$$
\rho_1 = \frac{1}{r^4} [(\mu_{20} - \mu_{02})^2 + 4\mu_{11}^2]
\tag{26}
$$

$$
\rho_2 = \frac{1}{r^6} [(\mu_{30} - 3\mu_{12})^2 + (3\mu_{21} - \mu_{03})^2]
\tag{27}
$$

$$\rho_3 = \frac{1}{r^6}\left[(\mu_{30} + \mu_{12})^2 + (\mu_{21} + \mu_{03})^2\right] \tag{28}$$

$$\rho_4 = \frac{1}{r^{12}}\left[(\mu_{30} - 3\mu_{12})(\mu_{30} + \mu_{12})\{(\mu_{30} + \mu_{12})^2 - 3(\mu_{21} - \mu_{03})^2\}\right.$$

$$\left. + (3\mu_{21} - \mu_{03})(\mu_{21} + \mu_{03})\{3(\mu_{30} + \mu_{12})^2 - (\mu_{21} + \mu_{03})^2\}\right] \tag{29}$$

$$\rho_5 = \frac{1}{r^8}\left[(\mu_{20} - \mu_{02})\{(\mu_{30} + \mu_{12})^2 - (\mu_{21} - \mu_{03})^2\}\right.$$

$$\left. + 4\mu_{11}(\mu_{30} + \mu_{12})(\mu_{21} + \mu_{03})\right] \tag{30}$$

and one skew* orthogonal invariant given by

$$\rho_6 = \frac{1}{r^{12}}\left[(3\mu_{21} - \mu_{03})(\mu_{30} + \mu_{12})\{(\mu_{30} + \mu_{12})^2 - 3(\mu_{21} + \mu_{03})^2\}\right.$$

$$\left. - (\mu_{30} - 3\mu_{12})(\mu_{21} + \mu_{03})\{3(\mu_{30} + \mu_{12})^2 - (\mu_{21} + \mu_{03})^2\}\right]. \tag{31}$$

Above ρ_1, ρ_2, ... ρ_6 have been normalized by dividing by $\rho_0 = r$ to cancel uniform scale changes. Because the quality of most radar images is not good compared to optical or FLIR images, the number of moments and invariants used in most of the classification tests of radar images described in this report is much larger than six. In particular, all invariant functions involving central moments up to order n = 7 (i. e. , a total of 33) were computed using the formulas presented in Appendix A. In the classification tests, all of the above invariants as well as smaller subsets of these invariants were used to construct feature vectors. Classification results from these tests are presented in Section VI.

Although the moment functions in Equations (25) to (31) above and those presented in Appendix A are invariant under orthogonal transformations, they are not invariant under general algebraic transformations. In particular if the apparent target rotation rate is not estimated, the cross range dimension of an inverse SAR image may not be properly scaled. The result is a

---

A skew orthogonal invariant changes sign under reflection.

distorted image, which destroys the invariance of the above moment functions. A technique for estimating the cross range scale of inverse SAR images using orthogonal invariant moment functions is discussed in Section 3.2. This technique has been tested on the turntable data but has not been proven yet on real moving target data.

To overcome this scaling problem, Hughes investigated the use of a set of moment functions that are invariant under general linear transformations provided that the determinant of the transformation matrix is unity, i.e.,

$$\begin{pmatrix} x' \\ y' \end{pmatrix} = \begin{pmatrix} a & b \\ c & d \end{pmatrix} \begin{pmatrix} x \\ y \end{pmatrix}$$

where:

$$\Delta = (ad - bc) = 1.$$

Such a set exists, and for the second and third order moments Hu [7] gives the following invariant moment functions:

$$I_0 = \mu_{02}\mu_{20} - \mu_{11}^2 \tag{32}$$

$$I_1 = (\mu_{03}\mu_{30} - \mu_{21}\mu_{12})^2 - 4(\mu_{03}\mu_{21} - \mu_{12}^2)(\mu_{12}\mu_{30} - \mu_{21}^2) \tag{33}$$

$$I_2 = \mu_{02}(\mu_{12}\mu_{30} - \mu_{21}^2) - \mu_{11}(\mu_{03}\mu_{30} - \mu_{12}\mu_{21}$$

$$- \mu_{20}(\mu_{03}\mu_{24} - \mu_{12}^2) \tag{34}$$

$$I_3 = \mu_{03}^2\mu_{20}^3 - 6\mu_{03}\mu_{12}\mu_{11}\mu_{20}^2 - 6\mu_{03}\mu_{21}\mu_{20}(2\mu_{11}^2 - \mu_{02}\mu_{20})$$

$$+ \mu_{03}\mu_{30}(6\mu_{02}\mu_{11}\mu_{20} - 8\mu_{11}^3) + 9\mu_{12}^2\mu_{02}\mu_{20}^2$$

$$- 18\mu_{12}\mu_{21}\mu_{02}\mu_{11}\mu_{20} - \mu_{12}\mu_{30}\mu_{02}(2\mu_{11}^2 - \mu_{02}\mu_{20}) \tag{35}$$

$$+ 9\mu_{21}^2\mu_{02}^2\mu_{20} - 6\mu_{21}\mu_{30}\mu_{11}\mu_{02}^2 + \mu_{30}^2\mu_{02}^3$$

41

These can be normalized to generate a set of general algebraic invariants given by

$$\eta_0 = 1$$

$$\eta_1 = I_1/I_0^3 \tag{36}$$

$$\eta_2 = I_2/I_0^2 \tag{37}$$

$$\eta_3 = I_3/I_0^3 \tag{38}$$

Using the theory of algebraic invariants a much larger set of general algebraic invariants can be derived. However in this investigation the feature vectors that were considered consist only of the above three invariant functions as well as the squares and by two products of these invariants as described in Section VI. In general, moments and invariants were computed from both the intensity modulated image and from the edge detected image obtained by the image preprocessing described in Section 2.3.

3.2 COMPUTATION OF TARGET ASPECT AND CROSS RANGE SCALING USING THE GEOMETRIC MOMENTS

If the rotationally invariant moment functions are used as features for classification, the target orientation in the imaging plane does not have to be computed. However, if that orientation is desired so that other recognition techniques, which need that information, can also be applied, the central moments can be used to give the target orientation as shown in Figure 20. It is shown in the figure that by fitting an ellipse to the aircraft image, the orientation of the major axis, which usually coincides with the fuselage, can be obtained from (see Hu [7])

$$\tan 2\theta = \frac{2\mu_{11}}{(\mu_{20} - \mu_{02})} . \tag{39}$$

where θ is the angle of this axis with the horizontal (x-axis).
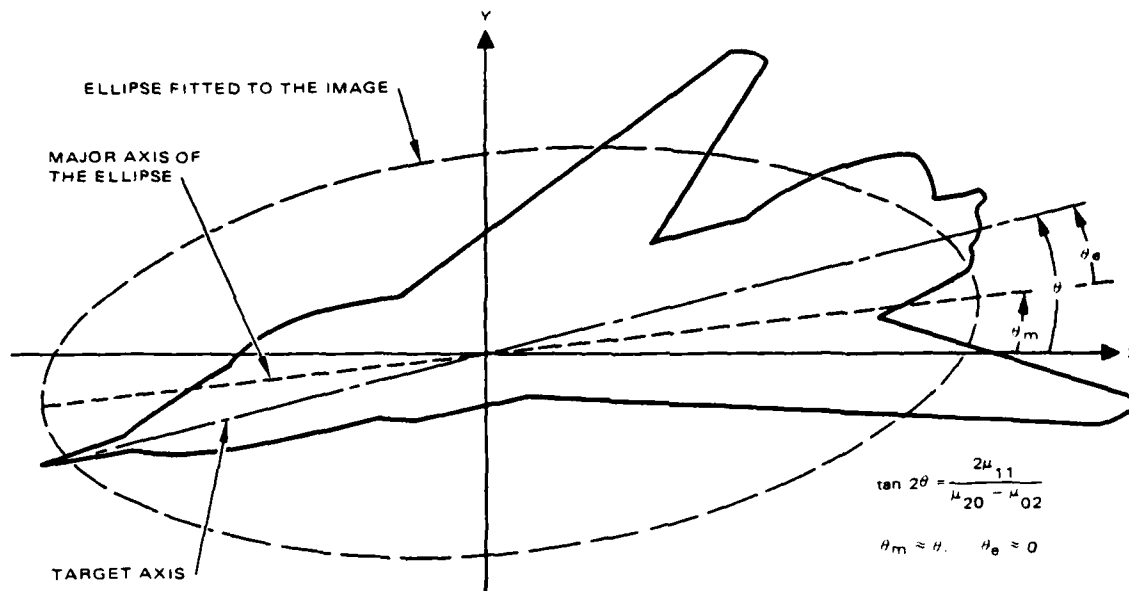
Figure 20.. Computation of fuselage orientation by fitting ellipse to target image.

In this study the performance of the above formula in estimating the target aspect angle was tested using the images of the five RATSCAT targets. The results are presented in Figure 21 in the form of a histogram that plots frequency of occurrence versus error in orientation angle estimate. A total of 3o images per target covering aspect angles from 0 degree (nose on) to 180 degrees (tail) were used in constructing the plot in Figure 21.

A problem that often arises in processing inverse SAR (ISAR) images is the determination of the scale factor to be used in converting relative cross range doppler bin numbers into absolute cross range units. For the range dimension such a scale factor is readily available from the radar range resolution cell. The computation of the equivalent range cell size along the cross range direction, however, requires knowledge of the rotation rate of the target about its centroid and is given by

$$q = \frac{\lambda}{2\dot{\Phi}\tau} \tag{40}$$

43

$$\frac{\Delta\theta}{\sqrt{2\pi}\sigma} \cdot e^{-\frac{|\Delta\theta|^2}{2\sigma^2}}$$

$$\sigma \cong 10.2^\circ$$

$$\theta_{BIAS} \cong 3^\circ$$
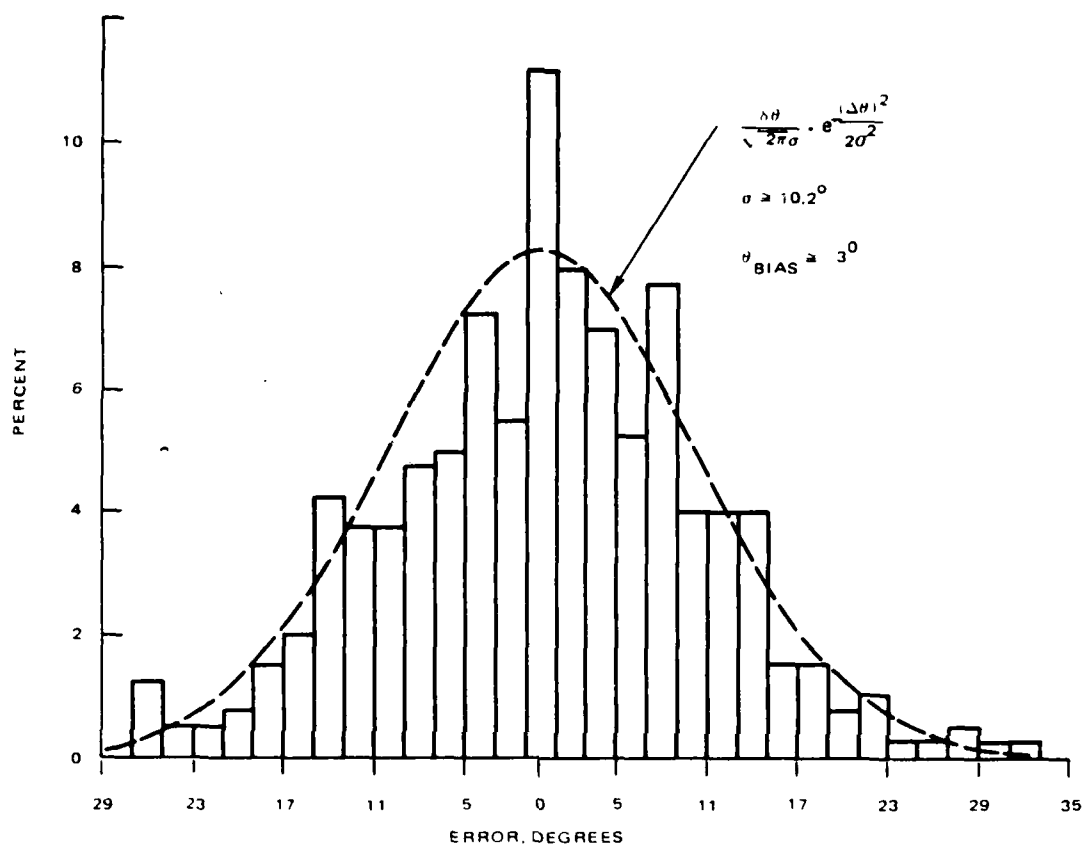
Figure 21. Aspect angle error distribution over all aspects for five RATSCAT targets.

where λ is the radar wavelength in meters, T is the time interval over which the target's doppler history is observed in forming the ISAR image, and $\dot{\phi}$ is the rotation rate of the target. Therefore, to use Equation (40) for the computation of the cross range scale factor d, the rotation rate $\dot{\phi}$ of the moving target must either be known or estimated from the radar data. Presently the lack of a good method for estimating the rotation rate of a moving target about its center imposes a major problem in the formation of properly scaled ISAR images.

During this study a technique was developed that allows the cross range dimension to be scaled without knowledge of the rotation rate. The method is based on the use of invariant moment functions of the image as described below.

44

If successive ISAR images of a rotating radar target are mapped on a plane so that the x-coordinate is along the range direction (i.e., the radial direction from the radar to the target) and the y-coordinate is along the cross range direction, as shown in Figure 22, then the above invariant moment functions can be used to compute the ratio of the cross range to range cell size.

Denoting this ratio by r, i.e.,

$$r = \frac{DY}{DX} ,$$

(41)

where DY is the cross range cell size and DX is the range cell size the orthogonal invariant moment functions are shown to be polynomials in r. For example, the invariant ρ_0 of Equation (25) can be expressed as

$$\rho_0 (r) = \mu_{20} + r^2 \mu_{02}$$

(42)
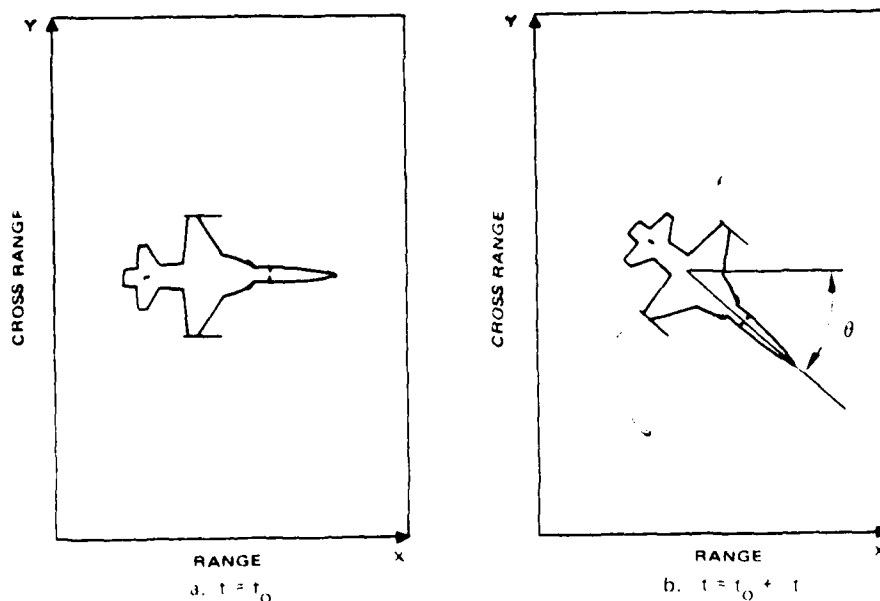
Figure 22. Two successive ISAR images rotated with respect to each other by angle θ

if μ_{20} and μ_{02} are computed by assuming that the cross range cell size DY is equal to the range cell size DX. Similarly from Equation (26)

$$\rho_1(r) = \mu_{02}^2 r^4 + 2\mu_{11}^2 r^2 + 2\left(\mu_{11}^2 - \mu_{20}\mu_{02}\right)r^2 + \mu_{20}^2 . \tag{43}$$

If the above normalized central moments from two successive inverse SAR images as shown in Figure 22 are computed by assuming that the range and cross range cell sizes are equal and if the moment from the first image are denoted by μ_{pq} and those from the second by μ'_{pq} and the corresponding invariants are denoted by ρ_i and ρ'_i, then for the correct value of the ratio r

$$\rho_i(r) = \rho'_i(r) \tag{44}$$

for all i. Thus, Equation (44) can be used to obtain the correct value of the cross range scale factor. To overcome the effects of noise, usually several invariant moment functions have to be used and an average value of the resulting values of r is computed as described below in a numerical example.

Application of Equation (44) to successive ISAR images as shown in Figure 22 gives

$$\left(\mu_{02} - \mu'_{02}\right) r^2 = \left(\mu'_{20} - \mu_{20}\right) \tag{45}$$

and

$$\left(\mu_{02}^2 - \mu'^2_{02}\right) r^4 + 2\left(\mu_{11}^2 - \mu'^2_{11}\right) r^2 + 2\left[\left(\mu_{11}^2 - \mu_{20}\mu_{02}\right)\right.$$

$$\left. - \left(\mu'^2_{11} - \mu'_{20}\mu'_{02}\right)\right] r^2 + \left(\mu_{20}^2 - \mu'^2_{20}\right) = 0 \tag{46}$$

Equation (46) can be simplified further using the fact that

$$\left(\mu_{11}^2 - \mu_{20}\mu_{02}\right)$$

is an absolute algebraic invariant (see Hu [7]), i.e., it is invariant under both rotations and nonuniform scale changes if the determinant of the transformation is unity. Using this result, Equation (46) gives

$$\left(\mu_{02}^2 - \mu'_{02}^2\right) r^4 + 2\left(\mu_{11}^2 - \mu'_{11}^2\right) r^2 + \left(\mu_{20}^2 - \mu'_{20}^2\right) = 0 \qquad (47)$$

Substitution from Equation (45) into the term

$$\left(\mu_{02}^2 - \mu'_{02}^2\right) r^4 \text{ of equation (3-28)}$$

gives

$$\left(\mu_{02} + \mu'_{02}\right)\left(\mu'_{20} - \mu_{20}\right) r^2 + 2\left(\mu_{11}^2 - \mu'_{11}^2\right) r^2 + \left(\mu_{20}^2 - \mu'_{20}^2\right) = 0 \qquad (48)$$

As mentioned earlier in the absence of noise, Equations (45) and (48) must have at least one common positive root. Usually when noise is present, this is not true and the two roots given by

$$r_1 = \left(\frac{\mu'_{20} - \mu_{20}}{\mu_{02} - \mu'_{02}}\right)^{1/2} \qquad (49)$$

(from Equation (45)) and

$$r_2 = \left[\frac{\left(\mu'^2_{20} - \mu^2_{20}\right)}{2\left(\mu^2_{11} - \mu'^2_{11}\right) - \left(\mu'_{20} - \mu_{20}\right)\left(\mu_{02} + \mu'_{02}\right)}\right]^{1/2} \qquad (50)$$

(from Equation (48)) are not equal or even real. In the Hughes computer study of the performance of the above technique to real data, the above two roots were used together with a root obtained by combining Equations (27) and (28) to obtain an invariant given by $(\rho_5 - \rho_2)$. This root is given by

$$r = \left[\frac{\left(\mu'^2_{21} - \mu'_{12}\right) - \left(\mu^2_{21} - \mu_{12}\right)}{\left(\mu^2_{12} - \mu_{21}\right) - \left(\mu'^2_{12} - \mu'_{21}\right)}\right]^{1/2} \qquad (51)$$

In combining these roots, only the positive ones are considered. To give equal weight to those with r < 1 as to those with r > 1, the geometric rather than the algebraic mean was used; i.e.,

$$\bar{r} = (r_1 \, r_2 \, r_3)^{1/3} \tag{52}$$

which is equivalent to averaging of the logarithm of the above roots.

The above method was used to compute the ratio of the range to cross range scale factor of a set of ISAR images obtained from multifrequency step S-band data for a scaled model of the F-5E. The data were recorded at the RATSCAT facility where the target was placed on a turntable and slowly rotated at a known rate. Using Equation (40) and the known rotation rate, the cross range cell size for the images was computed. The ratio of this cell size to the radar range resolution cell for the images was equal to 0.816.

Smoothed estimates of the above ratio using successive images of the rotating target are given in Table 2. These images were formed for target aspects ranging from 180 degrees (tail aspect) to 126 degrees. The target rotation between successive images was 3 degrees. From the results in this table, the cross range scale factor is estimated to within a 28 percent accuracy. This improvement is significant when compared to the previous complete lack of any knowledge of the cross range cell size dimension. The accuracy to within the cross range scale factor is estimated using this technique will probably be adequate to allow the use of moments for the automatic classification of aircraft targets. However, no tests were performed in this study to verify this assumption.

1.02
0.966
0.901
0.736
1.05
0.583
0.705
0.763
0.786
0.774
0.873
0.868
0.749
0.742
0.780
0.590
0.688
0.583

TABLE 2. COMPUTED RATIO OF CROSS RANGE TO RANGE SCALE FACTOR USING PLAN VIEWS OF THE F-5E.

(Correct Value is 0.816)

Section IV
RANGE IMAGE CLASSIFICATION USING RANGE
AND CROSS RANGE COLLAPSING

In addition to feature vectors computed from the geometric moments
of the image feature vectors obtained by collapsing the image intensities along
two orthogonal axes are also tested. Using the three second order moments
μ_{02}, μ_{20} and μ_{11} the orientation of the target in the image plane is computed
from Equation 39 and the images are rotated so that the same orientation
is used for all images. The intensity distribution of the rotated images is
then averaged along the Y and X axes to produce average X-axis and Y-axis
intensity profiles as shown in Figure 23. The correlation functions of the
X-axis and the Y-axis intensity profiles are computed and used to construct
a feature vector as shown in Figure 23. The performance of this feature
vector was tested using the radar images generated in Section II and the
results are presented in Section VI.
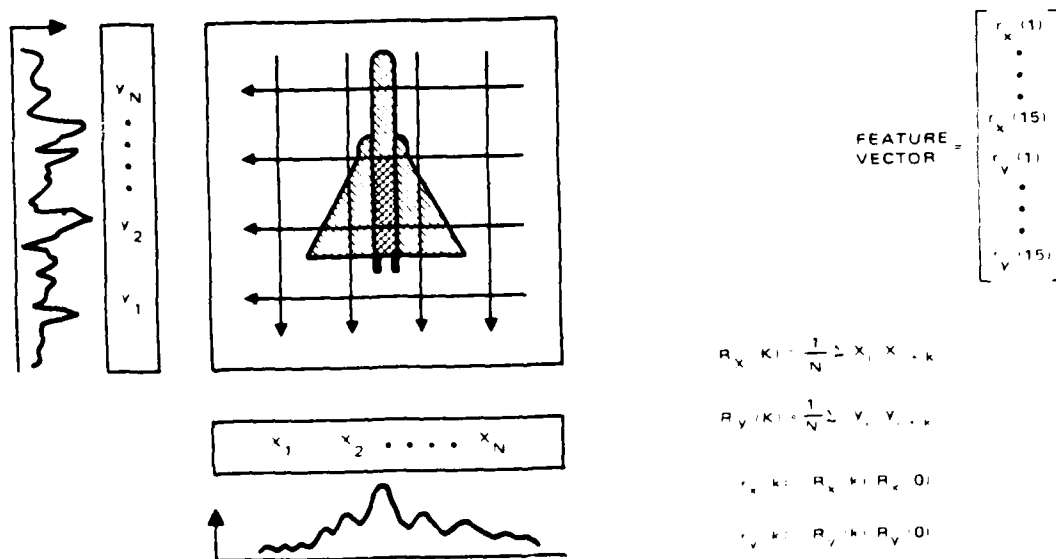
Figure 23 Computation of feature vector using range and cross range collapsing

Section V
CLASSIFIER DESIGN AND OPTIMUM FEATURE SELECTION

The classifier algorithm uses the above measured feature vectors to classify the target into one of M possible target classes. A review of the literature on pattern recognition shows that many techniques can be used to design such classifiers. Among the most common are the nearest neighbor, maximum likelihood, linearized Bayes, and Fisher's linear discriminant technique. The performance of classifiers, designed using the above techniques, depends on the available learning samples and the particular classification problem. Since this investigation is primarily concerned with the analysis of the performance of feature vectors computed using the method of moments, no elaborate classifier designs are attempted. Instead two classifiers are used: the Kth nearest neighbor and the Gaussian classifier. These two classifiers and two schemes used in reducing the dimensionality of the feature vectors are described in this section.

5.1 Kth NEAREST NEIGHBOR CLASSIFIER

The nearest neighbor classifier decides that a measured feature vector X belongs to target T_j if

$$\| X - X_n^{(j)} \| = \min_{i, k} \| X - X_k^{(i)} \| \tag{53}$$

where:

$X_k^{(i)}$ a measured feature vector for target i at the kth aspect angle and $\| X \|$ denotes the norm of X.

The K nearest neighbor classifier classifies the measured feature vector X to the class that represents the majority among the K nearest neighbors.

A generalization of the Kth nearest neighbor classifier is the distance weighted Kth nearest neighbor used for many of the classification tests described in Section VI. To classify a measured feature vector X using this classifier the K nearest neighbors of X are found from the training set $\{X_1, X_2 \ldots X_K\}$ and are ordered so that their distances $d_i = \|X - X_i\|$ from X are increasing

$$d_1 < d_2 < \ldots < d_K .$$

Using these distances, a set of weights W_j's are computed as follows.

$$W_j' = \frac{d_K - d_j}{d_K - d_1} \qquad d_K \neq d_1 \tag{54}$$

$$W_j' = 1 \qquad iff \qquad d_K = d_1 . \tag{55}$$

These weights are then normalized so that their sum is equal to unity

$$W_j = \frac{W_j'}{\sum_{j=1}^{K} W_j'} . \tag{56}$$

Using the weights W_j a set of class weights $W^{(m)}$, $m = 1, 2, \ldots M$ for the M possible target classes $[C_1, C_2, \ldots C_M]$ are computed from

$$W^{(m)} = \sum_{X \in C_m} W_j . \tag{57}$$

Since

$$\sum_{j=1}^{K} W_j = \sum_{m=1}^{M} W^{(m)} = 1.0$$

the class weights $W^{(m)}$ can be considered as an estimate of $p(X/C_m)$, and the unknown target is identified as target C_m if

$$W^{(m)} = \max_n W^{(n)} > p \tag{58}$$

where $0 \leq p < 1$ is a threshold used for the decision of unknown; i.e., if $\max_n (W^{(n)}) < p$ an unknown is declared.

To reduce the computations required for this classification scheme, a technique developed by Friedman, et al. [a], is used. According to their algorithm, the set of feature vectors from all the classes are sorted on the values of one of the coordinates. Then for each test vector, the training feature vectors are examined in the order of their projected distance from the test vector on the sorted coordinate. When this projected distance becomes larger than the distance to the Kth closest vector of those training vectors already examined the search stops, the K closest vectors of those already examined are those for the entire training set.

5.2 GAUSSIAN CLASSIFIER

The Gaussian classifier is a maximum likelihood classifier under the assumption that as the target aspect varies the measured feature vectors X are random vectors distributed according to the multivariate Gaussian density. Under this assumption, the classification algorithm is reduced to the computation of a quadratic discriminant function given by

$$D(X) = -\frac{1}{2} \ln S - \frac{1}{2} (X - \bar{X})^T S^{-1} (X - \bar{X}) \tag{59}$$

where the $|\cdot|$ indicates the "determinant of ", $\overline{X}_j$ is an estimate of the mean value of the feature vector X for the jth target and S_j is an estimate of the covariance matrix of X for the jth target. To obtain these estimates, a set of N learning samples of the feature vector X is used to represent each target over a range of aspect angles. This set of feature vectors is represented by

$$X_i^{(j)} \quad , \quad \left\{ \begin{array}{l} i = 1, \ 2, \ \ldots, \ N \\ j = 1, \ 2, \ \ldots, \ K \end{array} \right\}$$

where N is the number of aspects and $j = 1, \ 2, \ \ldots,$ K indicates the class or target (C_j) membership. Using this training set, the target means are computed by

$$\overline{X}_j = \frac{1}{N} \sum_{i=1}^{N} X_i^{(j)} \qquad j = 1, \ 2, \ \ldots, \ K \, , \tag{60}$$

and the target scatter or covariance matrices are

$$S_j = \frac{1}{N} \sum_{i=1}^{N} (X_i^{(j)} - \overline{X}_j)(X_i^{(j)} - \overline{X}_j)^T \, . \tag{61}$$

Using these estimates of the mean and covariance of the feature vector for each target, the quadratic discriminants $D_i(X)$ i = 1,....K of Equation (59) are evaluated for X equal to the measured feature vector. The feature vector is then assigned to target C_j if

$$D_j(X) \geq D_i(X) \qquad \text{for all } i. \tag{62}$$

To allow for the rejection of an unrecognizable feature vector, two additional tests are performed before the vector X is assigned to target C_j. The first test is based on Hotelling's generalized T^2 statistic, [10] which is given by

$$T^2 = (X - \overline{X}_j)^T S_j^{-1} (X - \overline{X}_j) \tag{63}$$

If the dimensionality of the feature vector X is M and if N training vectors are used in computing the mean $\overline{X}_j$ and covariance S_j for class C_j then the statistic

$$\left(\frac{N - M}{NM}\right) T^2$$

is distributed according to the central F_{ν_1, ν_2} distribution with $\nu_1 = M$ and $\nu_2 = N-M$ degrees of freedom [10], [11]. So for a confidence interval $(1 - \alpha) = \beta$

$$T^2 \leq \frac{N \cdot M}{N - M} F_{M, N-M} (1-\alpha) \tag{64}$$

For example, using tabulated values of the F distribution [12], the results are that if the dimensionality of the feature vector is 12 and if 18 training vectors are used then for a 97.5 percent confidence interval, $(F_{12, 6}(0.975) = 5.37)$

$$T^2 \leq \frac{18 \times 12}{6} \times 5.37 = 193.32$$

If the training set is increased to 27 feature vectors, then for the same confidence interval $(F_{12, 15}(0.975) = 2.96)$

$$T^2 \leq 64.8 .$$

Thus this test is used to reject a feature vector X that does not fall within a prescribed confidence region centered at the class whose discriminant function

is maximized by X. The second test is used to safeguard against misclassification of feature vectors that have a high probability of belonging to more than one class and is based on the cost to reject as compared to the loss incurred for making a substitution error. Assuming that the observed feature vector X is to be assigned to one of K classes and denoting by a_i for $i = 1 \ldots K$ the action of choosing class C_i and by a_{K+1}, the action of rejection, then if $\lambda(a_i/C_j)$ is the loss incurred for choosing action a_i when class C_j is present, the Bayes risk is given by

$$R(a_i/X) = \sum_{j=1}^{K} \lambda(a_i/C_j) \, p(C_j/X) .$$

(65)

Assuming that all classes are equiprobable and that

$$\lambda(a_i/C_j) = \begin{cases} 0 & i = j \quad i, j = 1, \ldots K \\ \lambda_r & i = K + 1 \\ \lambda_s & \text{otherwise} \end{cases}$$

(66)

and using the Bayes rule:

$$p(C_j/X) = \frac{p(X/C_j) \, P(C_j)}{p(X)} \quad ,$$

the resulting risk functions satisfy the relation

$$\frac{R(a_i/X)}{R(a_{K-1}/X)} = \frac{\lambda_s}{\lambda_r} \left[1 - \frac{p(X/C_i)}{\sum_{i=1}^{K} p(X/C_i)} \right]$$

(67)

for $i = 1, 2 \ldots K$.

From above, the selection of the action that minimizes the Bayes risk is equivalent to the selection of class C_i if

$$p(X/C_i) \geq p(X/C_j) \text{ for } j = 1, \ldots K \tag{68}$$

and

$$\frac{p(X/C_i)}{\sum^K p(X/C_j)} > \frac{\lambda_s - \lambda_r}{\lambda_s} = q, \tag{69}$$

Otherwise, the decision to reject is optimum. Under the assumption that all classes are equiprobable application of Bayes rule gives

$$p(C_i/X) = \frac{p(X/C_i)}{\sum\limits_{j=1}^K p(X/C_j)} > q \tag{70}$$

and under the Gaussian density assumption

$$p(C_i/X) = \left\{ \sum\limits_{j=1}^K \exp\left[D_j(X) - D_i(X) \right] \right\}^{-1} \cdot q, \tag{71}$$

where $D_i(X)$ is given by Equation (59).

In summary the Gaussian classifier used in this study assigns a feature vector X to class C_j if:

1) $D_j(X) \geq D_i(X)$ for all i   (72)

$$2) \quad T^2 = (X - \bar{X}_j)^T S_j^{-1}(X - \bar{X}_j) \le \frac{NM}{N - M} F_{M, N-M}(\beta) \tag{73}$$

and

$$3) \quad p(C_i/X) = \left\{ \sum_{j=1}^{K} \exp\left[D_j(X) - D_i(X) \right] \right\}^{-1} > q \tag{74}$$

where:

$$D_j(X) = -\frac{1}{2} \ln |S_j| - \frac{1}{2} (X - \bar{X}_j)^T S_j^{-1}(X - \bar{X}_j) \tag{75}$$

M = dimensionality of X

N = number of training vectors for class C_j

β = confidence interval

and q is a threshold on the a posteriori probability $p(C_j/X)$ which can be expressed as

$$q = \frac{\lambda_s - \lambda_r}{\lambda_s} , \tag{76}$$

where λ_r is the loss incurred by the decision to reject and λ_s is the loss due to a misclassification error.

3.3 FEATURE SELECTION USING A GENERALIZED MAHALANOBIS DISTANCE

Since the processing of high dimensional feature vectors is costly in terms of computation time and computer memory requirements, the dimensionality of the feature vector should be limited to the minimum necessary to ensure proper classification. A method is described here that reduces the dimensionality of the feature vector by selecting a subset of features after ranking the features according to their importance as "good" class discriminants. The criterion used to rank the features is based on a generalized Mahalanobis distance [8] given by

$$d^2 = \text{tr}\,(W^{-1}\,B) \tag{77}$$

where:

$$W = \sum_{i=1}^{K} W_i$$

is the total within-class scatter matrix

$$B = \sum_{i=1}^{K} n_i M_i M_i^T$$

is the between-classes scatter matrix,

$$M_i = \frac{1}{n_i} \sum_{X \in C_i} X, \quad i = 1, \dots K$$

are the class means and

$$W_i = \sum_{X \in C_i} (X - M_i)(X - M_i)^T$$

are the within-class scatter matrices.

Substitution of the above relations into Equation (77) gives

$$d^2 = \sum_{i=1}^{K} n_i M_i^T W^{-1} M_i \,. \tag{78}$$

Equation (78) is used as a measure of the interclass distance. When the dimensionality of the feature vector X is less than the total number of available features, the elements of X are selected to maximize the interclass distance d^2. Since the total number of possible combinations of s features out of m available features is

$$\binom{m}{s} = \frac{m!}{(m-s)!\, s!}$$

which can be very large

$$\left(\text{for example } \binom{36}{18} = 10^{10} \right),$$

an exhaustive search is not practical. To overcome this difficulty Gonzalez and Moret [8] developed a stepwise search procedure that selects features sequentially so that at every step the selected feature together with those already selected yield a maximum of the Mahalanobis distance. This method will produce the optimal subset when the features are statistically independent. When the features are correlated, however, the interdependence of the elements of the feature vector requires that they all be considered together at every step. Thus a stepwise procedure may not always yield the optimal solution in such cases. To speed this stepwise process, Gonzalez and Moret [8] introduced a recursive procedure for updating the inverse of the total within-class scatter matrix W as new components are added to the feature vector. Without going through the details of their derivation, the result is given

$$W_{K+1} = \begin{bmatrix} W_K & z \\ \hline z^T & w \end{bmatrix} \quad \text{and} \quad M_{K+1} = \begin{bmatrix} M_K \\ \hline u \end{bmatrix}$$

$$W_{K+1}^{-1} = \left[\begin{array}{c|c} U & V \\ \hline V^T & \beta \end{array} \right]$$

$$\beta = (w - Z^T W_K Z)^{-1}, \quad V = -\beta W_K^{-1} Z$$

$$U = W_K^{-1} + \beta(W_K^{-1} Z)(W_K^{-1} Z)^T$$

$$d_{K+1}^2 = M_{K+1}^T W_{K+1}^{-1} M_{K+1} = \underbrace{M_K^T W_K^{-1} M_K}_{} + \underbrace{(M_K^T W_K^{-1} Z - \mu)^2}_{} \quad (5\text{-}27)$$

which can be written as

$$d_{K+1}^2 = d_K^2 + \Delta d_{K+1}^2 . \quad (79)$$

Above K is the iteration index that should not be confused with the subscript _i_ in Equation (78) indicating class membership. To obtain the overall increment in d^2 (over all classes) of Equation (78), the increment of Equation (79) must be summed over all the classes. Thus in selecting an additional feature at each step, only the above increment in d^2 need be considered.

5.4 DIMENSIONALITY REDUCTION BY PROJECTING THE FEATURE VECTOR INTO A LOWER DIMENSIONAL SUBSPACE

In many cases where all components of the feature vector are available, a linear transformation can be used to reduce the dimensionality of the feature vector. Thus this technique selects a subset of derived features that are linear combinations of all available features. One advantage of this scheme over the previously described selection procedure is that all of the original features contribute to the derived lower dimensional feature vector. A disadvantage is that all original features must be computed or measured.

Since for a K class problem a K dimensional feature vector is adequate for classification, an (M x K) matrix H is introduced to transform the original M-dimensional feature vector X into a K dimensional feature vector Y by letting

$$Y = H^T X \qquad (80)$$

The matrix H is chosen so that the derived feature vectors Y from the kth class for $k = 1, 2, \ldots K$ cluster around the points

$$E_k = K \begin{bmatrix} 0 \\ \vdots \\ 0 \\ 1 \\ 0 \\ \vdots \\ 0 \end{bmatrix} \longleftarrow \text{kth element} \qquad (81)$$

in K dimensional space.

If the training set consists of feature vectors

$$X_i^{(j)}, \quad \begin{Bmatrix} i = 1, 2, \ldots, N \\ j = 1, 2, \ldots, K \end{Bmatrix}$$

then the requirement that the derived feature vectors $Y_i^{(j)}$ cluster around the points E_k can be formulated as an optimization problem where a matrix H is sought so that the criterion

$$\sum_{k=1}^{K} \sum_{i=1}^{N} \left(H^T X_i^{(k)} - E_k \right)^T \left(H^T X_i^{(k)} - E_k \right)$$

is minimized.   Using the trace and the cyclic properties of the trace
operator, the above can also be written as

$$J = \sum_{k=1}^{K} \sum_{i=1}^{N} \left\{ tr(H^T X_i^{(k)} (X_i^{(k)})^T H - 2tr \, (E_K^T H^T X_i^{(k)}) + E_k^T E_k \right\} . \qquad (52)$$

If the elements of H are

$$(h_{ij}) \begin{matrix} j=1 \ldots K \\ i=1 \ldots M \end{matrix}$$

and the gradient of J with respect to H is defined by

$$\nabla J_H \triangleq \begin{bmatrix} \dfrac{\partial J}{\partial h_{11}} & - - - & \dfrac{\partial J}{\partial h_{1K}} \\ & & \\ \dfrac{\partial J}{\partial h_{M1}} & - - - & \dfrac{\partial J}{\partial h_{MK}} \end{bmatrix} ,$$

then for the optimum matrix H

$$\nabla J_H = 0 .$$

Using the identities [18]

$$\nabla_H \, tr(H^T A H) = (A + A^T) H$$

and

$$\nabla_H tr(A^T H^T B) = BA^T$$

then

$$\nabla J_H = 2 \left(\sum_{k=1}^{K} \sum_{i=1}^{N} X_i^{(k)} (X_i^{(k)})^T \right) H - 2 \sum_{k=1}^{K} \sum_{i=1}^{N} X_i^{(k)} E_k^T = 0 \tag{83}$$

Letting

$$Z = \sum_{k=1}^{K} \sum_{i=1}^{N} X_i^{(k)} E_K^T$$

then

$$Z = \left[\sum_{i=1}^{N} X_i^{(1)} \quad \sum_{i=1}^{N} X_i^{(2)} \quad \cdots \quad \sum_{i=1}^{N} X_i^{(K)} \right] \tag{84}$$

$$S = \sum_{k=1}^{K} \sum_{i=1}^{N} X_i^{(k)} (X_i^{(k)})^T \tag{85}$$

and for in Equation (83), the optimum H is given by

$$H = S^{-1} Z$$

Using this matrix H, the original feature vector X is transformed into the K dimensional vector Y given by

$$Y = H^T X$$

and both training and classification is performed using this derived feature vector Y.

Section VI
RADAR IMAGE CLASSIFICATION RESULTS

Using the imaging algorithms described in Section II, a set of 540 plane view images was formed from the RATSCAT data base (108 images per target for 1/3 scaled models of an F-102, an F-15, a YF-16, an F-5E and an A-10). As mentioned earlier the data were collected at X band against 1/3 scale models using a total of 256 frequency steps with 3.4 MHz step size. For the full size targets these measurements correspond to S-band data with a measurement bandwidth of about 256 MHz. Out of the total of 108 images per target the first 72 images for each target were obtained using the lower 128 frequency measurements covering a bandwidth of 128 MHz out of the 256 MHz measurement bandwidth while the last 36 images per target were obtained using the upper 128 frequency measurements. The resulting range resolution on the full scale targets is 1.17 meters. For each image, a 3 degree rotation of the target was used resulting in a cross range resolution of 0.95 meters on the full scale target. The images were formed over the following set of aspect angles 0 - 3 degrees, 5 - 8 degrees... 175 - 178 degrees and 2 - 5 degrees, 7 - 10 degrees, 12 - 15 degrees,..... 177 - 180 degrees for the first set of 128 frequencies and for aspects of 0 - 3 degrees, 5 - 8 degrees, ...175 - 178 degrees for the second set of 128 frequencies. Examples of these images are shown in Figures 24 through 28.

The images of the F-111 were formed by C.C. Chen [14] using data obtained with the ALCOR radar. The data were recorded from a maneuvering F-111 target aircraft using a linear FM waveform with 500 MHz instantaneous bandwidth. The resolution of the images from this target was reduced to match the resolution of the RATSCAT images. The images for this target were formed over the following aspect angles.
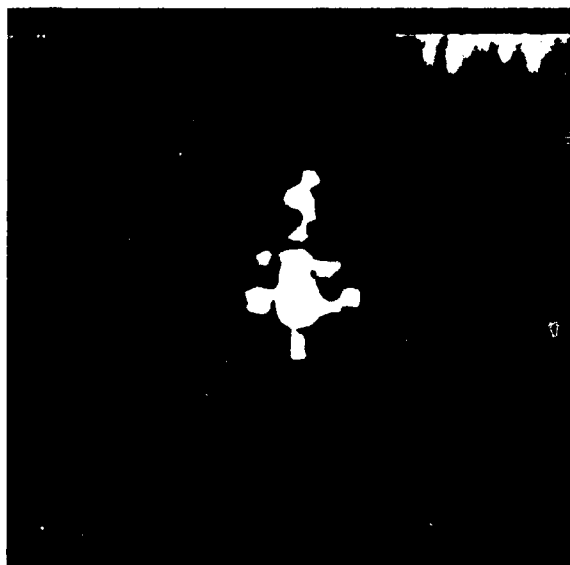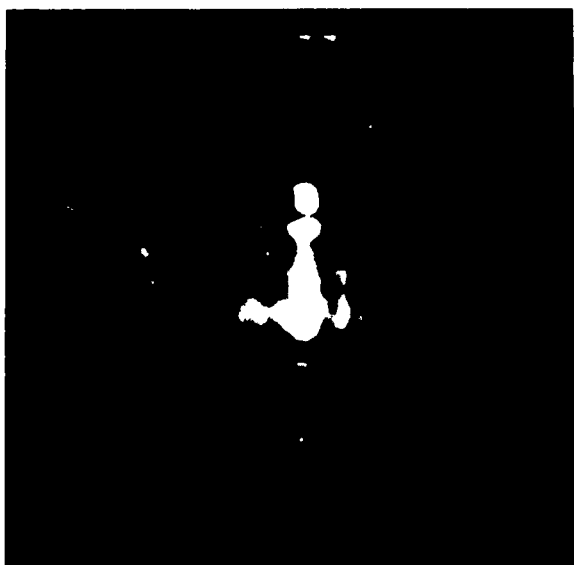
a. Tail Aspects
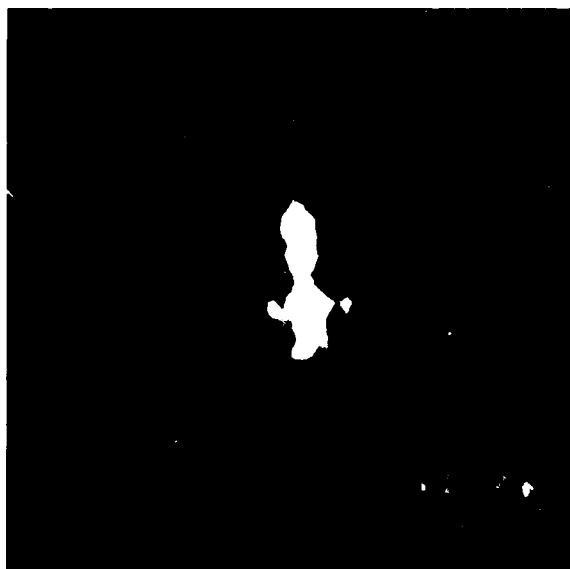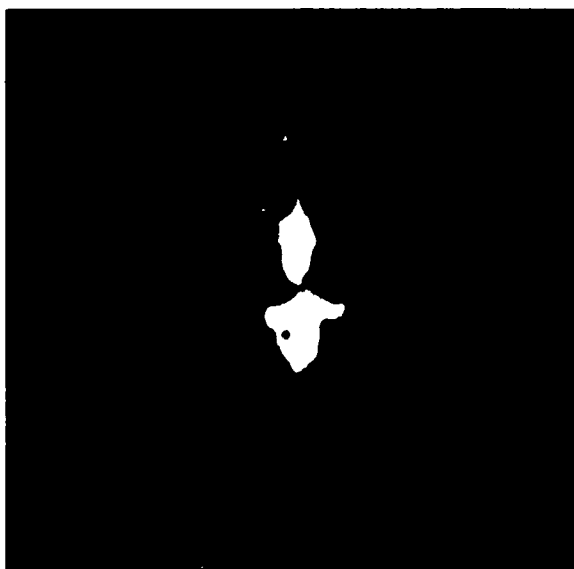
b. Nose Aspect

Figure 23. Top view of F-102 with 1.17m range resolution and 0.95m cross range resolution
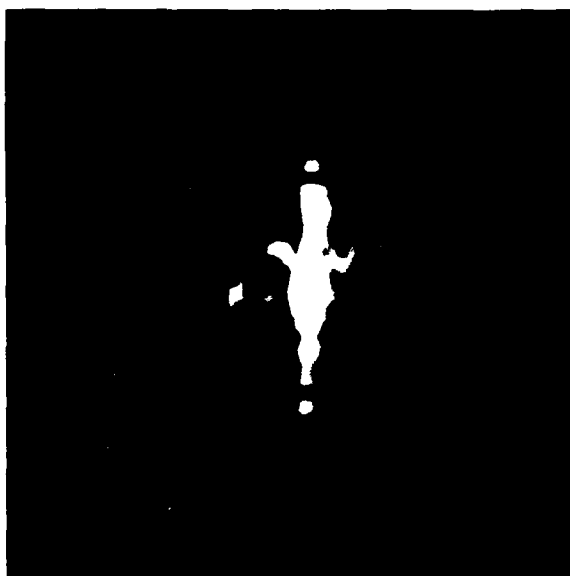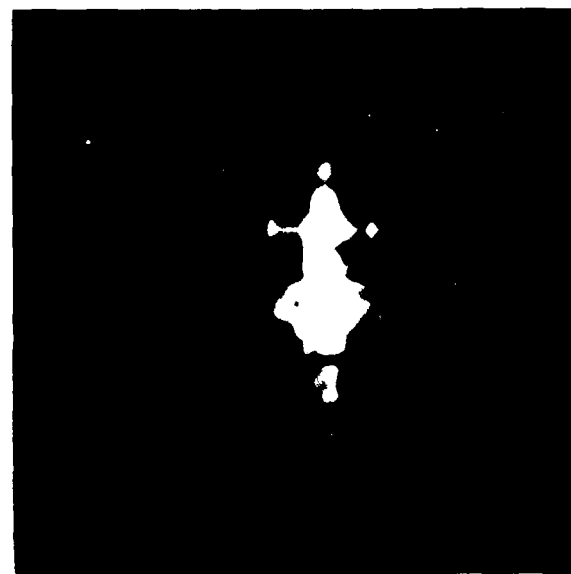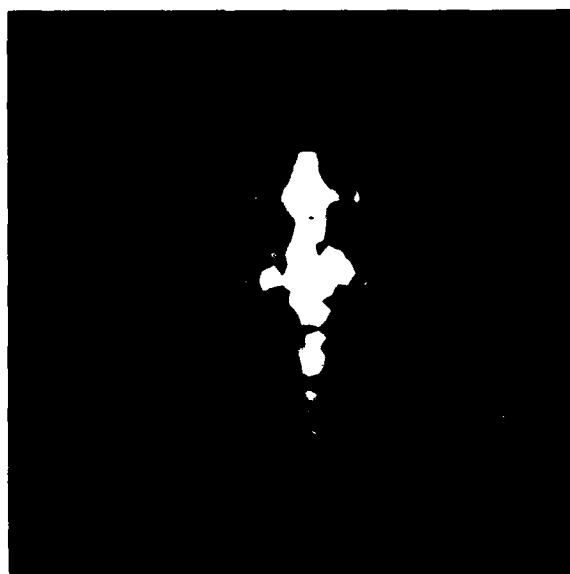
a. Tail Aspects

b. Nose Aspect

Figure 29. Top view of F-5E with 1.17m range resolution and 0.95m cross range resolution

81
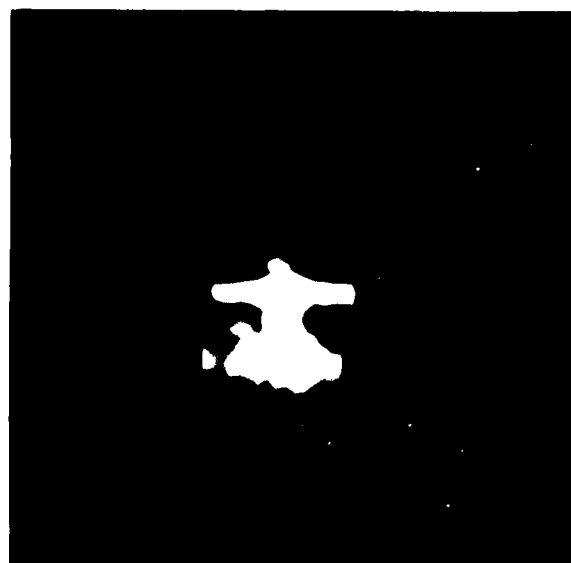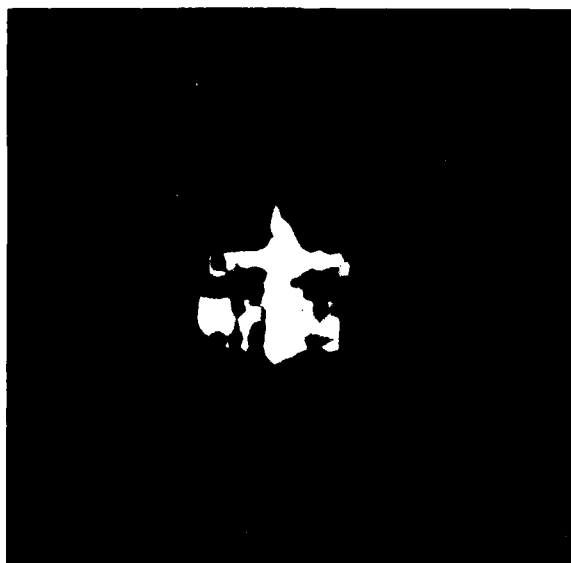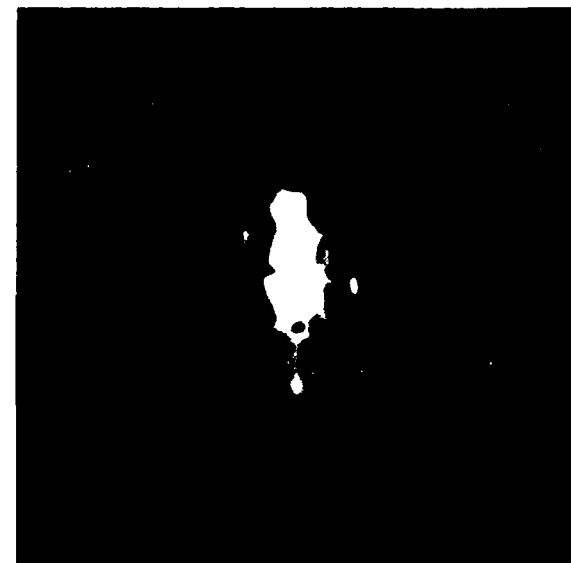
a. Tail Aspects

b. Nose Aspects

Figure 26. Top view of F-15 with 1.17m range resolution and 0.95m cross range resolution
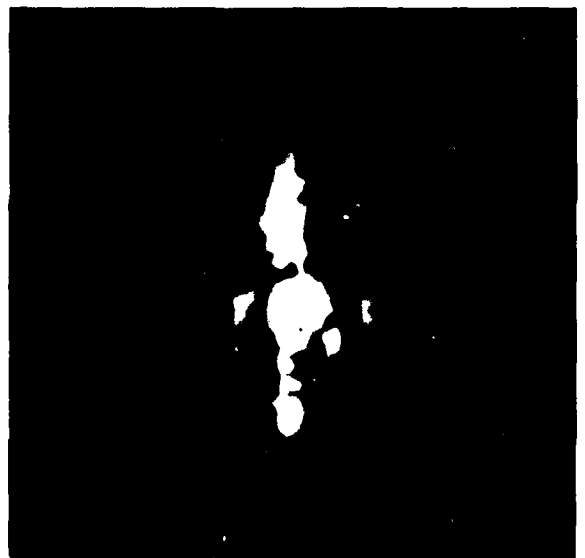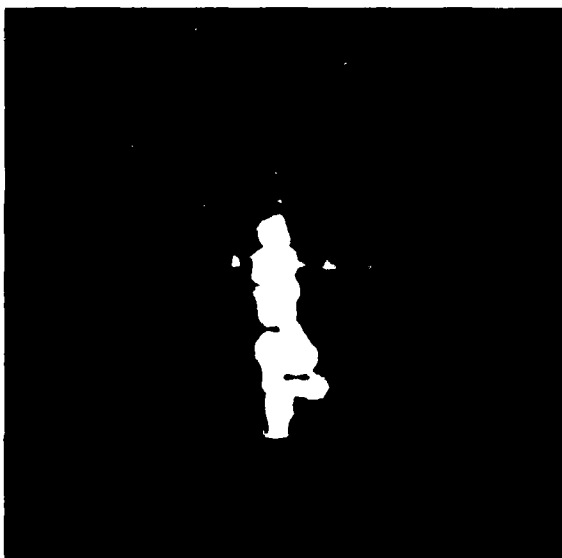
a. Tail Aspect

b. Nose Aspect

Figure 77. Top view of YF-16 with 1.17m range resolution and 0.46m cross range resolution
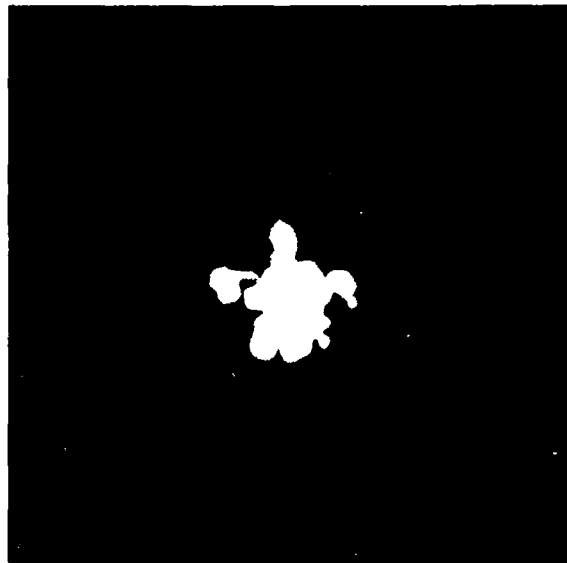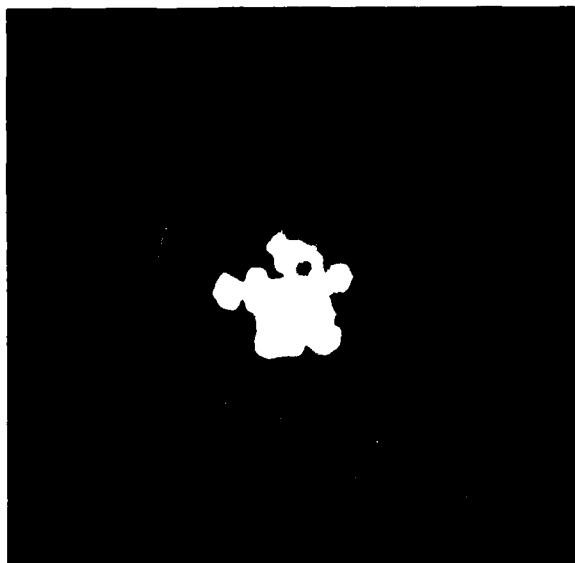
a. Tail Aspects
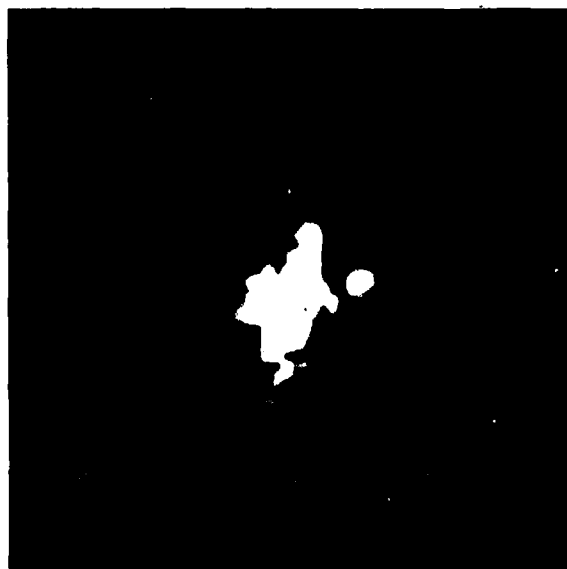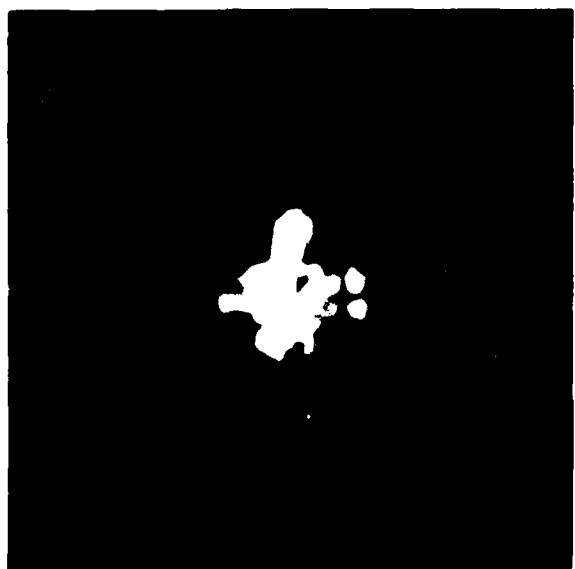
b. Nose Aspects

Figure. Zero range and 0.96m cross range resolution

0 - 3 degrees, 5 - 8 degrees,

85 - 87 degrees and 2 - 5 degrees,

7 - 10 degrees, ...87 - 90 degrees.

Examples of images from this target are shown in Figure 29. All of the above images correspond to top views of the targets i.e. projections on the horizontal plane. From the NOSC data set a small number of images (10 top views and 10 side views) was obtained for a DC-10, and examples are shown in Figure 13. Because this target was moving, it was necessary to use the full 256 MHz measurement bandwidth to properly focus and align the range signatures used in forming the image. For classification tests only the ten side views obtained on this target have been used. These images were combined with a set of ten side view images obtained using RATSCAT measurements for the F-5E and the A-10. The side views on these targets, examples of which are shown in Figures 9 and 10, were obtained for a 6.2 degree rotation of the target for nose aspects (-18.2 to -12.0 degrees, -15.2 to -9 degrees, -12.2 to -6 degrees, -912 to -3 degrees, -6.2 to 0 degrees, 0 to 6.2 degrees, 3.2 to 9.7 degrees, 6.0 to 12.2 degrees, 9.0 to 15.2 degrees, 12.9 to 18.2 degrees) using the full 256 MHz measurement bandwidth resulting in 0.6 meter range resolution and 0.5 meter cross range resolution on the full scale target.

In addition to the above classification tests the classifiers were also presented with top view images of the RATSCAT targets obtained using the full 256 MHz bandwidth and a 6.2 degree rotation of the target. For these tests 24 images per target for the five RATSCAT targets were formed over the following set of aspects (0.8 - 7 degrees, 6.8 -13 degrees, . . . 30.8 - 37 degrees, 140.8 - 147 degrees, 146.8 - 153 degrees, ... 170.8 -177 degrees) and 3.8 - 10 degrees, 9.8 - 16 degrees, ... 33.8 - 40 degrees, 143.8 - 150 degrees, 149.8 - 156 degrees, ...173.8 - 180 degrees) and the classifier was trained on the first set and classified the second. Examples of these images are shown in Section II.
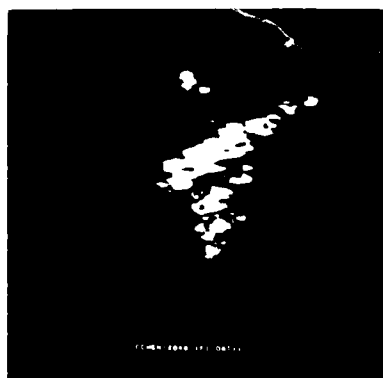
a. First 20 seconds or 2048 signatures
   ($\approx 2.5°$ aspect change)
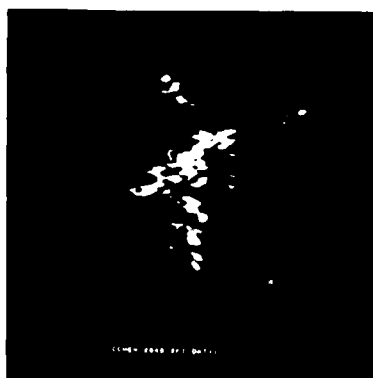
b. Second 20 seconds

c. Third 20 seconds

d. Fourth 20 seconds

Figure 29. Images of an F-111 generated using data obtained by ALCOR Radar

6.1 CLASSIFICATION PERFORMANCE OF FEATURE VECTORS USING THE CENTRAL MOMENTS

In this section performance results are presented for feature vectors computed using moments from the image, a combination of moments from the image and edge detected image and moments from the edge detected image. For the classification tests the Kth nearest neighbor classifier and the Gaussian classifier have been used.

To avoid the problem of singular covariance matrices resulting from training sets with a small number of learning vectors as compared to their dimensionality. whenever the training set was small in comparison to the number of features the kth nearest neighbor classifier was used.

For the classification tests in this study the measurements on the targets ranging from 0 degrees (for nose aspects) to 180 degrees (for tail aspects) on the plan view images were subdivided into either four 45 degree sectors (0 - 45 degrees. 45 - 90 degrees. 90) - 135 degrees. 135 - 180 degrees) or three 60 degree sectors (0 - 60 degrees. 60 - 120 degrees. 120 - 180 degrees). In each case the classifiers were trained and tested on a per sector basis.

For classification using the central moments from the image and from the edge detected image all moments of orders 2 to 7 were computed giving a total number of 33 central moments. For the classification tests using the Kth nearest neighbor for the plan view images with 1. 17 meter range and 0.95 meter cross range resolution the classifier was trained using 36 images per target obtained using the lower 128 frequency steps over the aspects 0 - 5 degrees. 5 - 8 degrees. ... 175 - 175 degrees. The classifier was tested using 72 images per target. where 36 images were obtained from the same set of 128 frequency steps for data collected from aspects 2 - 5 degrees. 7 - 10 degrees. ... 177 - 180 degrees. The remaining 36 images were obtained from the next 128 frequency steps out of a total of 256 steps for aspects 0 - 5 degrees. 5 - 8 degrees. ... 175 - 175 degrees. The 33 central moments were ordered according to their importance for classification purposes using the Mahalanobis distance criterion for each and every target. The resulting ordering of the most 12 moments averaged together over all aspects for nose and tail. list. N1 represents the

the F-111 was: μ_{20}, μ_{02}, μ_{40}, μ_{22}, μ_{30}, μ_{31}, μ_{60}, μ_{70}, μ_{12}, μ_{41}, μ_{51}, μ_{24}, where the first index corresponds to range and the second to cross range. The corresponding ranking of the best 12 central moments from the edge detected image is μ_{20}, μ_{02}, μ_{40}, μ_{22}, μ_{60}, μ_{31}, μ_{30}, μ_{50}, μ_{24}, μ_{04}, μ_{06}, μ_{42}. Figures 30 and 31 show the classification performance obtained using all 33 moments from the image. Figures 32 and 33 show the classification performance obtained when the best 12 moments from the image and the best 12 moments from the edge detected image are combined to form a 24 element feature vector. These figures show the performance is of the order of 50 to 65 percent. However, when the elements of the feature vector obtained using the 24 moments (best 12 from image and best 12 from edge detected image) are normalized by their standard deviation over all targets and aspects the kth nearest neighbor classification results are of the order of 80 to 97 percent as seen in Figures 34 and 3?. Figures 35 through 38 show a detailed tabulation of the classification results
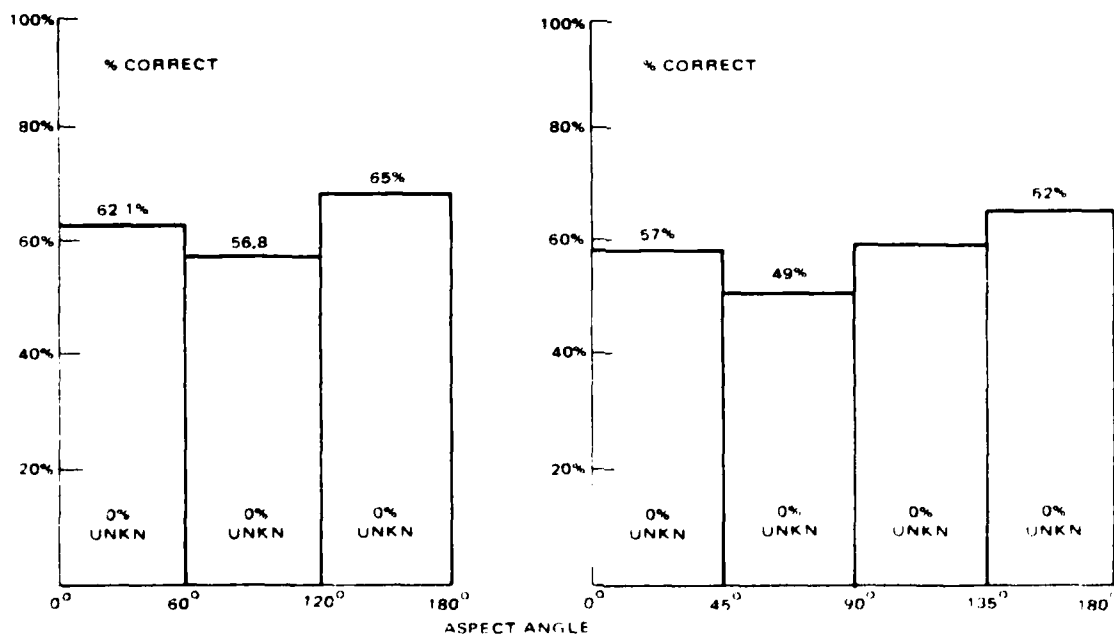
Figure 30. Classification results for 33 moments from image intensity (1m resolution plan views 6 classes) using kth nearest neighbor (no unknown class for 45° and 60° sectors)
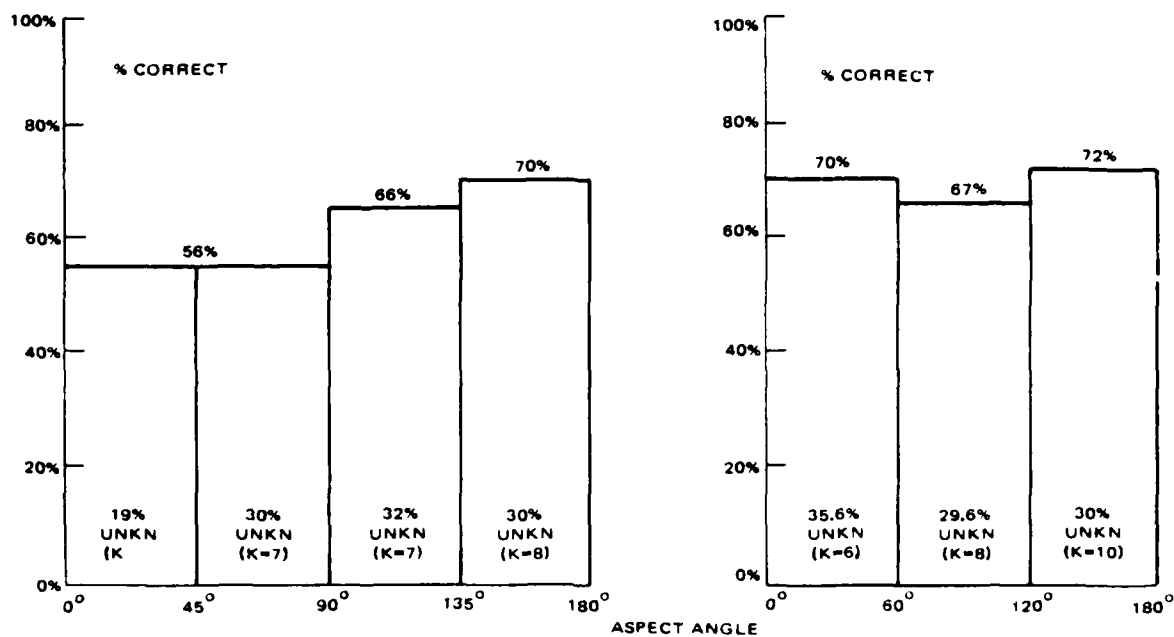
Figure 31. Classification results for 33 moments from image intensity (1m resolution plan views 6 classes) using kth nearest neighbor (with unknown), for 45° and 60° sectors.
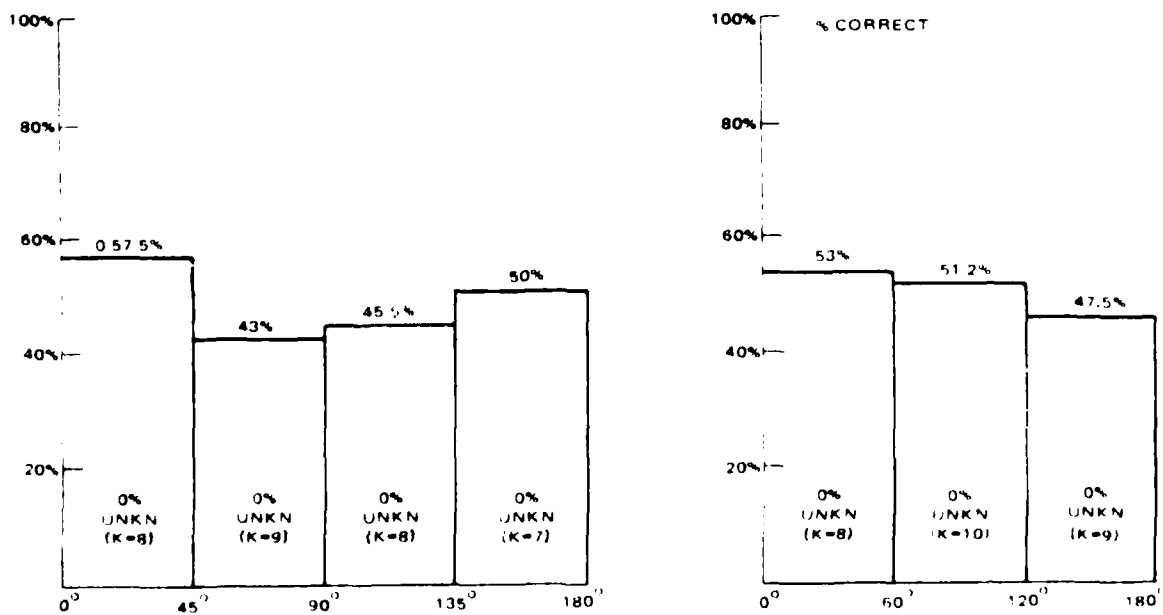
Figure 32 K-th nearest neighbor classification results (1m resolution plan views 6 classes) for 24 moments (12 best from image and 12 best from edge detected image) (no unknown), for 45° and 60° sectors.
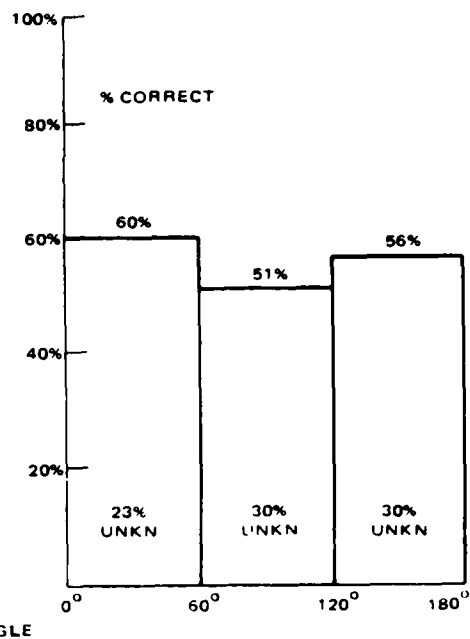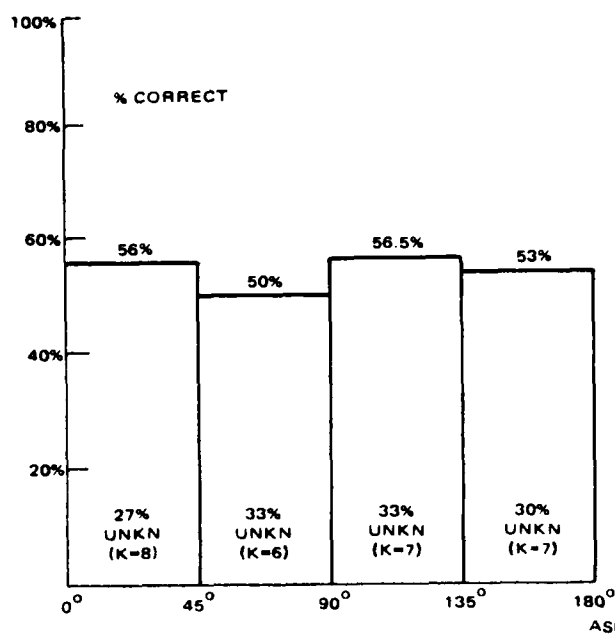
Figure 33. K-th nearest neighbor classification results (1m resolution plan views 6 classes) for 24 moments (12 best from image and 12 best from edge detected image) (with unknown) for 45° and 60° sectors.
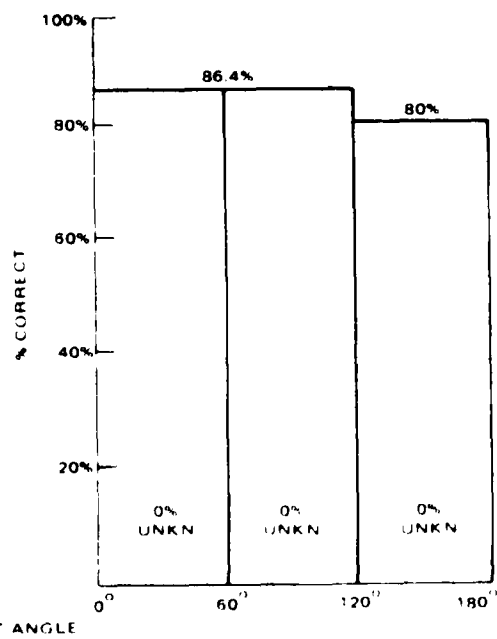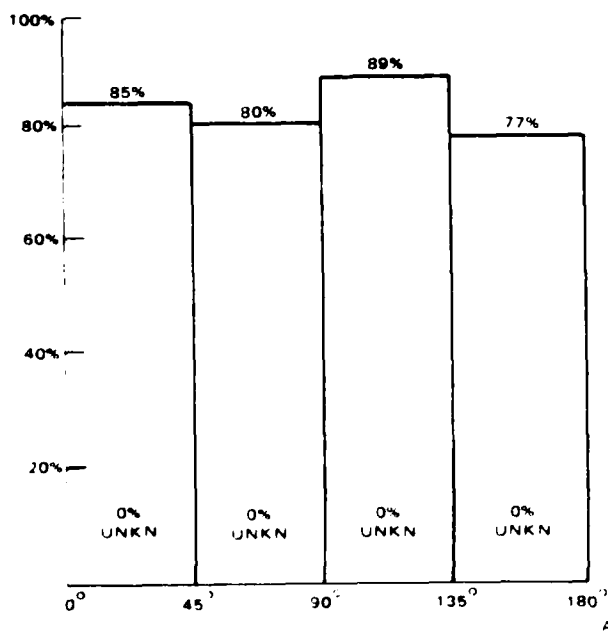
Figure 34 K-th nearest neighbor classification results (1m resolution plan views 6 classes) for 24 moments (12 best from image and 12 best from edge detected image) normalized by their standard deviations for K = 6 and no 'unknown' class.

CLASSIFIER DECISION

TARGET PRESENTED	F-102	F-15	F-16	F-5E	A-10	F-111	UNKN
F-102	17		1				0
F-15		15	3				0
F-16		3	15				0
F-5E	2		6	10			0
A-10					18		0
F-111						9	0

% CORRECT DECISION: 85%

Figure 35. Kth nearest neighbor classification results (1m resolution plan view images) for K = 6 for 24 moments (best 12 from image and best 12 from edge detected image) normalized by their standard deviations for 0° to 45° aspect angles (0° is nose-on). Threshold for unknown = 0.0.

CLASSIFIER DECISION

TARGET PRESENTED	F-102	F-15	F-16	F-5E	A-10	F-111	UNKN
F-102	17				1		0
F-15		15	2				0
F-16		5	11	2			0
F-5E		1	1	15	1		0
A-10	3				15		0
F-111	2		1	1		5	0

% CORRECT DECISION: 80%

Figure 36. Kth nearest neighbor classification results (1m resolution plan view images) for K = 6 for 24 moments (best 12 from image and best 12 from edge detected image) normalized by their standard deviations for 45° to 90° aspects. Threshold for unknown = 0.0.

CLASSIFIER DECISION

TARGET PRESENTED	F-102	F-15	F-16	F-5E	A-10	F-111	UNKN
F-102	15			1	2		0
F-15		16	2				0
F-16			18				0
F-5E				15	3		0
A-10	2				16		0
F-111							

% CORRECT DECISION 89%

Figure 37. Kth nearest neighbor classification results (1m resolution plan views) for K = 6 for 24 moments (best 12 from image and best 12 from edge detected image) normalized by their standard deviations for 90° to 135° aspects. Threshold for unknown = 0.0

CLASSIFIER DECISION

TARGET PRESENTED	F-102	F-15	F-16	F-5E	A-10	F-111	UNKN
F-102	14		2	2			0
F-15		14	4				0
F-16	1	4	11	2			0
F-5E	2	2	2	12			0
A-10					18		0
F-111							

% CORRECT DECISION 77%

Figure 38. Kth nearest neighbor classification results (1m resolution plan views) for K = 6 for 24 moments (best 12 from image and best 12 from edge detected image) normalized by their standard deviations for 135° to 180° aspects. Threshold for unknown = 0.0

- 1
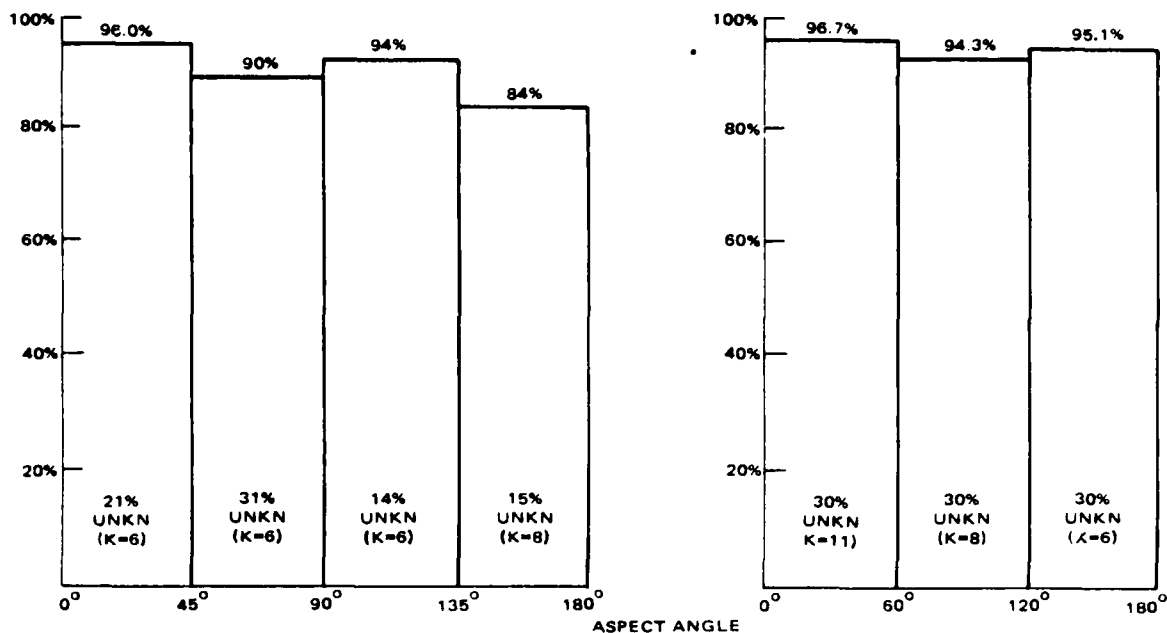
Figure 39. Kth nearest neighbor classification results (1m resolution plan views 6 classes) for 24 moments (12 best from image and 12 best from edge detected image) normalized by their standard deviations with provision for unknown.

for the 24 element feature vector when four 45 degree sectors are used. Figures 40 to 43 show the improved classification performance for the same feature vector when the classifier is allowed to make a decision of "unknown". The classification performance of the same 24-element feature vector when applied to the 1/2 meter resolution plan view images is shown in Figures 44 through 46. Figures 44 and 45 show results for nose aspects while Figure 46 shows the results for tail aspects. A comparison of Figure 44 to Figure 36, which shows results for the 1-meter resolution data, shows a 5 percent improvement in classification for nose aspects while from Figures 46 and 38 about 10 percent improvement is shown for tail aspects. However, in view of the limited numbers of images with 0.5 meter resolution used for these tests the results of this comparison with the 1.0 meter resolution data is not very conclusive, but it does show that classification improves with resolution for the aircraft targets considered here. Classification results with the Gaussian classifier using four degree sectors for the best 12 moments that is the best tail moments selected from the image and use for the best six in the image combined with the best six from the edge detected image

CLASSIFIER DECISION

TARGET PRESENTED	F-102	F-15	F-16	F-5E	A-10	F-111	UNKN
F-102	14						4
F-15		14	1				3
F-16		1	13				4
F-5E			1	10			7
A-10					17		1
F-111						7	2

PLAN VIEWS NOSE ASPECTS ONE METER RESOLUTION

% CORRECT DECISION: 96%

% UNKNOWN: 21%

Figure 40. Kth nearest neighbor classification results (1m resolution plan views) for K = 6 for 24 moments (best 12 from image and best 12 from edge detected image) normalized by their standard deviations for 0° to 45° aspects. Threshold for unknown = 0.5.

CLASSIFIER DECISION

TARGET PRESENTED	F-102	F-15	F-16	F-5E	A-10	F-111	UNKN
F-102	13						5
F-15		14	2				1
F-16		4	7				7
F-5E			1	10			7
A-10					13		5
F-111						4	5

% CORRECT DECISION: 90%

% UNKNOWN: 31%

Figure 41. Kth nearest neighbor classification results (1m resolution plan views) for K = 6 for 24 moments (best 12 from image and best 12 from edge detected image) normalized by their standard deviations for 45° to 90° aspects. Threshold for unknown = 0.5.

CLASSIFIER DECISION

TARGET PRESENTED	F-102	F-15	F-16	F-5E	A-10	F-111	UNKN
F-102	13				2		3
F-15		16					2
F-16			16				2
F-5E				11	2		5
A-10	1				16		1
F-111							

% CORRECT DECISION 94%

% UNKNOWN 14%

Figure 42. Kth nearest neighbor classification results (1m resolution plan views) for K = 6 for 24 moments (best 12 from image and best 12 from edge detected image) normalized by their standard deviations for 90° to 135° aspects. Threshold = 0.5.

CLASSIFIER DECISION

TARGET PRESENTED	F-102	F-15	F-16	F-5E	A-10	F-111	UNKN
F-102	13						5
F-15		14	2				2
F-16	1	4	10	1			2
F-5E	1	1	2	10			4
A-10					17		1
F-111							

PLAN VIEWS TAIL ASPECTS 1 METER RESOLUTION

% CORRECT DECISION 84%

% UNKNOWN 15%

Figure 43. Kth nearest neighbor classification results (1m resolution plan views) for K = 8 for 24 moments (best 12 from image and best 12 from edge detected image for 135° to 180° aspects. Threshold for unknown = 0.5.

CLASSIFIER DECISION

TARGET PRESENTED	F-102	F-15	F-16	F-5E	A-10	F-111	UNKN
F-102	6						
F-15		5	1				
F-16			6				
F-5E	2			4			
A-10					6		
F-111							

PLAN VIEWS NOSE ASPECTS 0.5 METER RESOLUTION

% CORRECT DECISION: 90%

Figure 44. Kth nearest neighbor classification results (0.5 meter resolution plan views) for K = 5 for 24 moments (best 12 from image and best 12 from edge detected image) normalized by their standard deviations for 0° to 40° aspects. Threshold = 0.0.

CLASSIFIER DECISION

TARGET PRESENTED	F-102	F-15	F-16	F-5E	A-10	F-111	UNKN
F-102	5						1
F-15		5	1				
F-16			6				
F-5E				4			2
A-10					6		
F-111							

PLAN VIEWS NOSE ASPECTS 0.5 METER RESOLUTION

% CORRECT DECISION: 96%
% UNKNOWN = 10%

Figure 45. Kth nearest neighbor classifications results (0.5 meter resolution plan views) for K = 7 for 24 moments (best 12 from image and best 12 from edge detected image) normalized by their standard deviations for 0° to 40° aspects. Threshold = 0.5.

CLASSIFIER DECISION

TARGET PRESENTED	F-102	F-15	F-16	F-5E	A-10	F-111	UNKN
F-102	5	1					
F-15		6					
F-16		1	5				
F-5E				6			
A-10					6		
F-111							

PLAN VIEWS TAIL ASPECTS 0.5 METER RESOLUTION
% CORRECT DECISION 93%

Figure 46. Kth nearest neighbor classification results for K = 5 for 24 moments (best 12 from image and best 12 from edge detected image) normalized by their standard deviations for 140° to 180° aspects.

are shown in Tables 3 and 4. Tables 5 and 6 show classification results with the Gaussian classifier using three 60 degree sectors for the best 18 moments from the image and for the best nine moments from the image combined with the best nine from the edge detected image. Tables 7 and 8 show cladsification results using the best 12 moments from the edge detected image using the Gaussian classifier with 45 degree sectors. In general, the best overall performance was obtained using the best 12 moments from the image although for nose aspects the 12-dimensional feature vector using the moments from the edge detected image and the feature vector using six moments from the image and six from the edge detected image did better.

Using 10 profile views of the DC-10, F-5E and A-10 and the best 18 normalized moments from the image, classification tests were performed with the kth nearest neighbor rule for $k = 4$. The classifier was trained using five images per target and was tested with the remaining five per target. A perfect score was obtained in this test, and the results are shown in Figure 47.

CLASSIFIER DECISION

	DC-10	F-5E	A-10	UNKN
DC-10	5			
F-5E		5		
A-10			5	

TARGET PRESENTED

Figure 47. Kth nearest neighbor classifier using 18 normalized moments. Profile images with 0.5 meter resolution (nose aspects), (K = 4).

TABLE 3. CLASSIFICATION RESULTS FOR 45° SECTORS (SECTOR 1 IS NOSE ASPECTS AND SECTOR 4 IS TAIL ASPECTS) USING THE BEST 12 OUT OF 33 MOMENTS COMPUTED FROM THE IMAGE INTENSITIES USING THE GAUSSIAN CLASSIFIER WITH β = 100 PERCENT AND q = 0.0

FOR SECTOR #1

TARGET: **IDENTIFIED AS**

	F-102	F-15	F-16	F-5E	A-10	F-111	UK
F-102	9	0	0	0	0	0	0
F-15	1	5	1	2	0	0	0
F-16	0	0	4	4	0	1	0
F-5E	0	0	0	9	0	0	0
A-10	0	0	0	0	8	1	0
F-111	0	0	0	0	0	9	0

PROBABILITY FOR A CORRECT DECISION 81%

FOR SECTOR #2

TARGET: **IDENTIFIED AS**

	F-102	F-15	F-16	F-5E	A-10	F-111	UK
F-102	6	8	0	0	8	0	0
F-15	0	5	1	2	0	1	0
F-16	0	0	5	3	0	1	0
F-5E	0	0	1	6	1	0	0
A-10	0	0	0	0	9	0	0
F-111	0	0	0	0	0	9	0

PROBABILITY FOR A CORRECT DECISION 75%

FOR SECTOR #3

TARGET: **IDENTIFIED AS**

	F-102	F-15	F-16	F-5E	A-10	F-111	UK
F-102	9	0	0	0	0	0	0
F-15	0	9	0	0	0	0	0
F-16	0	9	0	0	0	0	0
F-5E	2	0	7	0	0	0	0
A-10	1	0	0	6	2	0	0
F-111	0	0	0	0	0	0	0

PROBABILITY FOR A CORRECT DECISION 86%

FOR SECTOR #4

TARGET: **IDENTIFIED AS**

	F-102	F-15	F-16	F-5E	A-10	F-111	UK
F-102	9	0	0	0	0	0	0
F-15	1	5	0	2	1	0	0
F-16	3	0	5	0	1	0	0
F-5E	0	0	0	9	0	0	0
A-10	0	0	0	0	9	0	0
F-111	0	0	0	0	0	9	0

PROBABILITY FOR A CORRECT DECISION 92%

TABLE 4. CLASSIFICATION RESULTS FOR 45° SECTORS USING 12 MOMENTS (BEST 6 FROM IMAGE AND BEST 6 FROM EDGE DETECTED IMAGE) USING THE GAUSSIAN CLASSIFIER WITH β = 99 PERCENT AND q = 0.0

```
FOR  SECTOR  #1

  TARGET:              **IDENTIFIED AS**
           F-102   F-15   F-16   F-5E   A-10   F-111    UK
  F-102      8      0      0      0      0      0       1
  F-15       0      7      2      0      0      0       0
  F-16       3      0      6      0      0      0       0
  F-5E       1      0      0      8      0      0       0
  A-10       0      0      0      0      9      0       0
  F-111      0      0      0      0      0      9       0
PROBABILITY FOR A CORRECT DECISION  88%
PERCENT UNKNOWN   2%
FOR  SECTOR  #2

  TARGET:              **IDENTIFIED AS**
           F-102   F-15   F-16   F-5E   A-10   F-111    UK
  F-102      9      0      0      0      0      0       0
  F-15       0      4      4      1      0      0       0
  F-16       2      0      3      1      3      0       0
  F-5E       3      0      0      6      0      0       0
  A-10       1      0      0      0      7      0       1
  F-111      0      0      0      0      0      9       0
PROBABILITY FOR A CORRECT DECISION  71%
PERCENT UNKNOWN   2%
FOR  SECTOR  #3

  TARGET:              **IDENTIFIED AS**
           F-102   F-15   F-16   F-5E   A-10   F-111    UK
  F-102      9      0      0      0      0      0       0
  F-15       0      9      0      0      0      0       0
  F-16       2      0      5      2      0      0       0
  F-5E       1      0      0      8      0      0       0
  A-10       2      0      0      0      7      0       0
  F-111      0      0      0      0      0      0       0
PROBABILITY FOR A CORRECT DECISION  84%
PERCENT UNKNOWN   0%
FOR  SECTOR  #4

  TARGET:              **IDENTIFIED AS**
           F-102   F-15   F-16   F-5E   A-10   F-111    UK
  F-102      9      0      0      0      0      0       0
  F-15       3      4      2      0      0      0       0
  F-16       2      0      6      1      0      0       0
  F-5E       3      0      0      6      0      0       0
  A-10       1      0      0      0      8      0       0
  F-111      0      0      0      0      0      0       0
PROBABILITY FOR A CORRECT DECISION  75%
PERCENT UNKNOWN   2%
```

87

TABLE 5. CLASSIFICATION RESULTS FOR 60° SECTORS FOR THE BEST
18 MOMENTS OUT OF 33 (COMPUTED FROM THE IMAGE INTENSITY)
USING THE GAUSSIAN CLASSIFIER WITH $\beta = 99.5$ PERCENT AND $q = 0.5$

FOR SECTOR #1

TARGET: **IDENTIFIED AS**

	F-102	F-15	F-16	F-5E	A-10	F-111	UK
F-102	12	0	0	0	0	0	0
F-15	1	6	0	2	0	2	1
F-16	2	0	6	2	0	1	1
F-5E	1	0	0	10	0	0	1
A-10	0	0	0	0	12	0	0
F-111	0	0	0	0	0	12	0

PROBABILITY FOR A CORRECT DECISION 84%
PERCENT UNKNOWN 4%

FOR SECTOR #2

TARGET: **IDENTIFIED AS**

	F-102	F-15	F-16	F-5E	A-10	F-111	UK
F-102	10	0	0	0	2	0	0
F-15	0	10	1	0	1	0	0
F-16	1	0	4	0	6	0	1
F-5E	0	0	0	5	6	0	1
A-10	0	0	0	0	10	0	2
F-111	0	0	0	0	0	0	0

PROBABILITY FOR A CORRECT DECISION 69%
PERCENT UNKNOWN 7%

FOR SECTOR #3

TARGET: **IDENTIFIED AS**

	F-102	F-15	F-16	F-5E	A-10	F-111	UK
F-102	8	0	0	1	0	0	2
F-15	0	8	0	4	0	0	0
F-16	1	0	9	2	0	0	0
F-5E	0	0	0	10	1	0	1
A-10	0	0	0	0	12	0	0
F-111	0	0	0	0	0	0	0

PROBABILITY FOR A CORRECT DECISION 83%
PERCENT UNKNOWN 5%

88

TABLE 6. CLASSIFICATION RESULTS FOR 60° SECTORS FOR THE BEST 18 MOMENTS (9 FROM IMAGE AND 9 FROM EDGE DETECTED IMAGE) USING THE GAUSSIAN CLASSIFIER WITH β = 100 PERCENT AND q = 0.0 (NO UNKNOWN)

FOR SECTOR #1

TARGET: **IDENTIFIED AS**

	F-102	F-15	F-16	F-5E	A-10	F-111	UK
F-102	12	0	0	0	0	0	0
F-15	0	8	1	0	0	3	0
F-16	2	0	6	0	0	4	0
F-5E	3	0	0	9	0	0	0
A-10	1	0	0	0	11	0	0
F-111	0	0	0	0	0	12	0

PROBABILITY FOR A CORRECT DECISION 80%
PERCENT UNKNOWN 0%

FOR SECTOR #2

TARGET: **IDENTIFIED AS**

	F-102	F-15	F-16	F-5E	A-10	F-111	UK
F-102	11	0	0	0	1	0	0
F-15	0	8	0	0	4	0	0
F-16	4	2	2	1	3	0	0
F-5E	4	0	1	4	3	0	0
A-10	2	0	0	0	10	0	0
F-111	0	0	0	0	0	0	0

PROBABILITY FOR A CORRECT DECISION 58%
PERCENT UNKNOWN 0%

FOR SECTOR #3

TARGET: **IDENTIFIED AS**

	F-102	F-15	F-16	F-5E	A-10	F-111	UK
F-102	10	0	0	1	0	0	0
F-15	2	2	7	1	0	0	0
F-16	1	0	10	1	0	0	0
F-5E	4	0	0	8	0	0	0
A-10	2	0	0	0	10	0	0
F-111	0	0	0	0	0	0	0

PROBABILITY FOR A CORRECT DECISION 67%
PERCENT UNKNOWN 0%

TABLE 7. CLASSIFICATION RESULTS FOR 45° SECTORS USING THE BEST 12 OUT OF 33 MOMENTS COMPUTED FROM THE EDGE DETECTED IMAGE USING THE GAUSSIAN CLASSIFIER WITH β = 100 PERCENT AND q = 0.0

FOR SECTOR #1

TARGET:	**IDENTIFIED AS**						
	F-102	F-15	F-16	F-5E	A-10	F-111	UK
F-102	9	0	0	0	0	0	0
F-15	0	8	1	0	0	0	0
F-16	0	0	5	3	1	0	0
F-5E	0	0	0	9	0	0	0
A-10	0	0	0	0	9	0	0
F-111	0	0	0	0	0	9	0

PROBABILITY FOR A CORRECT DECISION 90%
PERCENT UNKNOWN 0%

FOR SECTOR #2

TARGET:	**IDENTIFIED AS**						
	F-102	F-15	F-16	F-5E	A-10	F-111	UK
F-102	7	0	0	1	0	1	
F-15	0	5	1	2	0	1	
F-16	0	1	4	2	2	0	0
F-5E	1	0	0	3	0	0	0
A-10		0	0	0			0
F-111		0	0	0	0	9	0

PROBABILITY FOR A CORRECT DECISION 75%
PERCENT UNKNOWN 0%

FOR SECTOR #3

TARGET:	**IDENTIFIED AS**						
	F-102	F-15	F-16	F-5E	A-10	F-111	UK
F-102	7	0	0	0	0		
F-15	0	7	0	2	0	0	
					0		
				5		0	
		0				1	0
F-111		0		0	0		0

PROBABILITY FOR A CORRECT DECISION 73%
PERCENT UNKNOWN 0%

FOR SECTOR #4

TARGET:	**IDENTIFIED AS**						
	F-102	F-15	F-16	F-5E	A-10	F-111	
					0	0	
					0		
		0					

PROBABILITY FOR A CORRECT DECISION 63%
PERCENT UNKNOWN 0%

TABLE 8. CLASSIFICATION RESULTS FOR 45° SECTORS USING THE BEST 12 OUT OF 33 MOMENTS COMPUTED FROM THE EDGE DETECTED IMAGE USING THE GAUSSIAN CLASSIFIER WITH β = 99 PERCENT AND q = 0.0

FOR SECTOR #1

TARGET: **IDENTIFIED AS**

	F-102	F-15	F-16	F-5E	A-10	F-111	UK
F-102	9	0	0	0	0	0	0
F-15	0	8	1	0	0	0	0
F-16	1	0	5	3	1	0	0
F-5E	0	0	0	8	0	0	1
A-10	0	0	0	0	9	0	0
F-111	0	0	0	0	0	9	0

PROBABILITY FOR A CORRECT DECISION 90%
PERCENT UNKNOWN 2%

FOR SECTOR #2

TARGET: **IDENTIFIED AS**

	F-102	F-15	F-16	F-5E	A-10	F-111	UK
F-102			1	0		0	
F-15	3	5	1	2		1	0
F-16		1	4	2	2	0	
F-5E			0	8	0	0	0
A-10			0	0			
F-111		0		0	0		

PROBABILITY FOR A CORRECT DECISION 76%
PERCENT UNKNOWN 4%

FOR SECTOR #3

TARGET: **IDENTIFIED AS**

	F-102	F-15	F-16	F-5E	A-10	F-111	UK

PROBABILITY FOR A CORRECT DECISION

PERCENT UNKNOWN

FOR SECTOR #4

91

6.2 CLASSIFICATION RESULTS USING INVARIANT MOMENT FUNCTIONS

As described in Section III some algebraic relations among the central moments of an image are invariant with respect to rotations of the image in the image plane. These relations are known as orthogonal invariant moment functions and have been proven to be a usefull feature for shape recognition in photographs and FLIR images. As described in Section III and Appendix A, 33 orthogonal moment invariants were computed using all central moments of orders 2 to 7. Orthogonal moment invariants were computed using both the image and the edge detected image. The invariant moment functions were ranked in terms of their importance as classification features using the Mahalanobis distance criterion described in Section 5. The resulting ordering was the same for both the invariants from the image and the invariants from the edge detected image. This ordering is:

$\rho_{21}, \rho_{29}, \rho_1, \rho_2, \rho_3, \rho_4, \rho_5, \rho_6, \rho_7, \rho_8, \rho_9, \rho_{10}, \rho_{18}, \rho_{17}, \rho_{22}, \rho_{28}, \rho_{23}, \rho_{20},$ where the invariants ρ_i are defined in Appendix A.

Using a 24-element feature vector obtained by combining the best 12 invariants from the image and the best 12 invariants from the edge detected image classification tests were performed against the 1 meter resolution plan view images of the five RATSCAT aircraft models and the F-111. For these tests the kth nearest neighbor classifier was used. The results are summarized in Figure 48. The training set for the RATSCAT targets consisted of 36 images per target formed by using the first set of 128 frequency steps over the following set of aspects 0 to 3 degrees, 5 to 8 degrees, ... 175 to 178 degrees. The testing set consisted of 72 images per target, where 36 were obtained from the same set of 128 frequency steps for data collected from aspects 2 to 5 degrees, 7 to 10 degrees, ... 177 to 180 degrees); 36 additional images were obtained from the next 128 frequency steps (out of the total 256 steps used for data collection) for aspects (0 to 3 degrees, 5 to 8 degrees, ...175 to 178 degrees). The training set for the F-111 images obtained using the ALCOR radar data consisted of images formed over the following set of aspects (0 to 3 degrees, 5 to 8 degrees, ...85 to 87 degrees). The testing set for this target consisted of images formed over the set of aspects (2 to 5 degrees, 7 to 10 degrees,
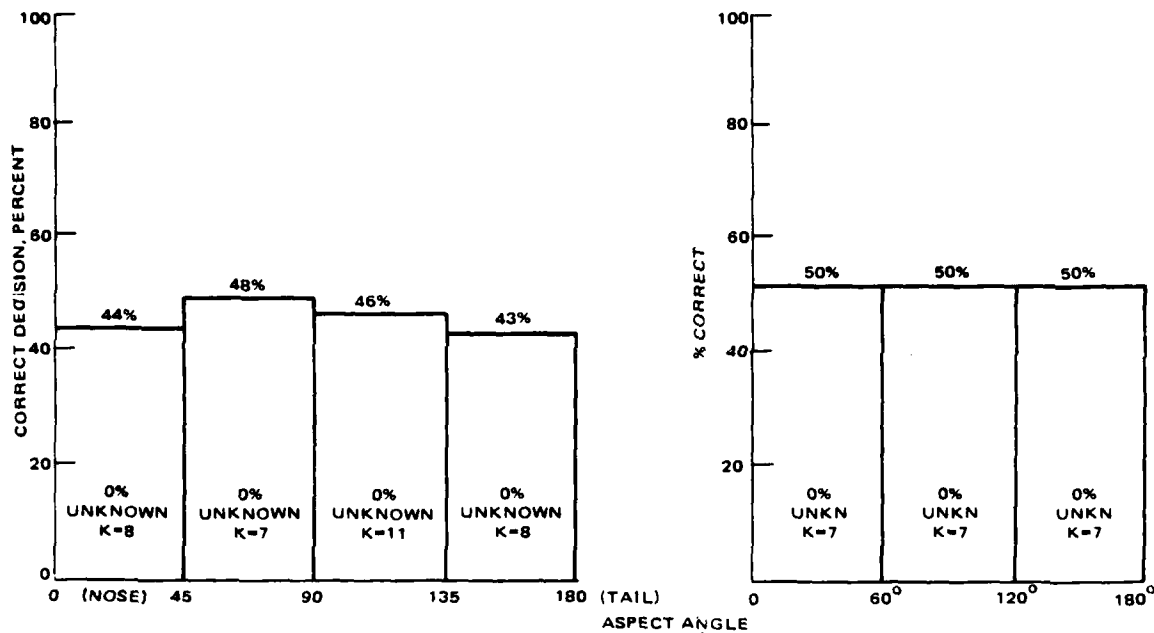
Figure 48. Classification performance of 24 invariants (best 12 from image and best 12 from edge detected image) with the kth nearest neighbor. Invariants were normalized by the radius of gyration.

...87 to 90 degrees). Figure 49 summarizes the classification results for the best 12 invariants from the image using the kth nearest neighbor rule and Figure 50 summarizes the results obtained using the kth nearest neighbor with a feature vector made up of the six best invariants from the image and the six best invariants from the edge detected image. Results obtained using the Gaussian classifier with the best 12 and best 17 variants from the image and also with the best six and six invariants (image and edge detected image) and with the best nine and nine are tabulated in Tables 9 through 12. For the above classification tests the invariant moment functions were normalized by the factor r^k where r is the radius of gyration defined in Equation (25) and the power k depends on the order of the invariant and is obtained using the algorithm described in Appendix A. Some classification tests were also performed where the invariants were normalized by their standard deviations (over all aspects and targets) rather than by the powers of the radius of gyration. Figure 51 shows the classification performance obtained using the 12 best normalized invariants from the image and 12 best normalized invariants

95
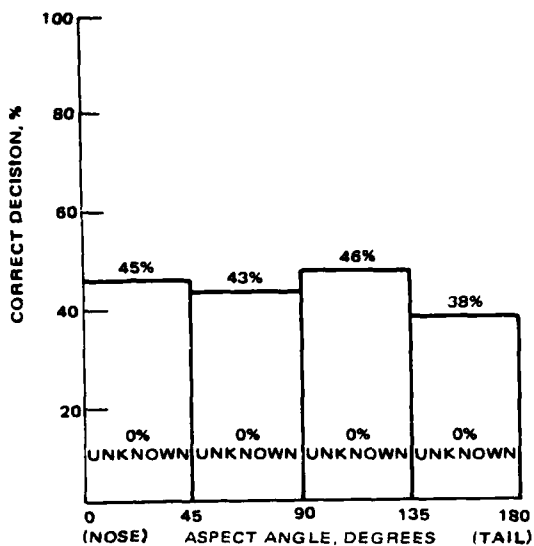
Figure 49. Classification performance of best
12 invariants using kth nearest
neighbor classifier. Invariants
normalized by radius of gyration.
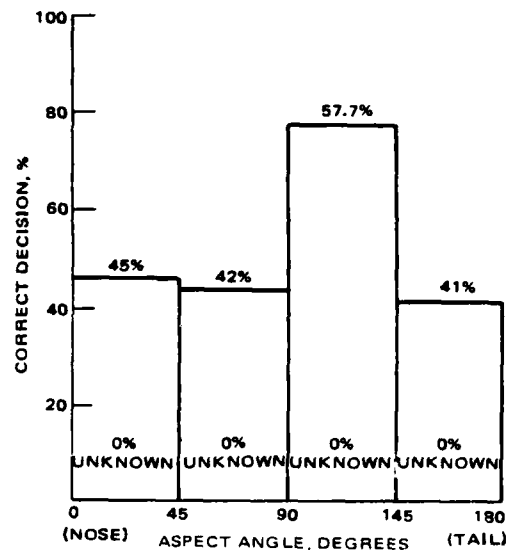
Figure 50. Classification performance of 12
invariants (best 6 from image and
best 6 from edge detected image)
using kth nearest neighbor
classifier. Invariants normalized
by radius of gyration.
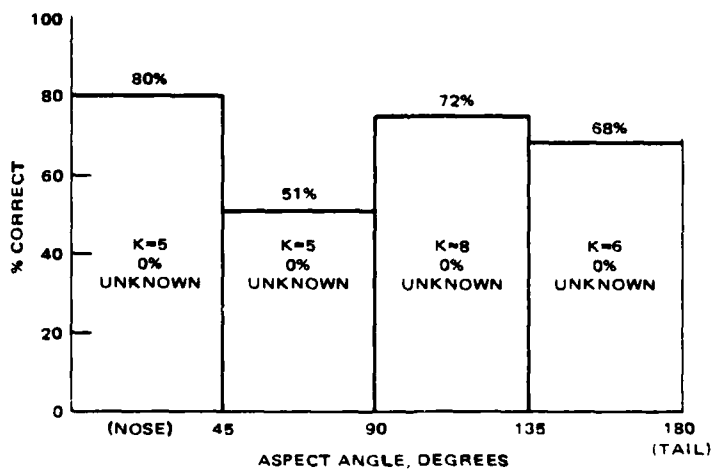
Figure 51. Classification results (1m resolution plan views 6 targets)
using the kth nearest neighbor with 24 invariants (12 best
from image and 12 best from edge detected image)
normalized by their standard deviations rather than by
powers of the radius of gyration.

TABLE 9. CLASSIFICATION RESULTS FOR 45° SECTORS FOR THE BEST 12 INVARIANTS FROM THE IMAGE USING THE GAUSSIAN CLASSIFIER WITH β = 99 PERCENT AND q = 0.7

FOR SECTOR #1

TARGET:	**IDENTIFIED AS**						
	F-102	F-15	F-16	F-5E	A-10	F-111	UK
F-102	7	1	1	0	0	0	0
F-15	1	7	0	1	0	0	0
F-16	2	1	4	1	0	0	1
F-5E	0	3	0	6	0	0	0
A-10	0	1	0	0	8	0	0
F-111	0	0	0	0	0	9	0

PROBABILITY FOR A CORRECT DECISION 77%

FOR SECTOR #2

TARGET:	**IDENTIFIED AS**						
	F-102	F-15	F-16	F-5E	A-10	F-111	UK
F-102	4	0	1	0	4	0	0
F-15	2	3	0	1	1	1	1
F-16	1	2	0	3	0	0	3
F-5E	2	1	1	5	0	0	0
A-10	0	0	0	2	4	2	1
F-111	0	0	0	0	0	9	0

PROBABILITY FOR A CORRECT DECISION 51%

FOR SECTOR #3

TARGET:	**IDENTIFIED AS**						
	F-102	F-15	F-16	F-5E	A-10	F-111	UK
F-102	7	0	1	0	0	0	1
F-15	0	8	0	1	0	0	0
F-16	4	0	4	0	0	0	1
F-5E	2	1	1	4	0	0	1
A-10	1	2	0	1	3	0	2
F-111	0	0	0	0	0	0	0

PROBABILITY FOR A CORRECT DECISION 65%

FOR SECTOR #4

TARGET:	**IDENTIFIED AS**						
	F-102	F-15	F-16	F-5E	A-10	F-111	UK
F-102	7	0	2	0	0	0	0
F-15	0	3	4	0	0	0	2
F-16	5	3	1	0	0	0	0
F-5E	2	0	3	3	0	0	1
A-10	5	2	1	2	3	2	0
F-111	0	0	0	0	0	0	0

PROBABILITY FOR A CORRECT DECISION %

TABLE 10. CLASSIFICATION RESULTS FOR 45° SECTORS FOR THE
BEST 12 INVARIANTS (6 FROM IMAGE AND 6 FROM EDGE DETECTED
IMAGE) USING THE GAUSSIAN CLASSIFIER WITH β = 99 PERCENT AND
q = 0.5

FOR SECTOR #1.

TARGET:	**IDENTIFIED AS**						
	F-102	F-15	F-16	F-5E	A-10	F-111	UK
F-102	7	0	1	0	1	0	0
F-15	1	5	2	1	0	0	0
F-16	1	1	5	2	0	0	0
F-5E	0	2	1	6	0	0	0
A-10	2	0	0	0	7	0	0
F-111	0	0	0	0	0	9	0

PROBABILITY FOR A CORRECT DECISION 72%
PERCENT UNKNOWN 0%

FOR SECTOR #2

TARGET:	**IDENTIFIED AS**						
	F-102	F-15	F-16	F-5E	A-10	F-111	UK
F-102	2	1	5	1	0	0	0
F-15	1	3	2	2	1	0	0
F-16	0	0	7	1	0	1	0
F-5E	0	0	2	6	0	1	0
A-10	1	0	1	0	4	0	0
F-111	0	0	0	0	0	9	0

PROBABILITY FOR A CORRECT DECISION 57%
PERCENT UNKNOWN 0%

FOR SECTOR #3

TARGET:	**IDENTIFIED AS**						
	F-102	F-15	F-16	F-5E	A-10	F-111	
F-102	7	0	2	0	0	0	
F-15		8	1	0	0	0	
F-16		0	5	2	0	0	
F-5E		0	0	7	0	0	
A-10							
F-111	0	0					

PROBABILITY FOR A CORRECT DECISION 70%
PERCENT UNKNOWN 0%

FOR SECTOR #4

TARGET:	**IDENTIFIED AS**						
	F-102	F-15	F-16	F-5E	A-10	F-111	
F-102	7						
F-15		5		1			
F-16							
F-5E							
A-10							
F-111							

TABLE 11. CLASSIFICATION RESULTS FOR 60° SECTORS FOR THE
BEST 17 INVARIANTS FROM THE IMAGE USING THE GAUSSIAN CLASSIFIER
WITH β = 99 PERCENT, q = 0.0

FOR   SECTOR   #1.

TARGET: **IDENTIFIED AS**

	F-102	F-15	F-16	F-5E	A-10	F-111	UK
F-102	9	0	2	0	0	0	1
F-15	0	7	1	1	0	0	3
F-16	1	2	6	1	0	0	2
F-5E	0	1	1	10	0	0	0
A-10	2	0	0	0	10	0	0
F-111	0	0	0	0	0	12	0

PROBABILITY FOR A CORRECT DECISION 81%
PERCENT UNKNOWN 8%

FOR   SECTOR   #2

TARGET: **IDENTIFIED AS**

	F-102	F-15	F-16	F-5E	A-10	F-111	UK
F-102	7	0	2	1	2	0	0
F-15	4	6	0	0	2	0	0
F-16	2	2	3	0	2	0	3
F-5E	1	1	0	6	1	0	3
A-10	1	0	1	1	6	0	1
F-111	0	0	0	0	0	0	0

PROBABILITY FOR A CORRECT DECISION 56%
PERCENT UNKNOWN 12%

FOR   SECTOR   #3

TARGET: **IDENTIFIED AS**

	F-102	F-15	F-16	F-5E	A-10	F-111	UK
F-102	10	0	0	1	0	0	1
F-15	2	5	3	1	0	0	1
F-16	2	0	6	2	0	0	2
F-5E	1	1	1	7	0	0	2
A-10	0	1	0	2	9	0	0
F-111	0	0	0	0	0	0	0

PROBABILITY FOR A CORRECT DECISION 68%
PERCENT UNKNOWN 10%

TABLE 12. CLASSIFICATION RESULTS FOR THE BEST 18 INVARIANTS
(9 FROM IMAGE AND 9 FROM EDGE DETECTED IMAGE USING THE
GAUSSIAN CLASSIFIER WITH β = 99 PERCENT AND q = 0.0

FOR SECTOR #1.

TARGET: **IDENTIFIED AS**

	F-102	F-15	F-16	F-5E	A-10	F-111	UK
F-102	7	4	0	1	0	0	6
F-15	0	9	1	1	0	0	1
F-16	2	2	7	0	0	0	1
F-5E	0	2	0	10	0	0	5
A-10	0	0	0	0	12	0	0
F-111	0	0	0	0	0	12	4

PROBABILITY FOR A CORRECT DECISION 81%
PERCENT UNKNOWN   3%

FOR SECTOR #2

TARGET: **IDENTIFIED AS**

	F-102	F-15	F-16	F-5E	A-10	F-111	UK
F-102	6	0	3	1	2	0	
F-15	5	3	1	1	1	0	1
F-16	3	0	5	1	1	0	3
F-5E	2	0	2	7	0	0	1
A-10	0	0	1	1	5	0	
F-111	0	0	6	0	0	0	

PROBABILITY FOR A CORRECT DECISION 46%
PERCENT UNKNOWN 10%

FOR SECTOR #3

TARGET: **IDENTIFIED AS**

	F-102	F-15	F-16	F-5E	A-10	F-111	UK
F-102	10	0	0	1	0	0	0
F-15	4	4	2	1	0	0	1
F-16	3	1	4	1	0	0	2
F-5E	2	0	1	9	0	0	1
A-10	2	2	1	0	7	0	0
F-111	0	0	0	0	0	1	

PROBABILITY FOR A CORRECT DECISION 60%
PERCENT UNKNOWN   7%

from the edge detected image. By comparing these results in Figure 51 to those of Figure 48 obtained for the invariants that were normalized by the radius of gyration, an average improvement is seen in classification performance of the order of 30 percent. Using the 33 invariants obtained from the image without any normalization an optimum transformation matrix H was computed as described in section 5.4 and the 33 dimensional vector of the invariants was projected into a 5 dimensional subspace. The resulting 5 dimensional feature vector was used to classify the five RATSCAT targets using the Gaussian classifier. The results are given in Table 13. From this table, classification performance is seen to be 86 percent for nose aspects and 75 percent for tail aspects, for the 1 meter resolution plan view images.

As seen in the figures and tables tabulating the classification performance for the invariant moment functions, the best results for the kth nearest neighbor tests are of the order of 51 percent to 80 percent correct shown in Figure 51. Comparing these results with those corresponding to classification using the moments (Figure 34), the central moments give on an average 10 percent better results. The same trend favoring the feature vector from the moments over that of the invariants is observed by comparing the results obtained using the feature vector formed by the best 18 invariants from the image and the corresponding feature vector formed using moments. By comparing the results in Table 11 with those of Table 5, the performance is about the same for both features for nose aspects but for all other aspects the feature vector using the central moments gives 10 to 15 percent better results. Thus the tests show that the moments perform much better than the invariants.

6.3 CLASSIFICATION RESULTS USING GENERAL ALGEBRAIC INVARIANT MOMENT FUNCTIONS

In our discussion of invariant moment functions a set of relations among the moments of an image that are invariant with respect to general coordinate transformations were presented in Equations 32 through 38. These functions of the moments are invariant with respect to both rotations and non uniform scale changes of the coordinates thus they are particularly

suitable for the recognition of inverse SAR images where the cross range scale may not be known accurately. For the classification tests using these general algebraic invariants, only the three general invariants obtained by Hu [7] and repeated in Equations 32 through 35 were used. With these formulas, three general invariants from the image and three from the edge detected image were computed and used to form a six-dimensional feature vector. This feature vector was then used to classify the plan view images obtained from the RATSCAT targets and the results for the 1 meter resolution images are presented in Table 14. As seen in this table the performance of this feature vector is poor (46 to 62 percent correct). The main reason for this poor performance is probably the low dimensionality of the feature vector. In an attempt to improve the performance of the above features without deriving new formulas to compute higher order general invariants, the dimensionality of the feature vector was increased from 6 to 27 by including the squares and by two products of the components of the original 6 dimensional feature vector. Then as described in Section 5.4, a transformation matrix was obtained to reduce the dimensionality of this new 27 dimensional feature vector down to 5. The Gaussian classifier was then trained and tested using this 5 dimensional feature vector and the results are tabulated in Table 15. The results are still not too good (66 to 71 percent correct), although there is some improvement over the results of Table 14 for all aspects.

5.4 CLASSIFICATION RESULTS USING RANGE AND CROSS RANGE COLLAPSING

As described in Section IV, the target orientation in the image plane is estimated using Equation (39) and the co-ordinate axes are rotated so that the y-axis (range) lines up with the fuselage. The intensity distribution of the image is then averaged along the x and y axes to produce average y-axis and x-axis intensity profiles. A feature vector is then computed using the correlation coefficients for each of these two profiles as shown in Figure 25. Using the 1 meter resolution images, the first 15 correlation coefficients were computed from the x-axis and the y-axis intensity profiles. Using the Mahalanobis distance criterion, the correlation coefficients were

TABLE 13. CLASSIFICATION RESULTS for 45° SECTORS FOR A
FEATURE VECTOR OBTAINED BY PROJECTING INTO A 5-DIMENSIONAL
SUBSPACE THE 33 ELEMENT INVARIANT FUNCTIONS VECTOR OBTAINED
FROM THE IMAGE INTENSITY DISTRIBUTION.

TABLE 14. CLASSIFICATION RESULTS FOR SIX GENERAL ALGEBRAIC INVARIANTS (3 FROM IMAGE AND 3 FROM THE EDGE DETECTED IMAGE) USING THE GAUSSIAN CLASSIFIER (NO UNKNOWN)

FOR SECTOR #1

TARGET: **IDENTIFIED AS**

	F-102	F-15	F-16	F-5E	A-10	F-111	UK
F-102	3	0	5	0	1	0	0
F-15	1	3	3	1	1	0	0
F-16	2	0		0	0	0	0
F-5E	2	3	0	4	2	0	0
A-10	0	2	0	2	2	0	0

PROBABILITY FOR A CORRECT DECISION 51%
PERCENT UNKNOWN 0%

FOR SECTOR #2

TARGET: **IDENTIFIED AS**

	F-102	F-15	F-16	F-5E	A-10	F-111	UK
F-102	3	2	0	1	2	0	0
F-15	0	1	3	2	0	0	1
F-16	1	2	3	1	1	0	0
F-5E	0	0	0	7	2	0	0
A-10	0	1	1	0	5	0	0

PROBABILITY FOR A CORRECT DECISION 46%
PERCENT UNKNOWN 0%

FOR SECTOR #3

TARGET: **IDENTIFIED AS**

	F-102	F-15	F-16	F-5E	A-10	F-111	UK
F-102	7	0	0	2	0	0	0
F-15	0	6	1	0	0	3	0
F-16	0	3	0	4	2	0	0
F-5E	2	0	0	5	2	0	0
A-10	1	0	1	1	4	0	0

PROBABILITY FOR A CORRECT DECISION 57%
PERCENT UNKNOWN 0%

FOR SECTOR #4

TARGET: **IDENTIFIED AS**

	F-102	F-15	F-16	F-5E	A-10	F-111	UK

PROBABILITY FOR A CORRECT DECISION 52%
PERCENT UNKNOWN 0%

TABLE 15. CLASSIFICATION RESULTS FOR A FEATURE VECTOR COMPUTED BY INCLUDING THE SQUARES AND BY TWO PRODUCTS OF THE SIX GENERAL INVARIANTS (3 FROM IMAGE AND 3 FROM EDGE DETECTED IMAGE) AND THEN PROJECTING THE RESULTING 27 DIMENSIONAL VECTORS ONTO A 5-DIMENSIONAL FEATURE VECTOR

FOR SECTOR #1.

```
TARGET:                **IDENTIFIED AS**
            F-102   F-15   F-16   F-5E   A-10   F-111   UK
F-102        ?      ?      ?      ?      ?      ?       ?
F-15         0      ?      ?      ?      ?      0       ?
F-16         ?      ?      ?      0      ?      ?       ?
F-5E         0      ?      0      ?      ?      ?       ?
A-10         ?      0      ?      0      ?      0       ?
```
PROBABILITY FOR A CORRECT DECISION 71%
PERCENT UNKNOWN 0%

FOR SECTOR #2

```
TARGET:                **IDENTIFIED AS**
```
PROBABILITY FOR A CORRECT DECISION 57%
PERCENT UNKNOWN 0%

FOR SECTOR #3

```
TARGET:                **IDENTIFIED AS**
```
PROBABILITY FOR A CORRECT DECISION 68%
PERCENT UNKNOWN 0%

FOR SECTOR #4

```
TARGET:                **IDENTIFIED AS**
```
PROBABILITY FOR A CORRECT DECISION 56%
PERCENT UNKNOWN 1%

ranked and the resulting ordering for the best 24 was found to be:

$$R_y(1), \ R_y(2), \ R_x(1), \ R_x(2), \ R_y(3), \ R_x(3),$$
$$R_x(4), \ R_x(5), \ R_y(14), \ R_y(13), \ R_y(7), \ R_y(12),$$
$$R_y(4), \ R_y(9), \ R_y(8), \ R_x(15), \ R_y(14), \ R_x(13),$$
$$R_x(10), \ R_x(8), \ R_x(6), \ R_x(12), \ R_x(7), \ R_x(9)$$

where y is the co-ordinate along the fuselage and x is the co-ordinate parallel to the wings. The classification performance of a feature vector using all 30 correlation coefficients was tested using the kth nearest neighbor rule and the results are presented in Figure 52. The classification performance for the best 24 correlation coefficients and the best 12 was also tested and the results of the order of 70 to 88 percent correct. These are comparable to many of the results obtained using the central moments but are about 10 percent below the best performance results obtained using the best 24 moments (best 12 from image and best 12 from edge detected image).
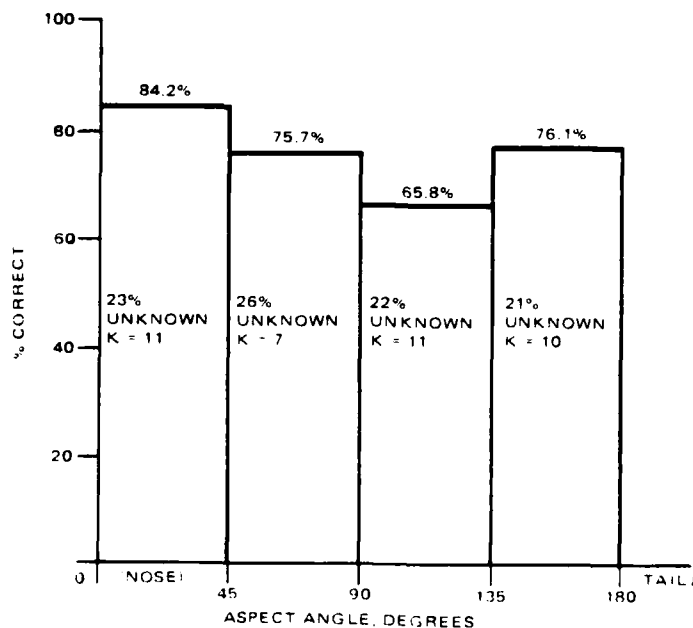

Figure 52. Classification performance using Kth nearest neighbor for 30 correlation coefficients from collapsed images.
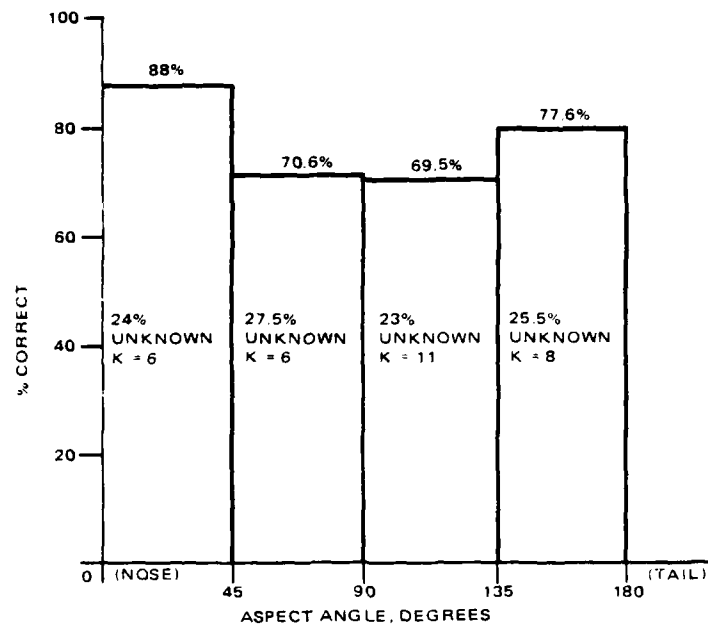
Figure 53. Classification performance using Kth nearest neighbor
with best 24 correlation coefficients from collapsed
images.
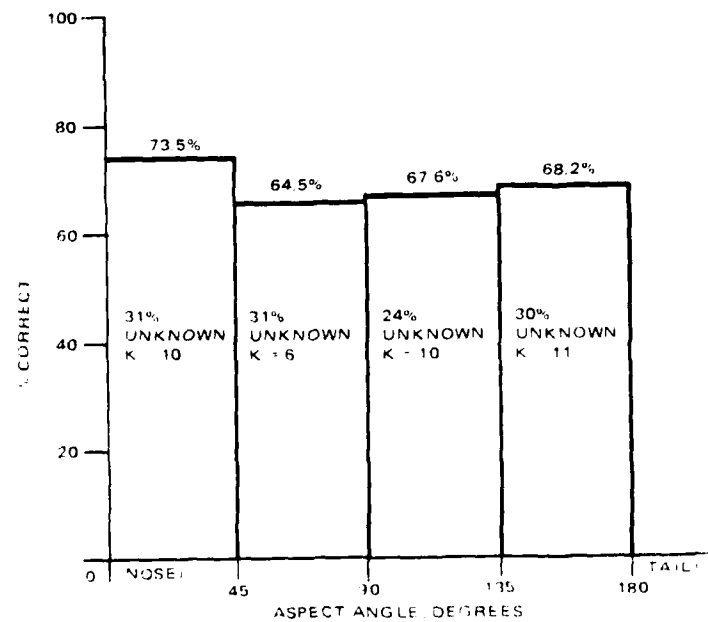
Figure 54   Classification performance using Kth nearest neighbor
with best 12 correlation coefficients from collapsed
images.

Section VII
CONCLUSIONS

Summarizing the results presented in Section VI, it can be observed that in general the best performance results were obtained using feature vectors constructed from the moments of the image and the edge detected image. For the plan view images of the six aircraft targets (F-102, YF-16, F-15, F-5E, A-10 and F-111, the performance results for a 24-element feature vector constructed using 12 best moments from the image and 12 best moments from the edge detected image are in the range of 84 to 96 percent as seen in Figure 39 which is repeated here in Figure 55. Using the dimensionality reduction procedure described in Subsection 5.4, a 5-element feature
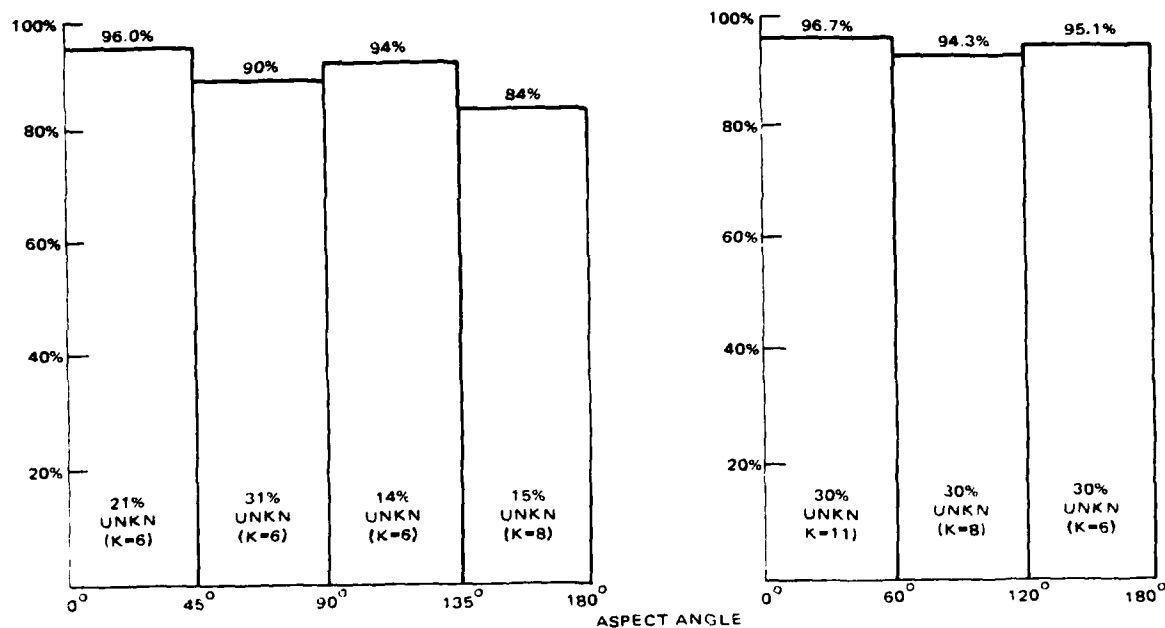
Figure 55. Kth nearest neighbor classification results (1m resolution plan views 6 classes) for 24 moments (12 best from image and 12 best from edge detected image) normalized by their standard deviations with provision for unknown.

107

vector was constructed by projecting into a 5-dimensional subspace the 33
element moment vector obtained from the image intensity. The classification
performance of this feature vector was tested using the 1-meter resolution
plan view images of the five RATSCAT targets and the results are shown in
Table 16. In general as shown in the results in Section VI, the best
classification performance obtained using the invariant functions was about
10 to 15 percent below the best results obtained using the moments. In
general the tests showed that moments from the image did better than moments
from the edge detected image, but feature vectors using combinations between
the two sets had a high classification performance.

The observed classification results with feature vectors obtained by
averaging the image intensity along two orthogonal axes (parallel and normal
to the fuselage) and then computing the autocorrelation function was 70 to
88 percent which is 10 percent less than the results obtained using the central
moments. Since the computational requirements for the construction of
this feature vector are considerably smaller than the computational require-
ments for obtaining the geometric moments and invariants, this feature
vector may prove useful in cases where classification accuracies of the
order of 70 to 88 percent are sufficient.

In general, the results from the performance tests conducted during
this study are encouraging and suggest that the geometric moments may prove
to be important features for the application of statistical pattern recognition
techniques to the identification of aircraft targets from radar images. How-
ever, because a limited set of imaging geometries (only plan views cor-
responding to projections on the horizontal plane for zero roll and profiles
corresponding to projections on the vertical plane) was used in this study the
performance of the techniques as a function of roll and pitch angles was not
investigated. Furthermore, it was assumed that the imaging plane was known.
The determination of the target view presented by the image is an important
problem that needs to be solved before the above recognition techniques can
be used in a completely unsupervised mode. This problem will be addressed
in follow-on work in this area.

TABLE 16. CLASSIFICATION RESULTS FOR 45° SECTORS FOR A FEATURE
VECTOR OBTAINED BY PROJECTING INTO A 5-DIMENSIONAL SUBSPACE
THE 33 ELEMENT MOMENT VECTOR OBTAINED FROM THE IMAGE
INTENSITY DISTRIBUTION.

FOR SECTOR #1.

TARGET: **IDENTIFIED AS**
              F-102   F-15   F-16   F-5E   A-10   F-111   UK
   F-102   9   0   0   0   0   0   0
   F-15   1   3   0   0   0   0   0
   F-16   0   0   0   0   0   0   0
   F-5E   0   0   0   2   0   0   0
   A-10   0   0   0   0   0   0   0
PROBABILITY FOR A CORRECT DECISION 97%
PERCENT UNKNOWN 0%

FOR SECTOR #2

TARGET: **IDENTIFIED AS**

              0   1
   A-10
PROBABILITY FOR A CORRECT DECISION 94%
PERCENT UNKNOWN 0%

FOR SECTOR #3

TARGET: **IDENTIFIED AS**

PROBABILITY FOR A CORRECT DECISION 95%
PERCENT UNKNOWN 0%

FOR SECTOR #4

PROBABILITY FOR A CORRECT DECISION 95%
PERCENT UNKNOWN 0%

Section VIII
REFERENCES

1. Chen, C.C. and Andrews, H.C., "Multifrequency Imaging of Radar Turntable Data," IEEE Trans. on AES, Vol. 6, pp. 15-22, 1980

2. Walker, J.L., "Range-Doppler Imaging of Rotating Objects, IEEE Trans. on AES," Vol. 6, pp. 23-52, 1980.

3. Wehner, D.R., "Stepped-Frequency Target Imaging," in Non-Cooperative Target Recognition Workshop Proc., Rome Air Development Center, October 1978.

4. Lewis, R.M., "Physical Optics Inverse Diffraction," IEEE Trans. on Antenna and Prop., Vol. AP-17, pp. 308-314, 1969.

5. Brown, W.M. and R.J. Fredricks, "Range-Doppler Imaging with Motion Through Resolution Cells," IEEE Trans. on AES, Vol. 5, p. 98, 1969.

6. Dudani, S.A., Breeding, K.J., and McGhee, R.B., "Aircraft Identification by Moment Invariants," IEEE Trans. on Computers, Vol. C-26, pp. 39-45, 1977.

7. Hu, M.K., "Visual Patten Recognition by Moment Invariants," IRE Trans. on Information Theory, pp. 179-187, 1962.

8. Gonzales, R.C., and Moret, B.M.E., "A Recursive Procedure for Updating Quadratic Forms and Its Application to Feature Selections," ONR-CR215-288-3F, 1978.

9. Friedman, J.H., Gaskett F., and Shustek, L.R., "An Algorithm for Finding Nearest Neighbors," IEEE Trans. on Computers, pp. 1000-1006, 1975.

10. Rao, C.R., Linear Statistical Inference and Its Applications, John Wiley and Sons, New York, 1973.

11. Jenkins, G.M. and Watts, D.G., Spectral Analysis and Its Applications, Holden-Day, San Francisco, 1969.

12. Scheffe, H., The Analysis of Variance, John Wiley, New York, 1959.

13. Graupe, D., <u>Identification of Systems</u>, Van Nost and Reinhold
     Co., New York, 1972.

14. Chen, C.C. and Andrews, H.C., "Target-Motion Induced Radar
     Imaging," IEEE Trans. on AES, Vol. 16, pp. 2-14, 1980.

APPENDIX A

ORTHOGONAL MOMENT INVARIANTS

by Jon P Belleville

A.1. INTRODUCTION

One of the more difficult problems in the design of a system to recognize objects from their images is the selection of a set of appropriate numerical features to be extracted from the shape of interest for purposes of classification. Such a set of features that has been successfully applied to the recognition of optical pictures is a set of invariant moment functions [1], [2], [3], which are discussed in this appendix.

A.2. MOMENTS

The two-dimensional (p+q)th order moments of an intensity distribution function f(x, y) are defined by

$$n_{pq} = \int_{-\infty}^{\infty} \int_{-\infty}^{\infty} x^p y^q f(x, y) \, dx dy \, , \qquad p, q = 0, 1, 2, \ldots$$

It is assumed that f(x, y) is a piecewise continuous and therefore bounded function, and that it can have nonzero values only in the finite part of the xy plane; then moments of all orders exist and the following uniqueness theorem can be proved. Theorem: the double moment sequence $\{n_{pq}\}$ is uniquely determined by f(x, y); and conversely, f(x, y) is uniquely determined by $\{n_{pq}\}$. It should be noted that the finiteness assumption is important; otherwise the theorem might not hold. It can be shown that this theorem holds in the discrete case as well. In the discrete case the (p+q)th order moments of an NxM rectangular image field $f(x_i, y_j)$ are defined by

$$n_{pq} = \sum_{i=1}^{N} \sum_{j=1}^{M} f(x_i, y_j)(x_i)^p (y_j)^q$$

where (x_i, y_j) are the coordinates of the (i, j) cell and $f(x_i, y_j)$ is the image intensity function.

The central moments for the same rectangular image field are defined by

$$m_{pq} = \sum_{i=1}^{N} \sum_{j=1}^{M} f(x_i, y_j)(x_i - \bar{x})^p (y_j - \bar{y})^q \qquad (A-1)$$

where:

$$\bar{x} = \frac{n_{10}}{n_{00}}$$

and

$$\bar{y} = \frac{n_{01}}{n_{00}}$$

The normalized central moments are defined by

$$\mu_{pq} = \frac{m_{pq}}{m_{00}} \qquad (A-2)$$

and are invariant with respect to changes in the image intensity. In what follows, by moments we refer to these normalized central moments.

To see that the normalized moments are invariant with respect to changes in image intensity let $g(x, y) = c \cdot f(x, y)$, where c is some non-zero constant. Then letting the primed moments be those computed from $g(x, y)$:

$$m'_{pq} = \sum_{i=1}^{N} \sum_{j=1}^{M} g(x_i, y_j)(x_i - \bar{x})^p (y_j - \bar{y})^q$$

which can be rewritten as:

$$m'_{pq} = c \cdot \sum_{i=1}^{N} \sum_{j=1}^{M} f(x_i, y_j)(x_i - \bar{x})^p (y_j - \bar{y})^q .$$

A-2

Thus $m'_{pq} = c \cdot m_{pq}$, and from Equation (2-2)

$$\mu'_{pq} = \frac{m'_{pq}}{m'_{00}} = \frac{c m_{pq}}{c m_{00}} = \mu_{pq} \ ,$$

which demonstrates that the normalized moments are invariant with respect to uniform changes in intensity. Also that the central moments and normalized central moments are invariant with respect to translations, as seen by examining Equation (A-1).

A.3 ALGEBRAIC FORMS AND INVARIANTS

A.3.1 Definitions

The set of moments developed above are invariant under translations and image intensity changes. However, since images may have any orientation in the image plane a set of features which remains constant under *rotation of the image is desirable.* Such a set has been developed by Hu[1], and is presented below.

First, some definitions and results will be stated. The following homogeneous polynomial of two variables u and v,

$$f = a_{po}u^p + \binom{p}{1} a_{p-1,1}u^{p-1}v + \binom{p}{2} a_{p-2,2}u^{p-2}v^2$$

$$+ \cdots + \binom{p}{p-1} a_{1,p-1}uv^{p-1} + a_{op}v^p \ , \tag{A-3}$$

is called a binary algebraic form, or simply a binary form, of order p. Using a notation, introduced by Cayley, the above form may be written [1] as

$$f = (a_{po}, a_{p-1,1}, \cdots, a_{op})(u, v)^p \ .$$

A homogeneous polynomial $I(a)$ of the coefficients $a_{po}, \ldots, a_{op}$ is an algebraic invariant of weight w, [1] if

$$I(a'_{po}, \ldots, a'_{op}) = \Delta^w I(a_{po}, \ldots, a_{op}),$$

where $a'_{po}, \ldots, a'_{op}$ are the new coefficients obtained from substituting the following general linear transformation into the original form (A-3).

$$\begin{bmatrix} u \\ v \end{bmatrix} = \begin{bmatrix} \alpha & \gamma \\ \beta & \delta \end{bmatrix} \begin{bmatrix} u' \\ v' \end{bmatrix}, \quad \Delta = \begin{vmatrix} \alpha & \gamma \\ \beta & \delta \end{vmatrix} \neq 0. \tag{A-4}$$

If $w = 0$, the invariant is called an absolute invariant; if $w \neq 0$ it is called a relative invariant.

In the study of invariants, it is helpful to introduce another pair of variables x and v, whose transformation with respect to (A-4) is as follows:

$$\begin{bmatrix} x' \\ v' \end{bmatrix} = \begin{bmatrix} \alpha & \beta \\ \gamma & \delta \end{bmatrix} \begin{bmatrix} x \\ v \end{bmatrix} \tag{A-5}$$

The transformation (A-5) is referred to as a cogredient transformation, and (A-4) is referred to as a contragredient transformation. The variables x, v are referred to as covariant variables, and u, v as contravariant variables. They satisfy the following invariant relation

$$ux + vy = u' x' + v' v'.$$

The Fundamental Theorem of Moment Invariants obtained by Hu [1] stated as follows:

If the algebraic form of order p has an algebraic invariant,

$$I(a'_{po}, \ldots, a'_{op}) = \Delta^w I(a_{po}, \ldots, a_{op}).$$

then the moments of order p have the same invariant but
with the additional factor J ,

$$I(\mu^-_{po}, \ldots, \mu^-_{op}) = |J| \Delta^W I(\mu_{po}, \ldots, \mu_{op}) .$$

where $|J|$ is the absolute value of the Jacobian
of the transformation (A-5).

A.3.2 Orthogonal Moment Invariants

In what follows Hu's [1] derivation of the orthogonal moment invariant functions is summarized. Two coordinate systems (x, y) and (x', y') rotated relative to each other by an angle θ are used. The two systems are related by the orthogonal matrix transformation

$$\begin{bmatrix} x' \\ y' \end{bmatrix} = \begin{bmatrix} \cos \theta & \sin \theta \\ -\sin \theta & \cos \theta \end{bmatrix} \begin{bmatrix} x \\ y \end{bmatrix}$$

whose Jacobian is

$$|J| = \begin{vmatrix} \cos \theta & \sin \theta \\ -\sin \theta & \cos \theta \end{vmatrix} = +1$$

Since $|J|=1$, the moment invariants are exactly the same as the algebraic invariants. If the moments are treated as the coefficients of an algebraic form

$$(\mu_{po}, \ldots, \mu_{op})(u, v)^p \tag{A-6}$$

under the contragredient transformation,

$$\begin{bmatrix} u \\ v \end{bmatrix} = \begin{bmatrix} \cos \theta & -\sin \theta \\ \sin \theta & \cos \theta \end{bmatrix} \begin{bmatrix} u' \\ v' \end{bmatrix} .$$

A-5

then the moment invariants can be derived by the following algebraic method.
If both u, v and u' v' are subjected to the transformation:

$$\begin{bmatrix} U \\ V \end{bmatrix} = \frac{1}{2}\begin{bmatrix} 1 & i \\ 1 & -i \end{bmatrix}\begin{bmatrix} u \\ v \end{bmatrix} \ , \quad \begin{bmatrix} U' \\ V' \end{bmatrix} = \frac{1}{2}\begin{bmatrix} 1 & i \\ 1 & -i \end{bmatrix}\begin{bmatrix} u' \\ v' \end{bmatrix} \tag{A-7}$$

then the orthogonal transformation is converted into the following simple
relations,

$$U' = U e^{-i\theta} \ , \quad V' = V e^{i\theta} \tag{A-8}$$

Substituting (A-7) and (A-8) into (A-6), yields the following identities:

$$(I_{po}, \ \ldots \ , \ I_{op})(U, V)^p \equiv (\mu_{po}, \ \ldots \ , \ \mu_{op})(u, v)^p$$

$$\equiv (\mu'_{po}, \ \ldots \ , \ \mu'_{op})(u', v')^p$$

$$\equiv (I'_{po}, \ \ldots \ , \ I'_{op})(U e^{-i\theta}, V e^{i\theta})^p , \tag{A-9}$$

where $I_{po}, \ \ldots \ I_{op}$ and $I'_{po}, \ \ldots \ I'_{op}$ are the corresponding coefficients
after the substitutions. From the identity in U and V, the coefficients of
the various monomials $U^{p-r}V^r$ on the two sides must be the same.
Therefore,

$$I'_{po} = e^{ip\theta} I_{po}; \ I'_{p-1, 1} = e^{i(p-2)\theta} \ I_{p-1, 1}; \ldots ;$$

$$I'_{1, p-1} = e^{-i(p-2)\theta} I_{1, p-1}; \ I'_{op} = e^{-ip\theta} I_{op} .$$

In general:

$$I'_{p-r, r} = e^{i (p-2r)\theta} \ I_{p-r, r} \tag{A-10}$$

where:

$$o \leq r \leq p .$$

From the identity of the first two expressions in (A-9), it follows that $I_{p-r, r}$ is the complex conjugate of $I_{r, p-r}$.

A general expression for $I_{p-r, r}$ in terms of the moments may be written as follows:

$$I_{p-r, r} = (\mu_{po}; \mu_{p-2, 2}; \cdots \mu_{p-2r, 2r}) (1, 1)^r;$$

$$(\mu_{p-1, 1}; \mu_{p-3, 3}; \cdots \mu_{p-2r-1, 2r+1})(1, 1)^r; \cdots ;$$

$$(\mu_{pr, p-2r}; \mu_{2r-2, p-2r+2}; \cdots ; \mu_{op})(1, 1)^r (1, -i)^{p-2r},$$

where $i = \sqrt{-1}$ and $p - 2r > 0$.

and

$$I_{p/2, p/2} = \mu_{po} + \binom{p/2}{1} \mu_{p-2, 2} + \binom{p/2}{2} \mu_{p-4, 4} + \cdots + \mu_{op},$$

$$p = \text{even}.$$

It may be noted that these (p+1) I's form a linearly independent set of linear transformations of the μ's, and vice versa. This can be rewritten in summation notation as follows:

$$I_{p-r, r} = \sum_{r=0}^{p-2r} \left[(-i)^n \binom{p-2r}{n} \left\{ \sum_{k=0}^{r} \binom{r}{k} \mu_{p-2k-n, 2k-n} \right\} \right] \qquad (A-11)$$

Separating into real and complex parts we get

$$I_{p-r,r} = \sum_{\substack{n=0,2,4 \\ n=\text{even}}}^{p-2r} \left[(-1)^{n/2} \binom{p-2r}{n} \left\{ \sum_{k=0}^{r} \binom{r}{k} \mu_{p-2k-n,\ 2k+n} \right\} \right]$$

$$+ (-i) \sum_{\substack{n=1,3,5 \\ n=\text{odd}}}^{p-2r} \left[(-1)^{(n-1)/2} \binom{p-2r}{n} \left\{ \sum_{k=0}^{r} \binom{r}{k} \mu_{p-2k-n,\ 2k+n} \right\} \right]$$

$$(A-12)$$

If $\binom{0}{0} \overset{\Delta}{=} 1$ and empty sums equal zero then equations (A-11) and (A-12) are valid for $p-2r \geq 0$.

Referring back to equation (A-10) it can be seen that if the I's are combined in such a manner as to eliminate the θ dependence, invariants are formed with respect to rotation. For example for $p=5$ and $r=2$ $I_{32} \cdot I_{23}$ is such an invariant. This can be seen by simply applying equation (A-10).

$$I_{32} \cdot I_{23} = e^{i(5-4)\theta} I_{32} \cdot e^{i(5-6)\theta} I_{23}$$

$$= I_{32} \cdot I_{23}$$

Furthermore, since the moments are invariant with respect to translation and changes in intensity the invariants formed from the I's also have these properties.

A complete system of orthogonal moment invariants developed by Teague is listed below for reference.

For the second-order moments the two independent invariants are

$$I_{11}, \quad I_{20} I_{02}$$

For the third-order moments the three independent invariants are

$$I_{30}I_{03}, \quad I_{21}I_{12} , \qquad\qquad (A-13)$$

$$(I_{30}I_{12}^3 + I_{03}I_{21}^3)$$

A fourth one depending also on the third-order moments is

$$\frac{1}{i} \cdot (I_{30}I_{12}^3 - I_{03}I_{21}^3) . \qquad\qquad (A-14)$$

The first three given by (A-13) are absolute invariants for both proper and improper rotations but the last one given by (A-14) is invariant only under proper* rotation, and changes sign under improper* rotation. This will be called a skew invariant. Therefore it is useful for distinguishing "mirror images." One more independent absolute invariant may be formed from second and third order moments as follows:

$$(I_{20}I_{12}^2 - I_{02}I_{21}^2)$$

For pth order moments, $p \geq 4$ we have $[p/2]$ (the integral part of $p/2$) invariants

$$I_{po}I_{op}; \quad I_{p-1,1}I_{1,p-1}; \cdots ; \quad I_{p-r,r}I_{r,p-r}; \cdots .$$

If p is even, then

$$I_{p/2,p/2} \text{ is also an invariant.}$$

Combining the pth order moments with the (p-2) order moments a set of $[p/2-1]$ invariants are obtained given by

$$(I_{p-1,1} I_{o,p-2} + I_{1,p-1} I_{p-2,0}) \, ,$$

$$(I_{p-2,2} I_{1,p-3} + I_{2,p-2} I_{p-3,1}) \, , \cdots ,$$

$$(I_{p-r,r} I_{r-1,p-r+1} + I_{r,p-r} I_{p-(r+1),r-1}) \, , \quad p-2r > 0, \ r \geq 1. \quad (A-15)$$

Also by combining the pth order moments with second-order moments, two additional invariants are obtained

$$\left(I^2_{[p/2],[p/2]+1} I_{20} + I^2_{[p/2]+1,[p/2]} I_{02} \right) \, ,$$

if p is odd, and

$$\left(I_{p/2-1,\ p/2+1} I_{20} + I_{p/2+1,\ p/2-1} I_{02} \right) \, , \qquad (A-16)$$

if p is even. Therefore there are always $(p+1)$ independent absolute invariants.

The invariants thus far developed are invariant with respect to translation, changes in intensity, rotation and reflection. However, they are not invariant with respect to scale changes. To adjust for scale changes each invariant is divided by a factor of r^k, as done by Dudani (2). The scaling factor r is defined as

$$r = \sqrt{(\mu_{20} + \mu_{02})} \, ,$$

which is itself an invariant (namely I_{11}) also known as the radius of gyration of the figure. The value of k depends upon the order of the I's used to form the invariants.

The values of k are as follows:

k = 2p for invariants of the form: $\qquad$ $I_{p-r,r} I_{r,p-r}$

k = p for invariants of the form: $\qquad$ $I_{p/2,p/2}$

k = p+q-n(r+s) for invariants of the form: $I_{pq} I^n_{rs} + I_{qp} I^n_{sr}$.

     This completes the development of orthogonal moment invariants. Hu [1] also developed a set of moment functions which is invariant under general nonsingular algebraic transformations. This set is briefly discussed in Section 3 of this report.

A.4 PROGRAMMING CONSIDERATIONS

     Basically, the algorithm to compute the invariants will be a straight line program; the I's are computed first and then combined to form invariants. However, there are a couple of points where the program may be optimized.

     First, not all the I's need to be computed since $I_{r,p-r}$ is the complex conjugate of $I_{p-r,r}$. Second, the calculation of $I_{p-r,r}$ as per equation (A-11) or (A-12) may be optimized by the use of a recursive procedure for computing $\binom{m}{n}$.

     For instance, if $\binom{m}{n}$ is known for some value of m and n and we wish to compute $\binom{m}{n-1}$ (assume that $o \leq n \leq m-1$). By expanding $\binom{m}{n}$ and $\binom{m}{n-1}$ then

$$\binom{m}{n} = \frac{m!}{(m-n)!\, n!}$$

$$\binom{m}{n-1} = \frac{m!}{(m-(n-1))!\, (n-1)!}$$

$$\binom{m}{n-1} = \frac{(m-n)!\, m!}{(n-1)!\, (m-n)!\, n!} = \frac{(m-n)}{(n-1)} \cdot \binom{m}{n}$$

A-11

Thus, the recursion relation is

$$\binom{m}{n+1} = \frac{(m-n)}{(n+1)} \cdot \binom{m}{n}$$

A.4.1 Program Verification

A program to compute the orthogonal moment invariants up to order seven using the results contained in this appendix is presented in a summary flow chart in Figure B-4 in Appendix B.

To check that the invariants computed are actually invariant with respect to rotation, a simple figure was used and the invariants calculated.

The figure used is shown in Figure A-1. The invariants that were calculated are listed in Table A-1. Record 1 contains the invariants for the original image and Record 2 are those for the rotated image. The two records are identical. Because the test figure is a straight line which is originally parallel to the x-axis all moments μ_{pq} with q>0 are zero. This results in many of the invariants reducing to the same numerical value and explains this occurrence in Table A-1.

The invariants in Table A-1 are numbered as follows. (The normalization by I_{11} is not shown)

$$\rho_1 = I_{20} I_{02}$$

ρ_2 through ρ_{17} have the form:

$$I_{p-n,n} I_{n,p-n} .$$

where $p = 3, 4, \dots, 7$, and $n = 0, 1, \dots, [p/2]$, and $[x]$ indicates the integral part of x. For the case when p is even $I_{p/2,p/2}$ is used instead of $I^2_{p/2,p/2}$.

The remaining invariants were arbitrarily labeled as follows

$$\rho_{18} = I_{30} I_{12}^3 + I_{03} I_{21}^3$$

$$\rho_{19} = -i \left(I_{30} I_{12}^3 - I_{03} I_{21}^3 \right) ,$$

$$\rho_{20} = I_{20} I_{12}^2 + I_{02} I_{21}^2$$

$$\rho_{21} = I_{31} I_{02} + I_{13} I_{20}$$

$$\rho_{22} = I_{41} I_{03} + I_{14} I_{30}$$

$$\rho_{23} = I_{32} I_{12} + I_{23} I_{21}$$

$$\rho_{24} = I_{51} I_{04} + I_{15} I_{40}$$

$$\rho_{25} = I_{42} I_{13} + I_{24} I_{31}$$

$$\rho_{26} = I_{71} I_{05} + I_{17} I_{50}$$
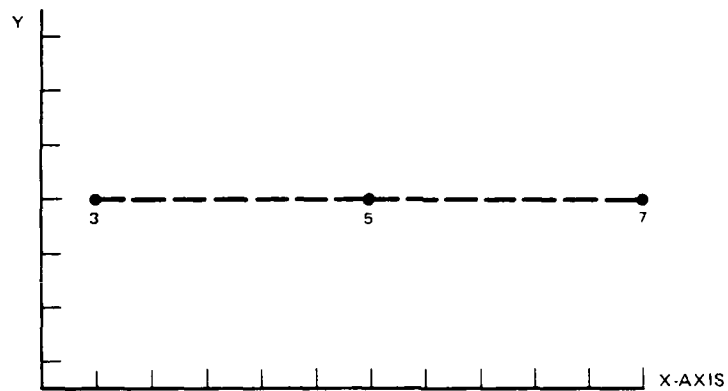
$$\rho_{27} = I_{52} I_{14} + I_{25} I_{41}$$

$$\rho_{28} = I_{43} I_{23} + I_{34} I_{32}$$

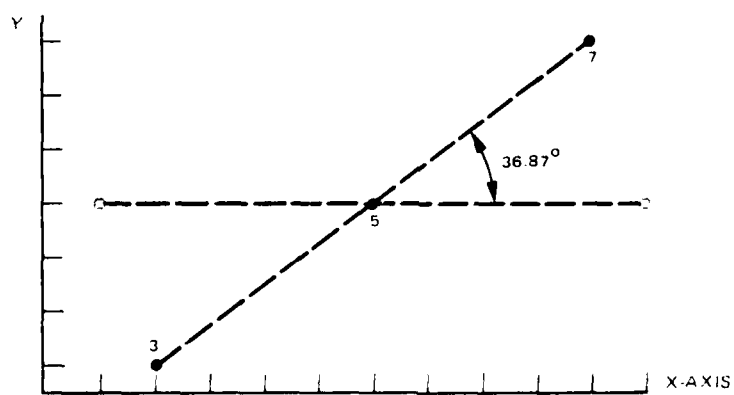$$\rho_{29} = I_{04} I_{20}^2 + I_{40} I_{02}^2$$

$$\rho_{30} = I_{23}^2 I_{20} + I_{32}^2 I_{02}$$

$$\rho_{31} = I_{24} I_{20} + I_{42} I_{02}$$

$$\rho_{32} = I_{34}^2 I_{20} + I_{43}^2 I_{02}$$

a. Test figure

b. Rotated figure

THE NUMBERS BY EACH POINT REPRESENT THE
RELATIVE BRIGHTNESS AT THAT POINT

Figure A-1.

TABLE A-1. INVARIANTS BEFORE AND AFTER ROTATION

n	Record 1 (Original) ρ_η	Record 2 (Rotated) ρ_η
1	1.00	1.00
2	0.248	0.248
3	0.248	0.248
4	3.37	3.37
5	3.37	3.37
6	1.84	1.84
7	4.09	4.09
8	4.09	4.09
9	4.09	4.09
10	18.1	18.1
11	18.1	18.1
12	18.1	18.1
13	4.25	4.25
14	37.1	37.1
15	37.1	37.1
16	37.1	37.1
17	37.1	37.1
18	0.123	0.123
19	0.0	$2.29 \times 10^{-8} \approx 0.0$
20	0.495	0.495
21	3.67	3.67
22	2.01	2.01
23	2.01	2.01
24	15.6	15.6
25	15.6	15.6
26	24.6	24.6
27	24.6	24.6
28	24.6	24.6
29	3.67	3.67
30	8.18	8.18
31	8.51	8.51
32	74.2	74.2

REFERENCES

1. Hu, M.K., "Visual Pattern Recognition by Moment Invariants," IRE Trans. on Information Theory, pp. 179-187, 1962

2. Dudani, S.A., Breeding, K.J., and R.B. McGhee, "Aircraft Identification by Moment Invariants," IEEE Trans. on Computers, Vol. C-26, pp. 39-45, 1977.

3. Gonzalez, R.C., and B.M.E. Moret, "A Recursive Procedure for Updating Quadratic Forms and its Application to Feature Selection," ONR-CR215-228-3F, 1978.

APPENDIX B
DESCRIPTION OF COMPUTER PROGRAMS USED
FOR THE CLASSIFICATION TESTS

by Charles P. Dolan

B.1 INTRODUCTION

In designing the software for this study, an effort was made to modularize the routines and use a uniform input output format for all the programs. Thus the same training and classification routines could be employed for all feature vectors used in the study. Also commonality among the routines for computing the moments and invariants allowed efficient program design. The flowcharts and block diagrams in this appendix summarize the computer programs needed for the computation of the moments and invariants, the normalization of the moments by their standard deviation over all targets and aspects, the nearest neighbor and Gaussian classifiers and the feature selection.
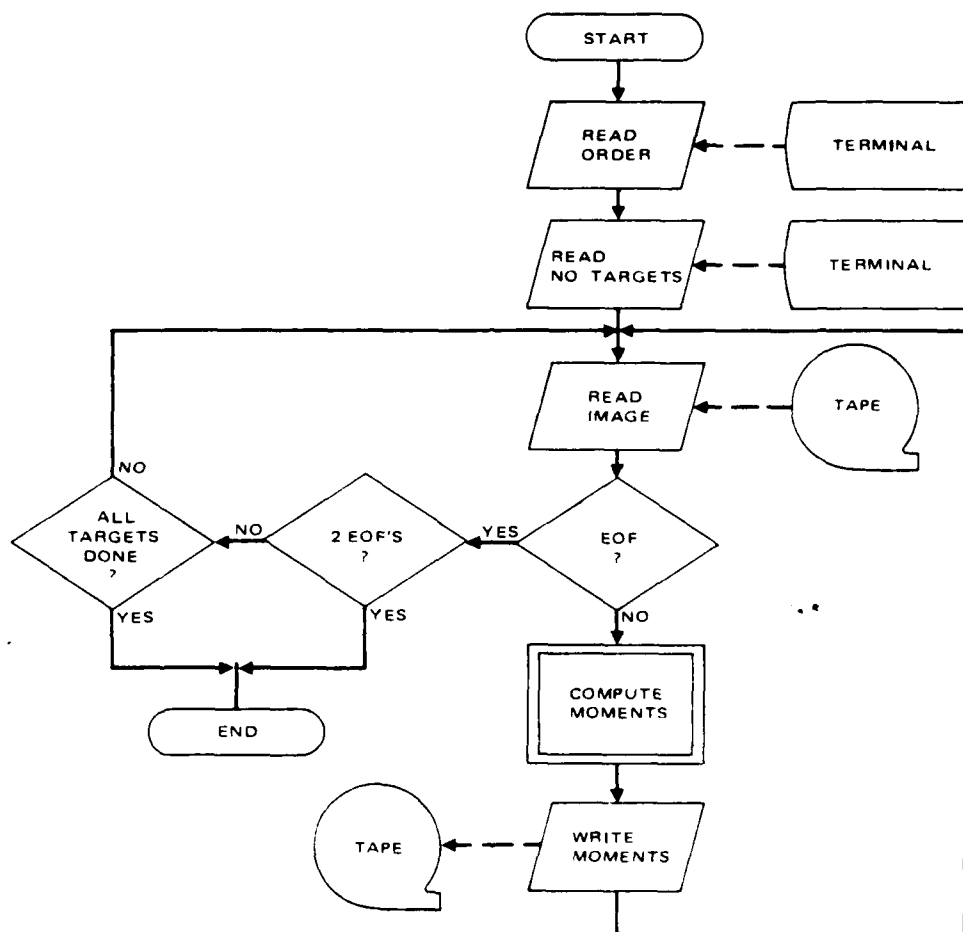
Figure B-1. Flow chart of program for computation of moments 1
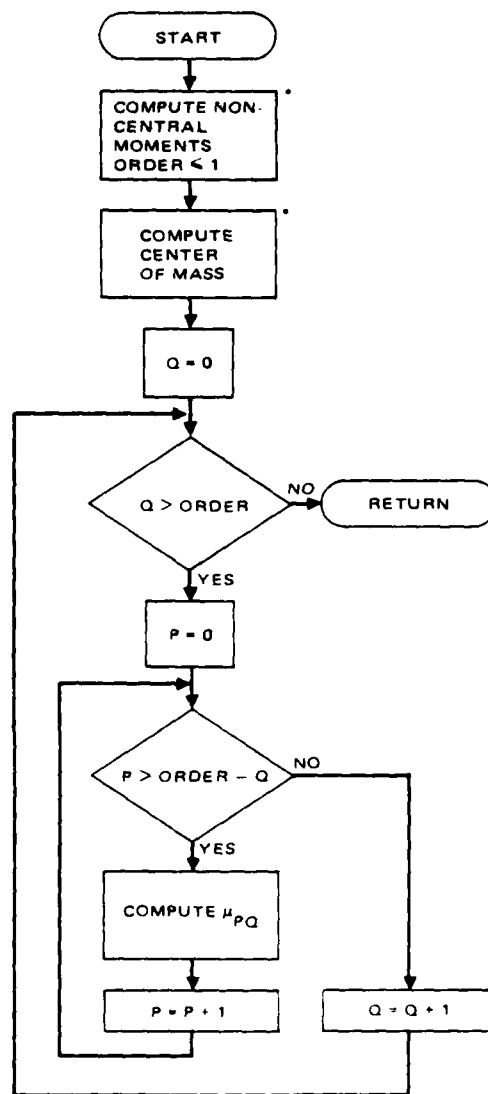
Figure B-2. Flow chart for computations of moments 2
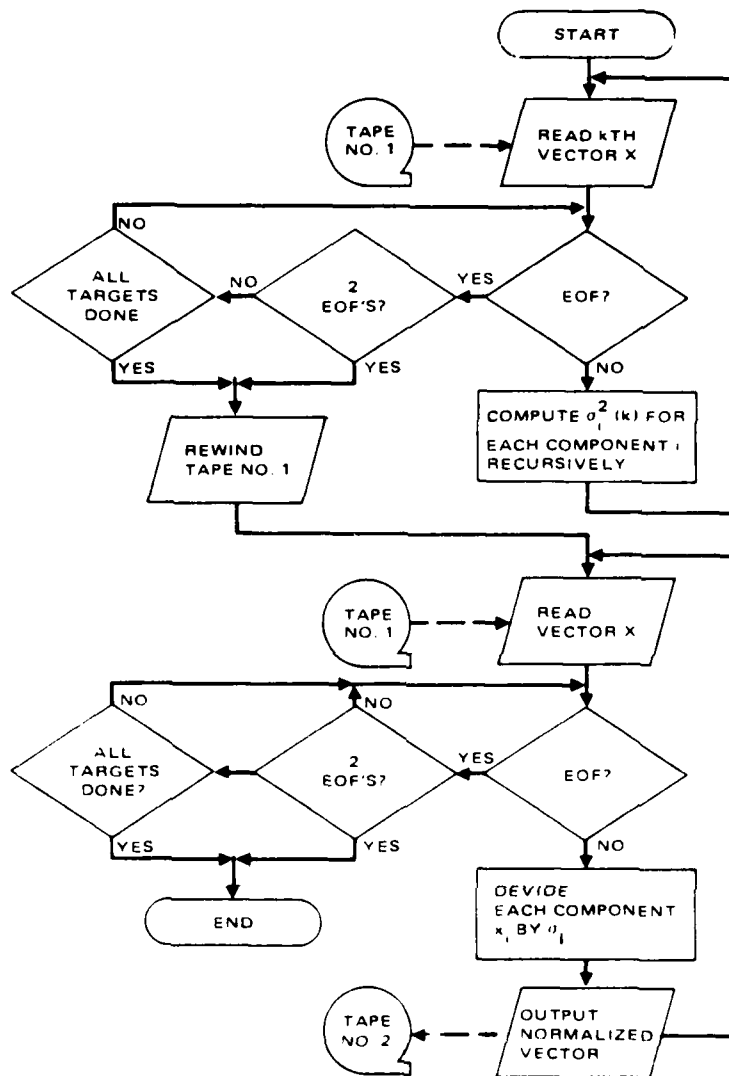
Figure B-3. Computer program for normalization of moments by
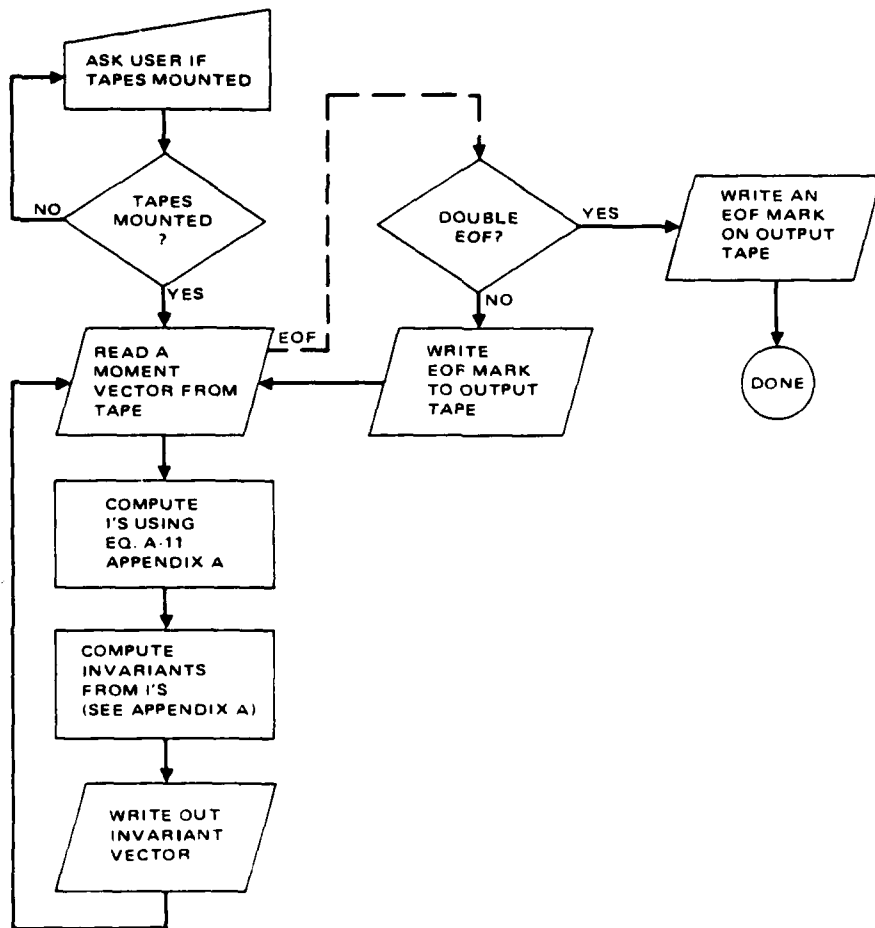their standard deviations

Figure B-4. Summary flow chart of computer program for computation
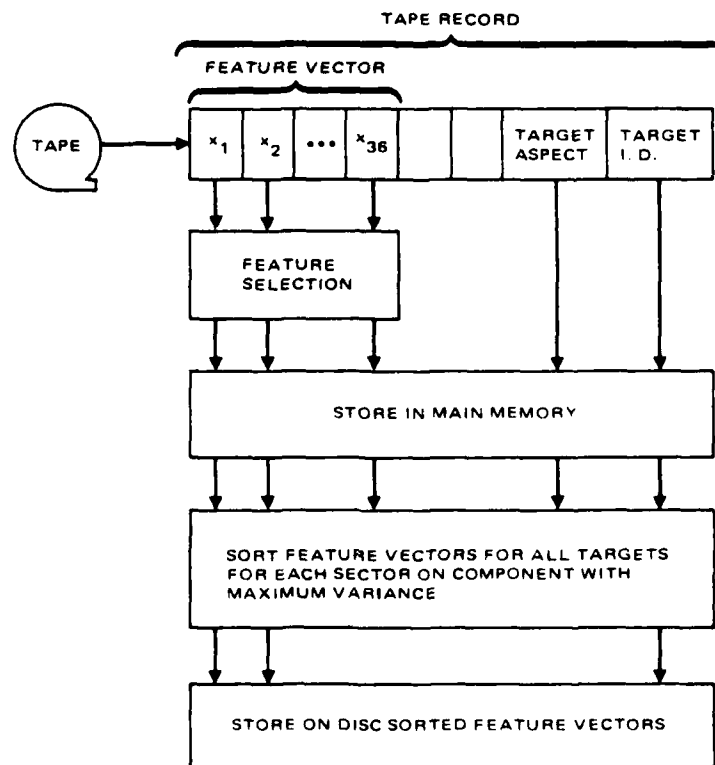orthogonal moment invariants

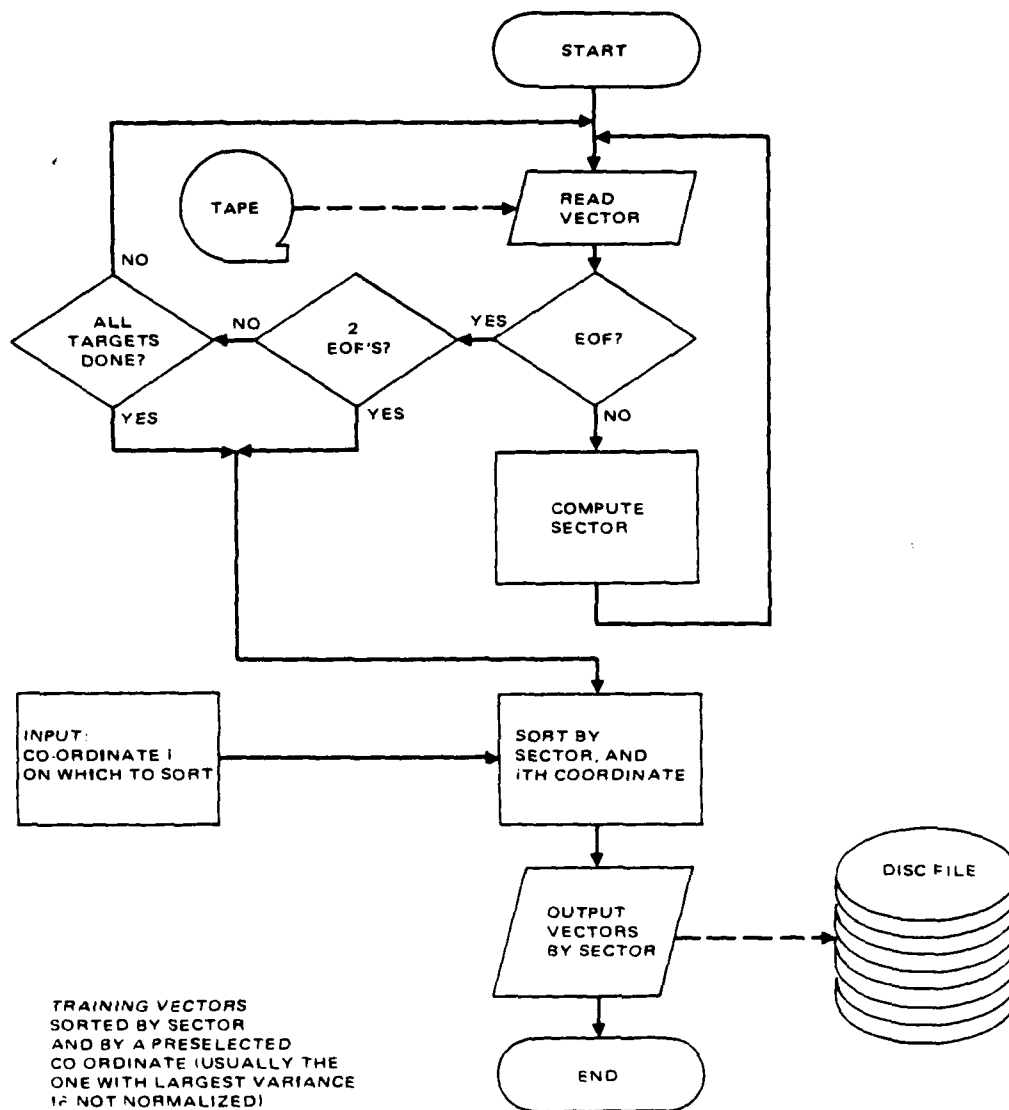Figure 8-5. Training kth nearest neighbor classifier

Figure B-6. Computer program for the formation of training files for nearest neighbor classifier
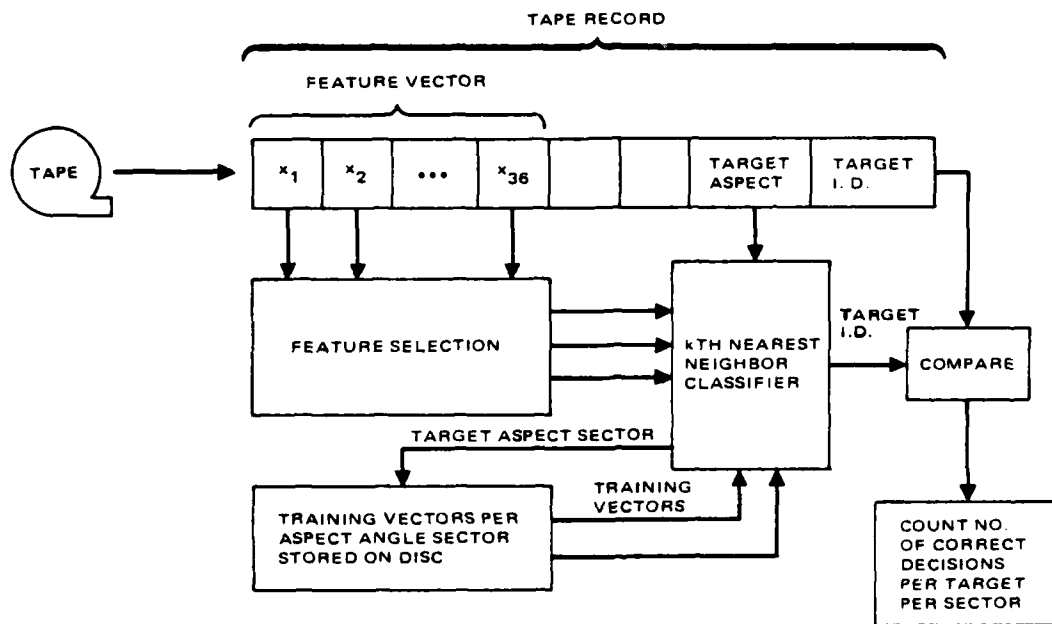
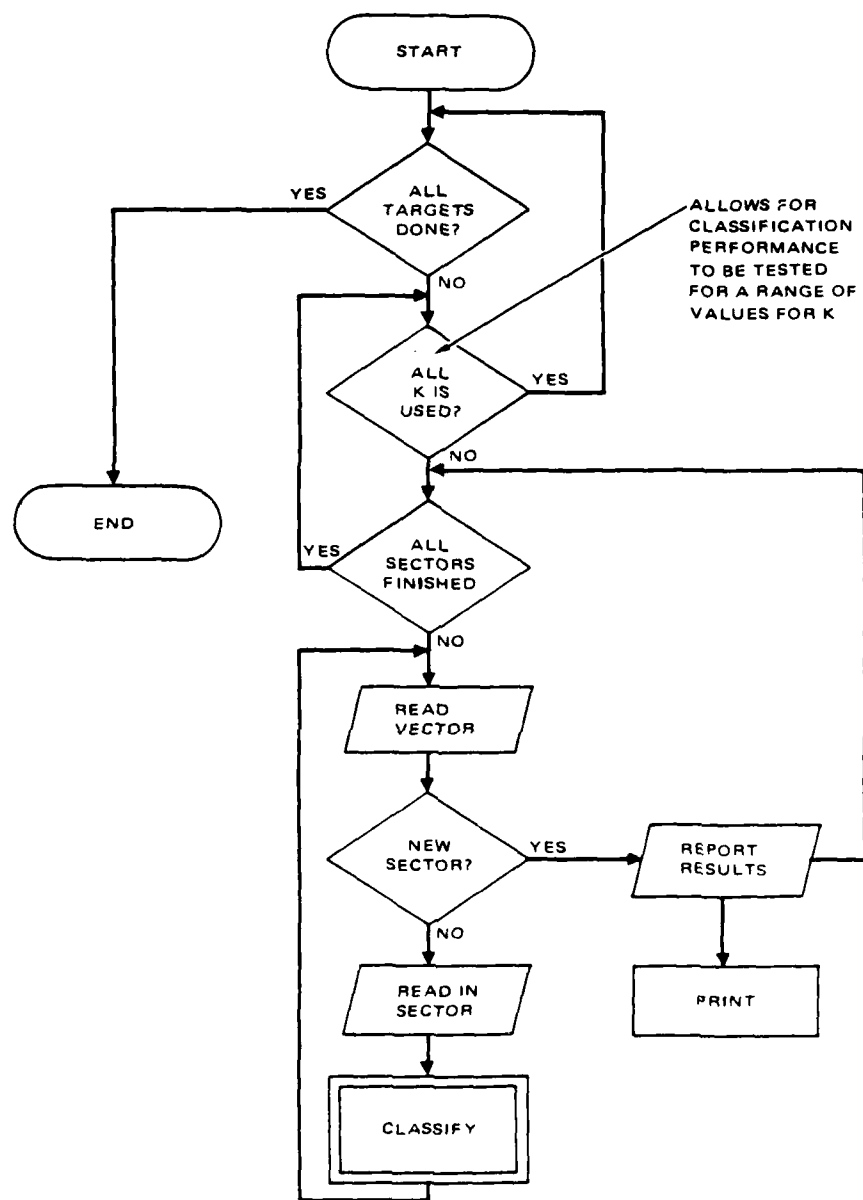Figure 3-7. Classification tests using kth nearest neighbor classifier

Figure 8-8. Flow chart of kth nearest neighbor classifier which performs classification tests over multiple targets aspect angle sectors and values for k
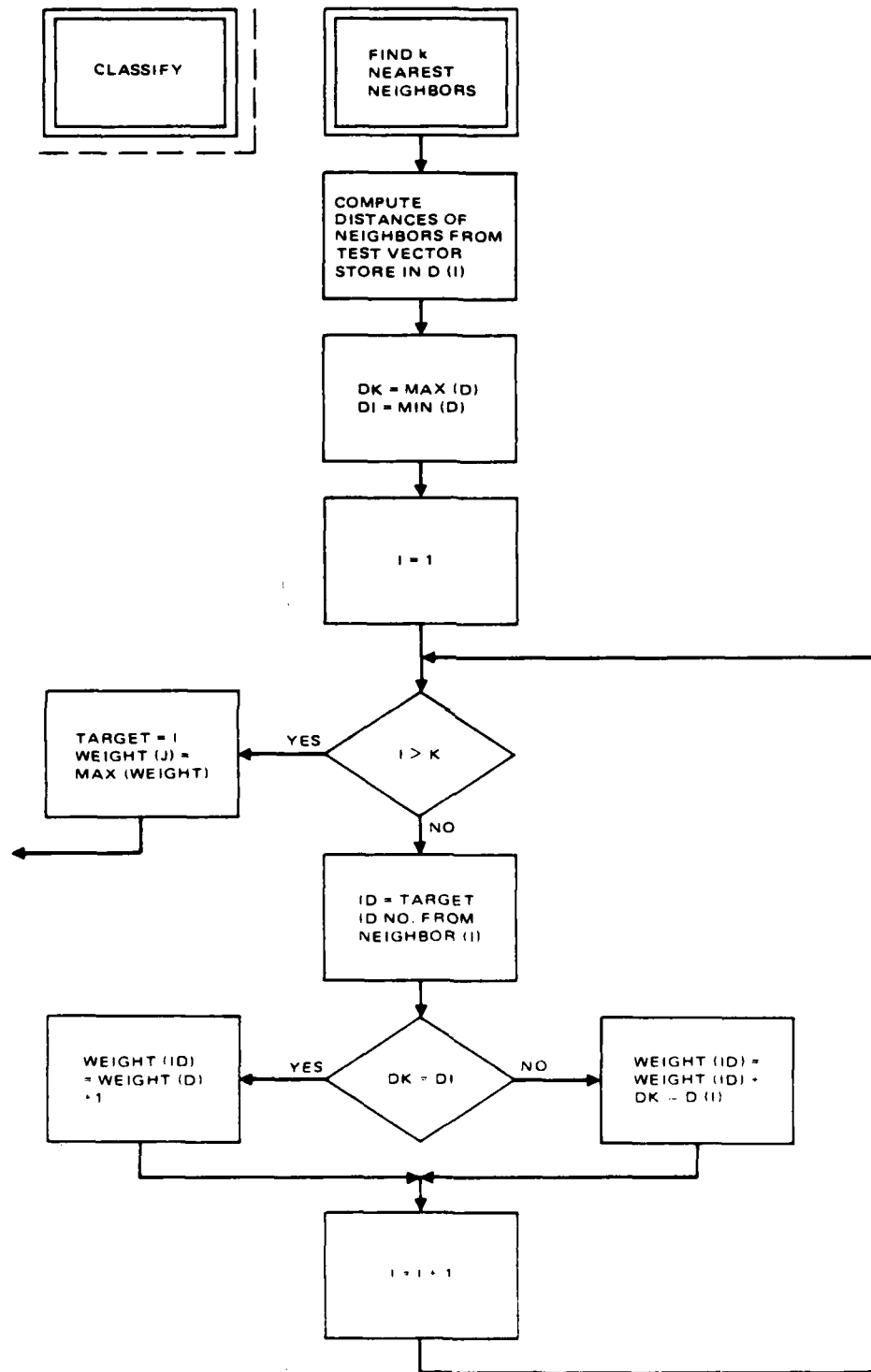
Figure 8-9 Flow chart of procedure classify in k-nearest neighbor classifier
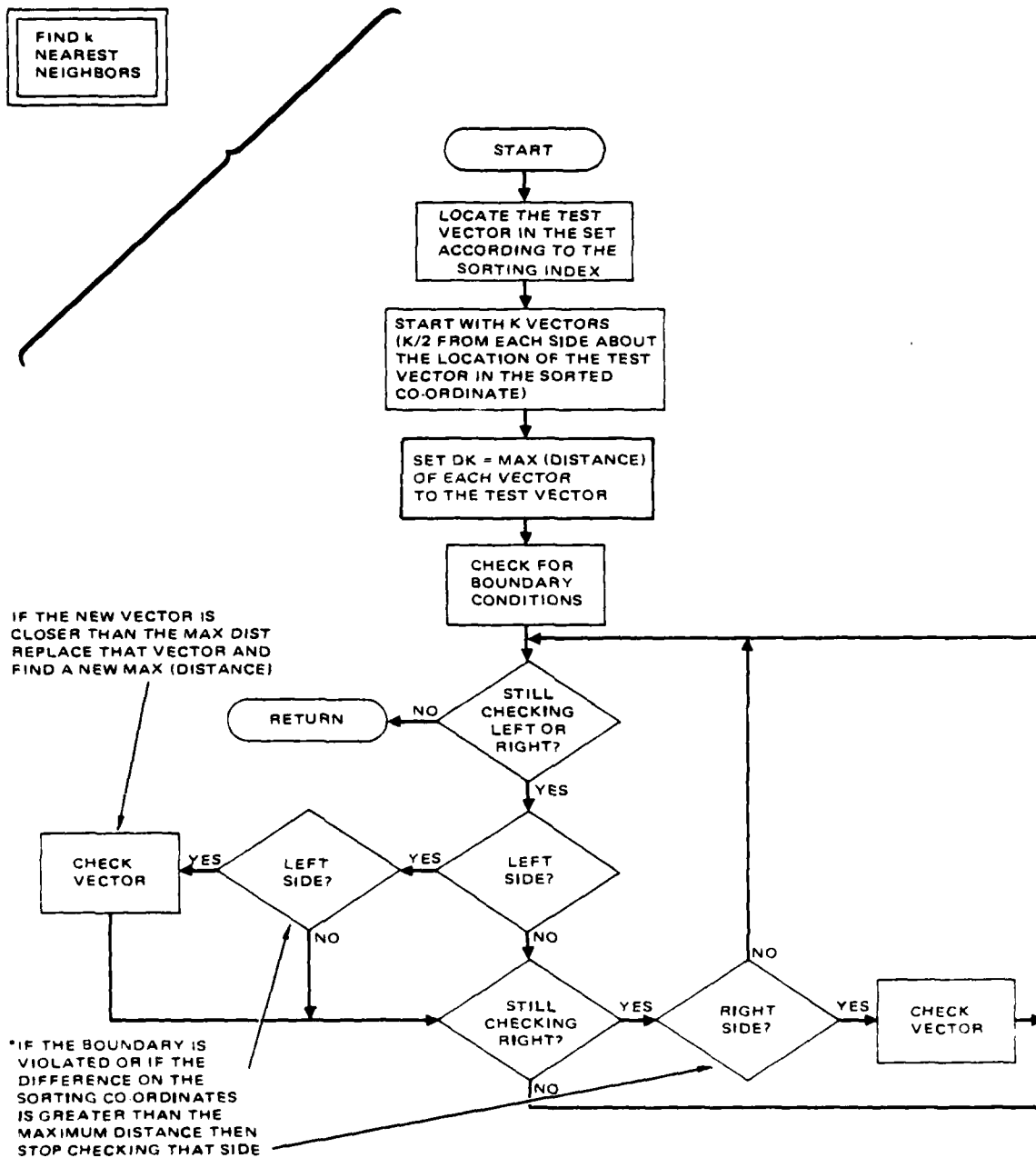
FIND k
NEAREST
NEIGHBORS

START

LOCATE THE TEST
VECTOR IN THE SET
ACCORDING TO THE
SORTING INDEX

START WITH K VECTORS
(K/2 FROM EACH SIDE ABOUT
THE LOCATION OF THE TEST
VECTOR IN THE SORTED
CO-ORDINATE)

SET DK = MAX (DISTANCE)
OF EACH VECTOR
TO THE TEST VECTOR

CHECK FOR
BOUNDARY
CONDITIONS

IF THE NEW VECTOR IS
CLOSER THAN THE MAX DIST
REPLACE THAT VECTOR AND
FIND A NEW MAX (DISTANCE)

STILL
CHECKING
LEFT OR
RIGHT?

RETURN   NO

YES

CHECK
VECTOR   YES   LEFT
SIDE?   YES   LEFT
SIDE?

NO   NO

*IF THE BOUNDARY IS
VIOLATED OR IF THE
DIFFERENCE ON THE
SORTING CO-ORDINATES
IS GREATER THAN THE
MAXIMUM DISTANCE THEN
STOP CHECKING THAT SIDE

STILL
CHECKING
RIGHT?   YES   RIGHT
SIDE?   YES   CHECK
VECTOR

NO

Figure B-10. Flow chart for k nearest neighbor classifier (continued)
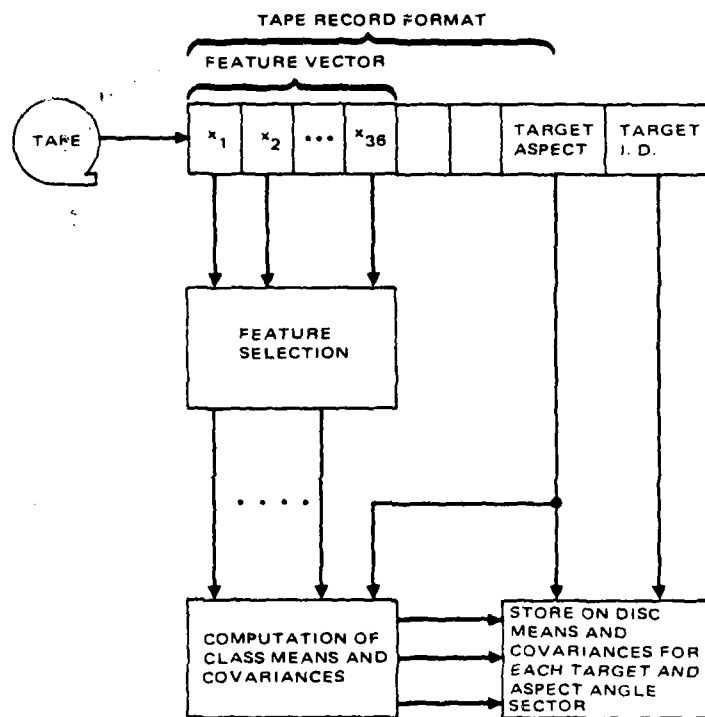
B-11
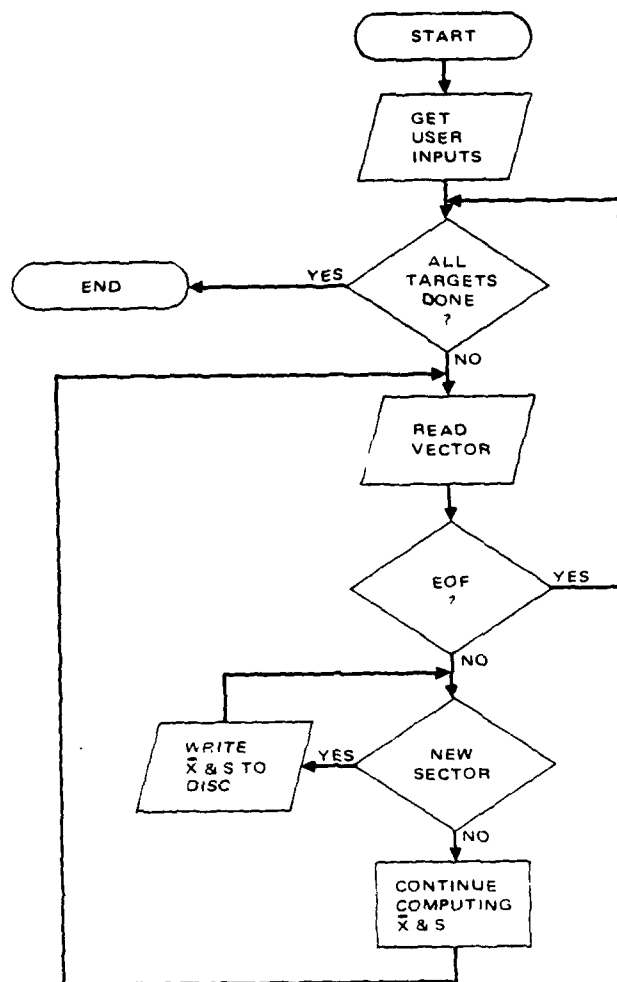
Figure B-11. Training Gaussian classifier

Figure B-12. Computer program for preparation of means and covariance matrices used by Gaussian classifier
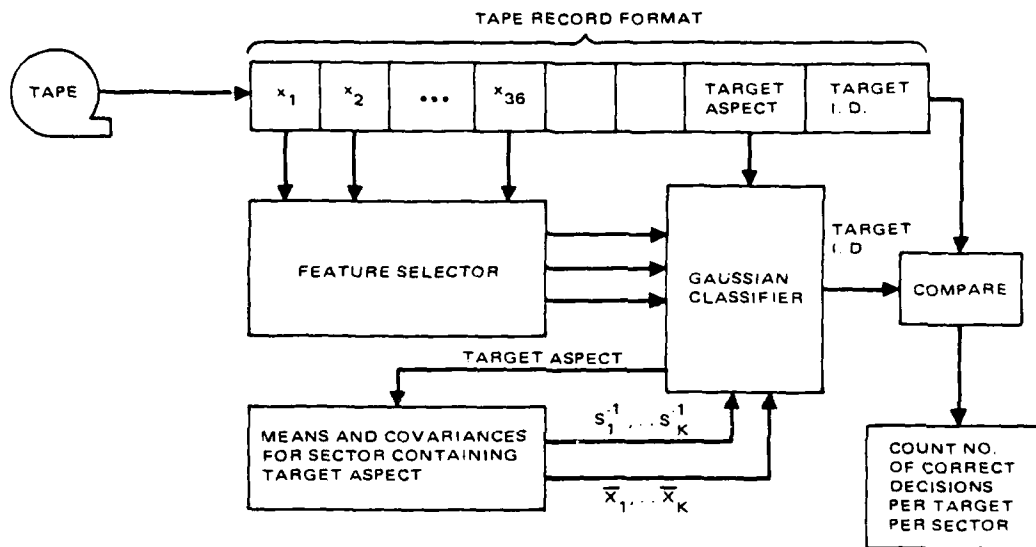
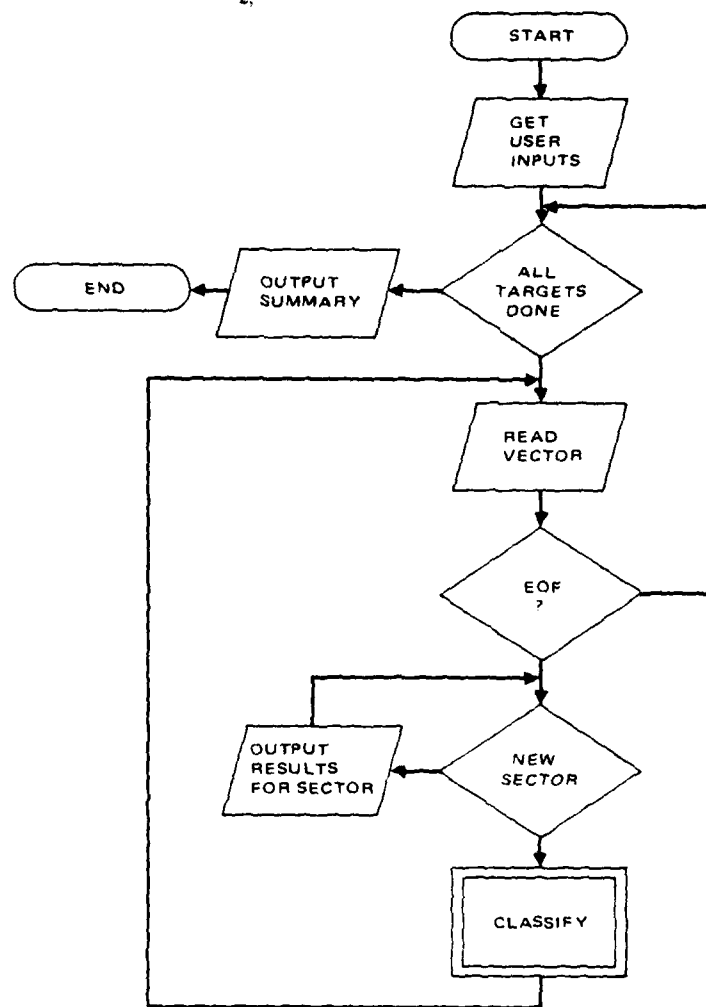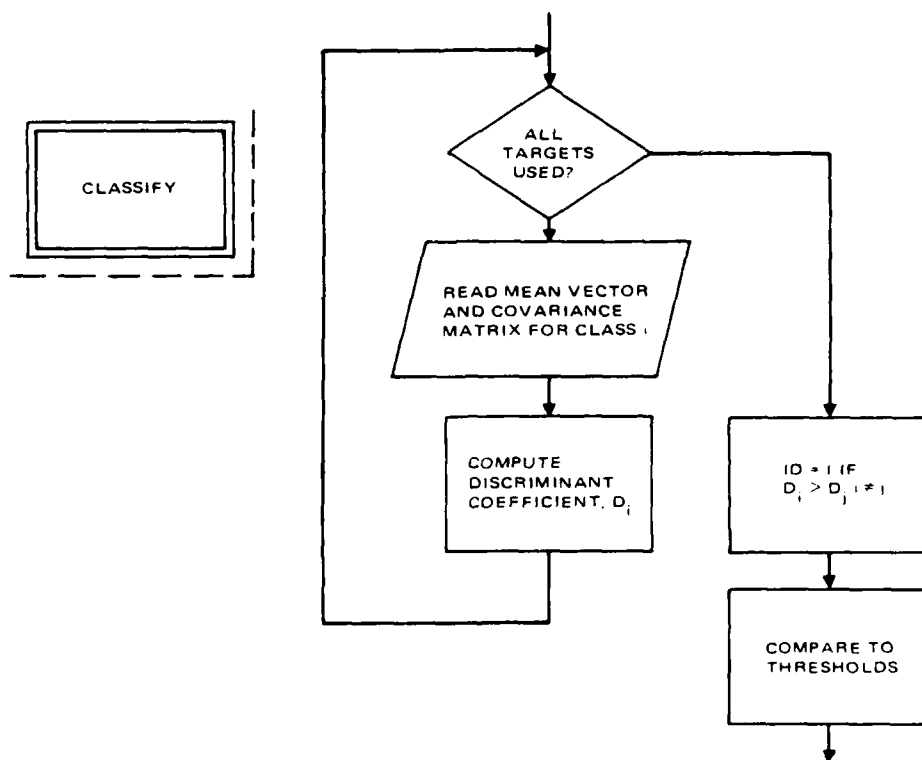Figure B-13. Classification tests using the Gaussian classifier

Figure B-14. Flow chart of computer program for the Gaussian classifier

*THE FIRST THRESHOLD IS FOR HOTELLING'S T^2 STATISTIC COMPUTED FOR
CLASS C, AND COMPARED TO A TABLE LOOK UP FROM THE F DISTRIBUTION
THE SECOND THRESHOLD IS ON THE *A POSTERIORI PROBABILITY* $P(C_i/X)$
WHERE X IS THE TEST VECTOR

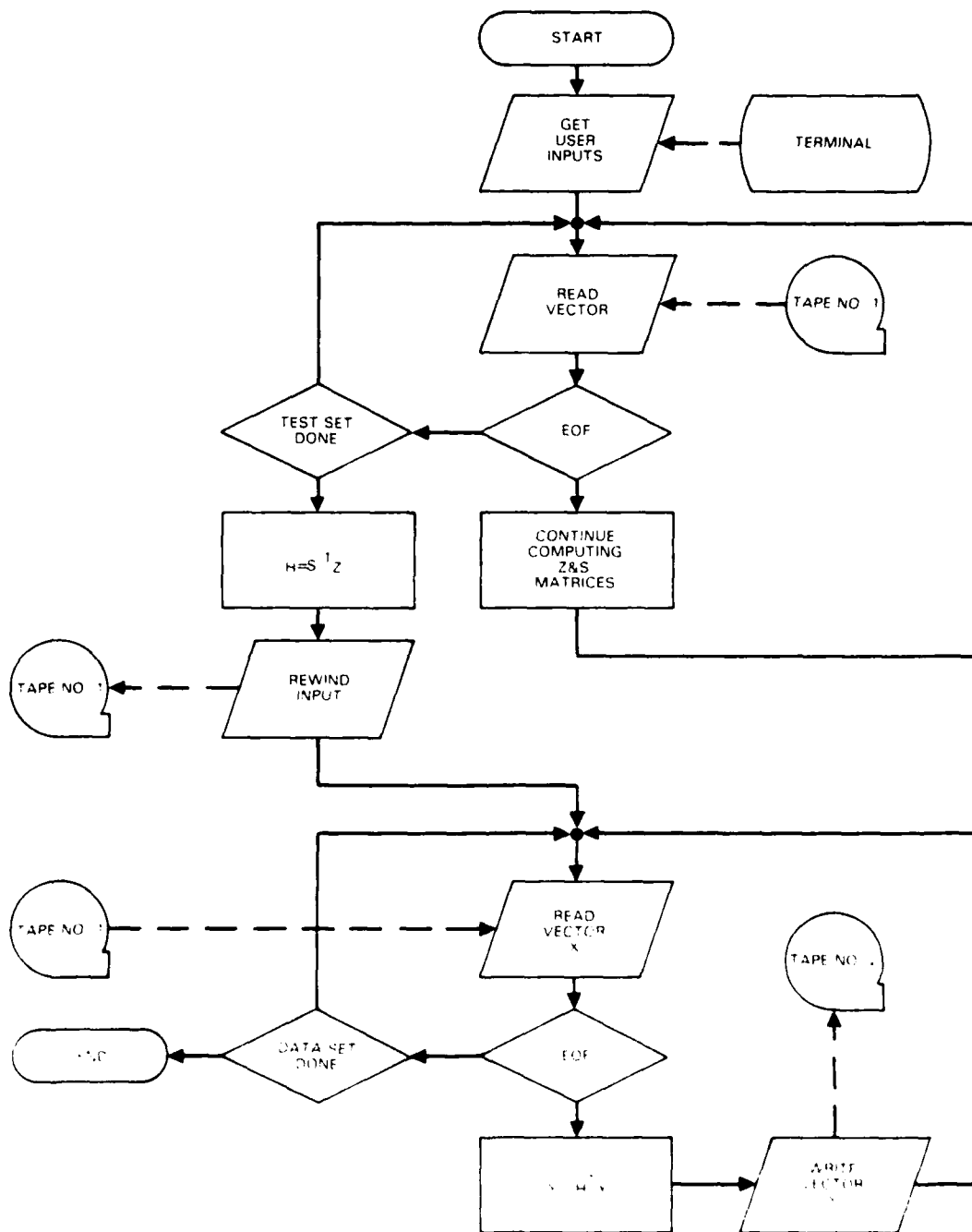Figure B-15. Flow chart of procedure classify of Gaussian classifier

Figure B-16. Feature ranking using the mahalanobis distance criterion.

Figure B-17. Feature vector dimensionality reduction by projection into a lower
dimensional subspace.

DISTRIBUTION

Addressee	DODAAD Code	Number of Copies
Scientific Officer	N0014	1
Administrative Contracting Officer	FY1767	1
Director, Naval Research Laboratory Attn: Code 2627 Washongton, D.C. 20375	N00173	6
Defense Documentation Center Bldg. 5, Cameron Station Alexandria, VA 22314	SA47031	12
Office of Naval Research, Branch Office 1030 East Green Street Pasadena, CA 91106	N62887	1